Nanoscale Energy Transport Investigated with Ultrafast Electron Microscopy

A Dissertation
SUBMITTED TO THE FACULTY OF
UNIVERSITY OF MINNESOTA
BY

Dayne Andrew Plemmons

IN PARTIAL FULFILLMENT OF THE REQUIREMENTS
FOR THE DEGREE OF
DOCTOR OF PHILOSOPHY

David J. Flannigan, Advisor

September 2017

# Acknowledgements

*To the thread…*

*IF YOURE*
*READING*
*THIS ITS*
*TOO LATE*

## Abstract

Direct visualization of dynamic and non-equilibrium processes occurring on the atomic-scale remains a tremendous challenge owing to the condensed time-scales associated with the reduction in length-scale. Coherent phonon transport, for example, occurs at the speed of sound over distances spanning a few nanometers to a few microns. As such, a single wavefront may emanate, propagate, and scatter over the course of just a few picoseconds. Uniquely, ultrafast electron microscopy (UEM) has the ability to probe phonon transport processes on the relevant condensed time- and length-scales simultaneously, avoiding ensemble averaging over time and space characteristic of many traditional probes. Here, we have focused on the development of UEM as a tool for direct investigation of energy transport processes on the nanoscale. We have studied a variety of phenomena in two-dimensional atomic crystals and discussed progress in methodologies in operation of a thermionic UEM.

In UEM, we call upon a variety of analytical modalities which utilize elastic scattering as a sensitive indicator of structural modulation within a crystalline lattice. Contrast in real-space arising from small angular perturbations in lattice orientation (and as result, local modulation of the Bragg condition) associated with phonon-mediated elastic deformation allows imaging the propagation of individual phonon wavefronts. We have discovered that phonon nucleation and launch occurs at discrete spatial locations along individual interfaces, and that the appearance of coherent, propagating wavefronts are extremely sensitive to the shapes of local strain fields and vacuum-crystal interfaces. Additional information from local elastic scattering in reciprocal-space allows examination of the specific modes and mechanisms of the observed phonon transport. In thin-films of $WSe_2$, we conclude that the observed modes arise from interfacial stress resulting from the initial excitation and confinement of compressional waves along the WSe2 c-axis stacking direction within the thickness of the specimen. We also observe large-amplitude out-of-plane modes in single-crystal and polycrystalline monolayer graphene membranes through examination of laser-excited variation in the Debye-Waller factor; we expect the intrinsic ripples of the suspended membranes mediate flexural modes in a manner similar to the morphologically dependent wavefronts in $WSe_2$.

We have found that the ultrafast imaging and diffraction experiments are subject to a variety of practical challenges associated with stroboscopic operation. For one, heat dissipation from the specimen must be considered such that pseudo-steady-state operating temperatures resulting from the laser-pulse-trains are within ranges suitable for a particular experiment. Additionally, dynamics occurring on time-scales comparable to instrument response require precise deconvolution for proper interpretation of instrinsic material response. As such, we systematically optimize photoelectron generation and collection and map the space-charge and temporal instrument-response parameter space as a function of photoelectron-packet population. We obtain photoelectron packets populated by up to ~$10^5$ electrons, and instrument-response times range from 1 to 10 ps (FWHM) for laser-limited single-electron packets to those with maximum packet population. This large range of achievable bunch-charge increases experimental

flexibility and allows UEM experiments to be conducted at relatively low repetition rates facilitating investigation of a greater range of ultrafast phenomena.

We expect the methodology and insight presented in this work will aid in future quantitative studies of energy transport in crystalline materials with nanostructured interfaces and atomic defects. Ultimately, we envision the direct insight available in UEM will facilitate design of materials and structures for precise control of energy transport and improvement of the numerous applications in which understanding heat transport is critical.

# Table of Contents

# List of Figures

# 1 | Introduction

Since Richard Feynman's now-famous seminar given in 1959 entitled "There's Plenty of Room at the Bottom",[1] the field of nanotechnology has become prevalent in all aspects of science and has encompassed technological innovation spanning the continued miniaturization of transistors powering Moore's law[2] to atomically precise materials design allowing tailoring of physical properties for specific applications[3, 4, 5]. Crucial to the explosion of nanoscience was the development of characterization techniques with atomic-scale spatial resolution sufficient to discern structural features on these condensed length-scales. Indeed, the development of the scanning tunneling (STM),[6] atomic force (AFM),[7] and transmission electron microscopes (TEM)[8] have been driving factors in the engineering of materials. The insight gathered via these techniques represent static structures at equilibrium; dynamic and non-equilibrium processes occurring on the atomic-scale pose additional challenges owing to commensurate reduction in the associated time-scales. Nanoscale acoustic waves, for instance, typically travel distances of a few hundred nanometers at velocities ranging from $10^3$ to $10^4$ m/s before scattering. As such, observing this process requires both nanoscale spatial resolution as well as

picosecond temporal resolution. One such method to obtain the requisite spatiotemporal sensitivity relies on stroboscopic extension of the conventional TEM via employment of precisely synchronized ultrashort laser pulses and packets of electrons. This technique, called ultrafast electron microscopy,[9, 10, 11] and the development there-of is the focus of this dissertation. Specifically, we will focus on employing the technique to examine energy transport on the nanoscale, which, in a large range of materials and structures, occurs via propagation and scattering of acoustic vibrations called phonons.

## 1.1 | Thermal Transport and Coherent Acoustic Waves

Continuum solid-state heat transport is described by Fourier's law which states that heat flux per area, $q$, is proportional to the temperature gradient, $\nabla \cdot T$, by a constant material property called the thermal conductivity, $k$. On the nanoscale, however, this approach breaks down for a variety of reasons. First, temperature is a thermodynamic quantity which is defined for a large ensemble (i.e. approaching the thermodynamic limit when $N \to \infty$). Second, Fourier's law describes diffusive heat flow in which heat carriers akin to particles travel randomly due to collisions with other energy carriers. In reality, phonons typically travel unabated for a distance called the phonon mean-free-path, $\lambda_p$, which can be a few nanometers to several microns for primary energy carriers. Thus, energy transport on length-scales smaller than the characteristic length set by $\lambda_p$ is not adequately described by Fourier's law.[12, 13] In this regime heat transport becomes much less akin to particle diffusion but rather exhibits coherent wave-like phenomena.

Despite lacking a detailed theoretical understanding of heat transport on length-

scales comparable to $\lambda_p$, many devices and materials indeed exploit structural features just a few nanometers in size; microelectronics, optoelectronics, microelectromechanical sensors, semiconductor quantum dots and superlattices, polymer nanocomposites, and multilayer coatings are examples of current commercial market products which exploit nanoscale features. Thus, a robust depiction of thermal energy transport is critical in continued development of these technologies. Energy dissipation from transistors, for example, has imposed a practical limit on power density in CPUs and must be reconciled to extend Moore's law.[14] Further, a large portion of energy used in electronics is dissipated as waste heat, which, in the case of a growing information technology infrastructure, requires additional energy consumption for cooling. Indeed, thermal transport is at the center of many current challenges regarding energy consumption, generation, and dissipation.

While the wave-nature of thermal energy carriers on the nanoscale complicates the depiction of heat transfer, it also opens opportunities for their coherent manipulation. Drawing upon analogies to sound amplification and manipulation (such as whispering galleries and other acoustic cavities), one could envision extension of these technologies to few nanometer wavelength vibrations which comprise thermal phonons. Indeed many recent revolutions in technology have centered on the ability to control electrons and photons, and vigorous efforts to design structures and materials for phonon manipulation could lead to similar gains.[15] Such ideas have included resonant cavities for optomechanical coupling,[16, 17] thermal metamaterials for heat cloaking,[18] phononic crystals with lattices designed for confinement of vibrations with tunable wavelength,[19]

and hierarchical nanostructured features for scattering of phonons across a variety of wavelengths.[20] Though this field is in its infancy, the paradigm shift in nanoscale heat transport seems promising for engineered heat transport and confinement.

Importantly, understanding the nature of interaction between phonons and material interfaces and defects is critical in both developing a nanoscale depiction of heat-transfer and applications exploiting coherent phonons. We seek to examine and identify specific phonon modes and their evolution and scattering at well-defined interfaces and material defects.

## 1.2 | Ultrafast Electron Microscopy (UEM)

### 1.2.1 | Probing Nanoscale Energy Transport with UEM

In order to elucidate the dynamics of collective excitations in the presence of individual interfaces and defects, one must contend with the difficult-to-access spatiotemporal regimes in which these phenomena operate. At the unit-cell level, speed-of-sound phonon wavefronts typically transit such spatial dimensions in less than 100 femtoseconds (fs). The propagating energy causes local bond modulation and a transient elastic deformation of the lattice, briefly re-orienting the atoms in a manner dictated by the symmetry of the mode. Structural dynamics of this nature are amenable to study with ultrafast methods that make use of the dependence of scattering wavevectors on lattice orientation and symmetry,[21, 22] movement or spacing and symmetry changes of the reciprocal lattice; or transient modulations in optical properties resulting from lattice distortion. Despite being sensitive to symmetry changes,[23, 24] bond dilation and

4

breaking,[25, 26] and atomic-vibration amplitude,[27, 28] these methods typically probe lattice motion within material volumes that are large relative to nanoscale discontinuities (i.e. for parallel-beam diffraction or optical spot sizes limited to the diffraction limit). Additionally, elastic scattering techniques which probe structure in reciprocal space often lack phase information, and real-space identification of phonon modes propagating on the nanometer length-scale remains difficult. Real-space imaging in ultrafast electron microscopy (UEM) – specifically, the bright-field and dark-field imaging modalities – is sensitive to elastic deformation of the lattice via variations in the local Bragg condition and thus offers insight into phonon nucleation, propagation, and scattering at individual nanoscale interfaces and atomic defects. We can exploit this technique, and auxiliary information from ultrafast electron diffraction, to gain insight into energy transport beyond an ensemble-averaged picture of the dynamics.

1.2.2 | Practical Considerations in Employment of UEM

The use of discrete electron packets to probe transient structures introduces challenges stemming from the fermionic nature of electrons. Electron-electron repulsion occurring at the photoelectron source (space-charge) and during packet propagation from source to specimen (Coulombic repulsion) limits spatial and temporal resolutions via degradation of coherence lengths.[29, 30, 31] A variety of methods have been developed to overcome such limitations, including photoelectron-packet compression with synchronized electromagnetic fields [32, 33] and operation at megavolt (as opposed to kilovolt) accelerating voltages,[34, 35] though these strategies have largely been implemented in dedicated electron-diffraction instruments. An alternative method often

5

employed in ultrafast electron microscopes is to populate each probe packet with, on average, a single photoelectron, thus altogether circumventing the deleterious effects.[36, 37] In this regime, one would expect the statistical temporal distribution of the probe component to approach the fs UV laser-pulse duration used to generate the photoelectrons.[38, 39]

Conducting ultrafast electron microscopy (UEM) experiments in the single-electron regime introduces additional practical challenges that limit the operational parameter space. Though fast-electron scattering cross-sections are large compared to X-ray photons, roughly a million or more are typically needed to generate sufficient signal-to-noise ratios. Thus, high laser repetition rates (*e.g.*, MHz) and/or long acquisition times (*e.g.*, tens of seconds or longer) must be used. Despite this, it has been shown that the UEM single-electron regime enables preservation of the intrinsic instrument spatial resolution (*e.g.*, 2.3 Å in real-space images).[38, 40, 41] Accordingly, the limiting factors in UEM experiments become relatively long specimen relaxation times following fs excitation (which dictate the experiment repetition rate), as well as real-time environmental instabilities and specimen drift or other non-reversible motion occurring during acquisition (which ultimately limit real-space resolution).

Despite the challenges mentioned above, the UEM stroboscopic approach employing fs laser pulses can be used to study a wide variety of systems, materials, and phenomena in the combined nanometer-picosecond spatiotemporal parameter space (angstrom dimensions in reciprocal space). In this regard, UEM instruments equipped with relatively large, flat ceramic photocathodes (*e.g.*, $LaB_6$) can be used to generate

6

photoelectron packets with populations spanning several orders of magnitude (*i.e.*, from 1 to $\sim 10^5$ electrons per packet for fs UV laser pulses).[36, 38, 41] Importantly, this enables operation at relatively low repetition rates when using packets with large populations, despite a commensurate reduction in temporal resolution from hundreds of fs to picoseconds.[42, 43] While providing experimental versatility, detailed determination of the instrument characteristics (combined spatiotemporal resolution) is non-trivial owing to the complex interplay between photocathode position and properties (*i.e.*, work function, geometry, Fermi distribution, *etc.*), electrostatic electron-gun biasing, and the magnitude of bunch charge.[44] This work will focus additionally on the photogeneration of ultrashort electron packets suitable for use in UEM and development of methods to characterize instrument response spanning the single-electron to high bunch-charge regimes.

## 1.3 | Two-dimensional Atomic Crystals

We have chosen an emerging class of materials known as two-dimensional atomic crystals as a platform to study nanoscale energy transport. Recent extensive study on 2D materials has uncovered numerous novel properties and unusual phenomena arising from planar confinement effects.[45, 46] Specifically, thermal transport properties display an extraordinary disparity; thermal conductivities range from the highest ever measured (graphene)[47] to below theoretical limits for crystalline materials ($WSe_2$).[48] We seek to uncover phonon behavior which dictates these thermal transport discrepancies.

### 1.3.1 | Graphene

The anomalously large thermal conductivity of monolayer graphene, the largest ever measured for any material[47], has led to vigorous fundamental and applied research into thermal transport properties of the 2D material.[49] From a fundamental standpoint, the isolated plane of covalently bonded atoms acts as a model system for investigation of various phonon scattering effects both within a perfectly crystalline lattice and upon introduction of point and line defects.[50, 51] In particular, graphene grain boundaries,[52, 53] which act as one-dimensional line defects separating domains of tilted crystalline orientation, persist in commercially-viable synthesis techniques such as chemical vapor deposition (CVD), and their role in phonon scattering must be understood in applications seeking to exploit the excellent conductive properties for thermal management of nanoscale electronics.[54, 55] Conversely, intentional introduction of grain boundaries and other defects has been proposed as a route to independent reduction of the thermal conductivity (that is, while maintaining high electrical conductivity) for enhanced thermoelectric performance.[20, 56, 57]

Indeed, graphene has acted as a springboard for investigation of 2D materials, and unusual physical phenomena arising from planar confinement of charge and heat transport are being uncovered at a rapid pace.[45, 46] The nature of phonons in these materials holds particular importance as it was thought for decades that the presence of long-wavelength vibrations would preclude the stability of crystalline order in two dimensions at finite temperatures.[58] The stabilization of suspended graphene and other two-dimensional membranes is believed to occur through height fluctuations normal to the plane of atoms accommodated by anharmonic coupling of bending and stretching

modes,[59] and experimental observations of this behavior in monolayer graphene suggest ripples on the order of 5 to 10 angstroms in amplitude exist for samples isolated on the microscale.[60] Interestingly, phonon modes similar in nature to the out-of-plane ripples – that is, the so-called flexural phonon mode – have been found to dictate thermal transport in the material.[61, 62] Thus, understanding these types of vibrations is critical not only from the standpoint of mechanical stability but also in the observed thermal properties.

1.3.2 | Transition metal dichalcogenides (TMDs)

*Tungsten selenide (WSe$_2$)*

WSe$_2$ has generated an enormous amount of interest owing to dramatic differences in, and tunability of, transport properties (thermal and electronic) along different crystallographic directions and with varying numbers of layers. For example, it was shown with WSe$_2$ that the cross-plane thermal conductivity could be made several times smaller than the predicted minimum value (indeed, the smallest measured for any fully dense solid) via disordering of the two-dimensional sheets.[48] This was attributed mainly to phonon localization stemming from the incommensurate nature of the individual crystalline WSe$_2$ planes, thus restricting these modes from significantly contributing to thermal transport. Additionally, modulation of band-gap energy and k-vectors with layer number makes such materials ideal for studying coherent excitonic phenomena (e.g., coupling of excitons to optical- and acoustic-phonon reservoirs) that serve as the basis for optoelectronic applications.[63, 64, 65, 66, 67]

Notably, WSe$_2$ is a much higher *Z* material than graphene – that is, it shows enhanced electron scattering as it contains high-atomic-number elements.[68] Operating in

the low beam current regimes associated with UEM, the enhanced scattering cross-section of the material alleviates stroboscopic experimentation and acts as an ideal system for developing analytical modalities in UEM for investigating phonon transport.

*Tantalum sulfide (TaS$_2$)*

TMDs such as TaS$_2$ display correlated electronic phenomena such as charge-ordering. Indeed, formation of superlattices corresponding to charge density waves (CDW) is highly dependent on the stacking of the layers, coordination of the atoms within layers, and the thermodynamic conditions accompanying the lattice. Open questions relating to the effect of lattice distortion (i.e. phonons) on observed charge-ordering could potentially be clarified with ultrafast electron diffraction and imaging.[69, 70, 71] While photo-excited phase transitions in TaS$_2$ have been extensively studied, uncovering the dynamic topology of charge-ordering in real-space presents an enormous challenge. UEM potentially serves as tool to identify local nucleation or melting of specific charge-order phases and the commensurate lattice distortions via combined ultrafast diffraction and imaging.

## 1.5 | Summary

In summary, we have described the basis for this project. We seek to develop UEM as a tool for investigating energy transport on the nanoscale via direct imaging of acoustic elastic perturbations on their native time- and length- scales. We aim to optimize the operation of the UEM and determine photoelectron packet characteristics as well as employ various analytical modalities to examine thermal transport in 2D materials exhibiting a wide range of unusual phenomena.

# 2 | Equipment and Methods

In this chapter we will summarize the equipment and methods employed in our pursuit of examining nanoscale energy transport. Specifically, we will describe the operating principles of conventional TEM, UEM and Raman spectroscopy as well as outline specimen preparation and characterization procedures. Finally, we will expand on experiments unique to UEM and the operational parameters employed.

## 2.1 | Equipment

### 2.1.1 | Transmission Electron Microscopy (TEM)

Morphologies of the minor perturbations in crystalline lattices forming the basis of heat transport have features much smaller than the diffraction-limited resolution of optical microscopy and indeed are not conducive to contrast in such a technique. As such, the enhanced contrast and resolution offered by TEM is a valuable tool for the characterization and experimentation of 2D thin-films and the energy transport there-in. In TEM, accelerated electrons of de Broglie wavelength on the order of a picometer theoretically enable resolution below 0.5 Å, though resolution is traditionally limited by a

handful of lens aberrations.[72] A wealth of analytical information about the specimen – including crystal structure, defect structure, and composition – originates from the various interactions of the incident electrons with the specimen.[73]

In conventional TEM (CTEM), a parallel beam of electrons illuminates the specimen, and contrast arises from the scattering of the incident beam. Bright-field images formed from the incident beam typically exhibit mass-thickness contrast arising from the spatially varying electron transmission intensity of the specimen. Elastically scattered electrons contain information on the crystal structure and crystallographic orientation of the specimen and can be projected in reciprocal space in the form of a diffraction pattern or in real space as a phase-contrast or diffraction-contrast image. Phase interference between elastically scattered beams can be manifested at high-magnification as lattice fringes that resemble the atomic columns of a crystal or complex Moiré and Fresnel fringes at lower magnification.[72] Although interpretation of these images can be challenging, they contain a wealth of information on the local structure of a material. In dark-field imaging, only an individual elastically scattered beam is used to form an image, allowing for visualization of grain sizes and shapes in polycrystalline materials. Altogether, CTEM provides various convenient routes to valuable atomic-scale information in both real and reciprocal space.

In addition to CTEM, most modern TEMs are equipped with a condenser lens system capable of generating a convergent beam probe. Convergent beam diffraction allows sampling of a much smaller region than selected-area electron diffraction (SAED) in CTEM and also contains information that cannot be obtained with SAED, such as full

12

three-dimensional structure and lattice strain.[68] In real space, scanning TEM (STEM) uses a sub-angstrom convergent probe to detect scattered electrons and x-rays from a very small area. The probe is raster scanned across a desired region to form an image or digital map. Scattered electrons can be collected on an annular dark-field detector to form directly interpretable Z-contrast images.[74] Alternatively, x-ray energy dispersive spectroscopy (EDS) or electron-energy loss spectroscopy (EELS) data can be collected and used to create an elemental map of a desired region.[72] The auxiliary information provided by convergent beam techniques adds to the versatility of TEM as an analytical tool.

## 2.1.2 | Ultrafast Electron Microscopy (UEM)

A schematic of a UEM configured for stroboscopic operation is shown in Figure 2.1. The inset shows, conceptually, the generation of one time point ($\tau$) and the method for assigning a single temporal value to pulses with a finite duration. The general experimental procedure is as follows. A femtosecond laser pulse is split into what are dubbed pump and probe beams. The pump beam (which may undergo non-linear conversion depending upon the excitation of interest) is directed onto the specimen and initiates the dynamics. The probe beam is directed into the Wehnelt cylinder of the electron gun after undergoing appropriate harmonic generation; ultraviolet pulses are used to generate photoelectron packets from the $LaB_6$ emission source. The discrete, femtosecond photoelectron probe packets are then accelerated and directed down the column in the manner typical for standard TEMs with thermionic gun assemblies. One temporal point ($\tau$) is generated by fixing the relative arrival times of the photon pump

pulse and electron probe packet with a motorized optical delay stage. Additional points

are generated by changing the position of the stage such that the arrival times now differ

by $\tau + \Delta\tau$.
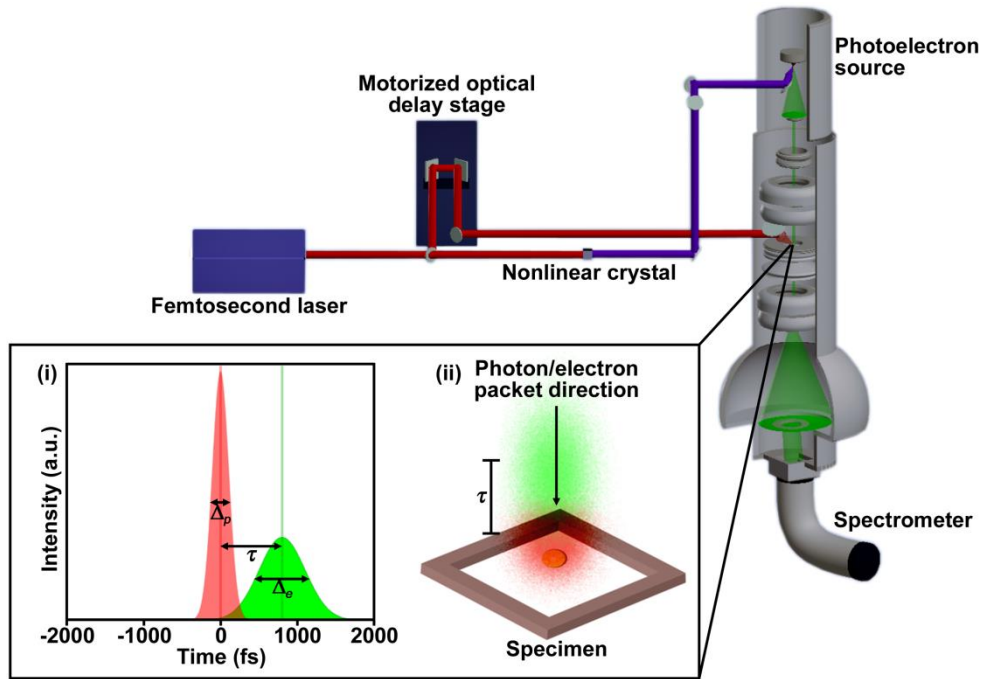


**Figure 2.1** Condensed schematic of the ultrafast electron microscope (UEM) and

overview of the experimental concept. The critical components are labeled, including the

spectrometer, which is necessary for the particular method outlined here. The inset

shows **(i)** an example of the temporal overlap of the photon pulse and electron packet

separated in time by $\tau$ [$\Delta_p$ and $\Delta_e$ represent the photon pulse and electron packet temporal

durations (full-width at half-maximum, FWHM), respectively], and **(ii)** a schematic of the

spatial interaction region of $\Delta_p$ and $\Delta_e$ at the specimen, again separated in time by $\tau$.

Electron packets employed in fs-UEM are populated with anywhere from 1 to

~$10^5$ electrons.[75] As such, a single pulse is insufficient for generating adequate signal-to-

noise on conventional detectors (typical TEM images are formed with $10^7$ to $10^9$ counts). Rather, the stroboscopic method relies on sequential excitations from laser pulse-trains with frequency, $f$. Schematically illustrated in Figure 2.2, image acquisition at a specified time-delay corresponding to a specific moment in the material response occurs over many pulses and is contingent on each electron packet sampling precisely the same instance of dynamic response. Image acquisition typically occurs over seconds and at repetition rates from a few kHz to a MHz corresponding to $\sim 10^4$ to $\sim 10^7$ electron packets employed in each acquisition. Critically, for proper stroboscopic operation, the material response must be entirely reversible and completed within the time-period specified by $1/f$ (typically a few μs to a few hundred μs). Meeting these criteria for a particular specimen while obtaining sufficient beam current to ensure tractable experiments is indeed a challenge in UEM operation.
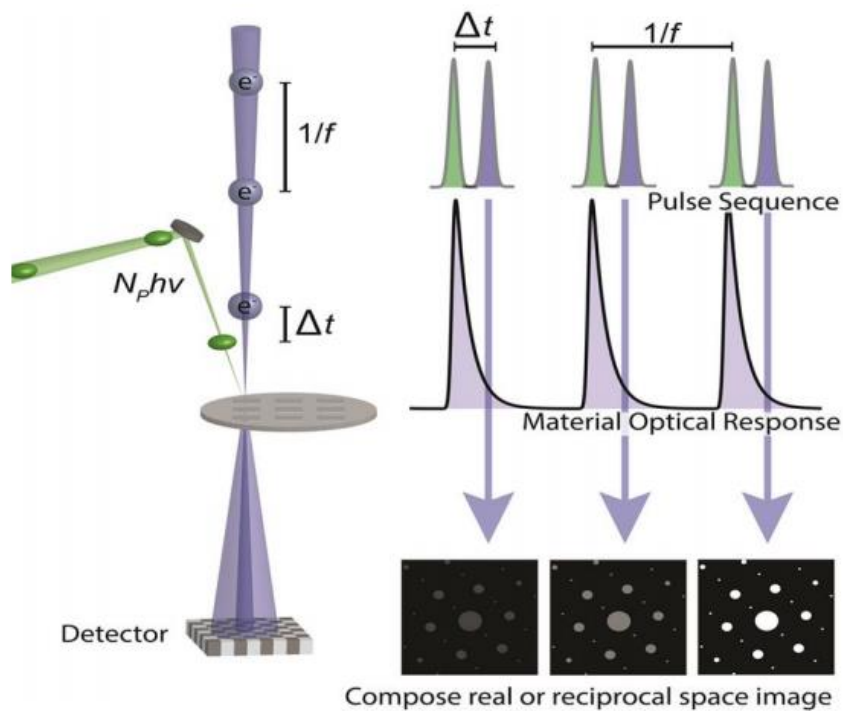
**Figure 2.2** Schematic representation of stroboscopic image acquisition in UEM. Photoelectrons (blue) probe an instance of material response to the ultrashort optical excitation (green) dictated by the delay of arrival between the laser pulses and electron packet at the specimen ($\Delta t$). An image with sufficient signal-to-noise is acquired over exposure to many electron packets in a pulse-train with repetition rate, $f$.

Excitation appropriate for materials with varying optical properties is tuned by adjustment of optical components in the laser line. Outlined in Figure 2.3, a Yb:KGW (1030-nm fundamental output), diode-pumped, solid-state Light Conversion PHAROS laser and a custom Light Conversion HIRO harmonics generation module are used to generate laser pulses at 1030 nm, 515 nm, 343 nm, and 258 nm. A single wavelength is directed to the specimen region through an optical periscope in an octagon port on the TEM after propagation down a mechanical delay stage, and in all cases the 258 nm light is split and directed toward a truncated $LaB_6$ cathode to generate photoelectrons.
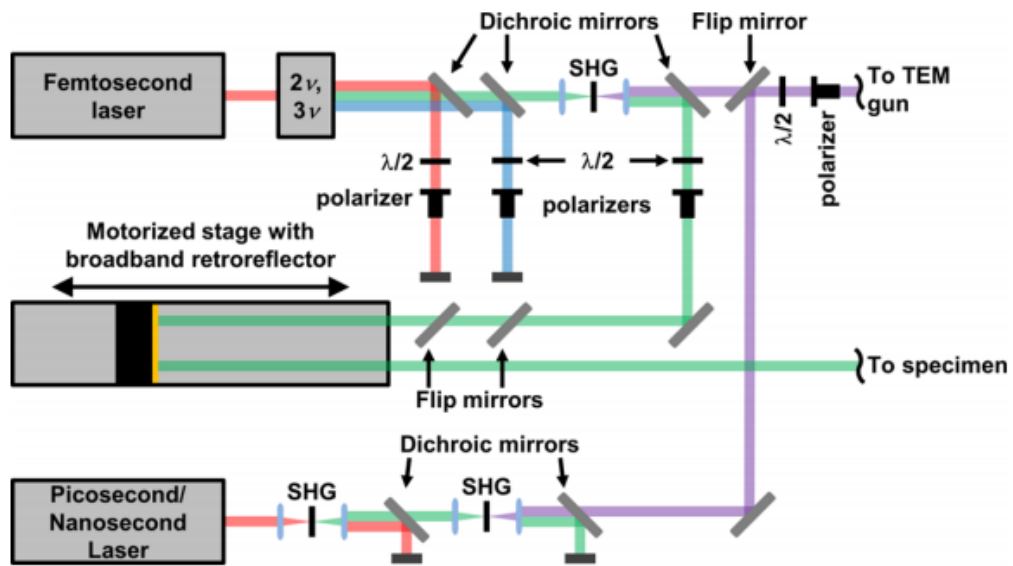


**Figure 2.3** Schematic outline of laser beamline employed in our lab. The fundamental

1030 nm (red) beam from the fs-laser harmonically generates 515 nm (green), 343 nm (blue) (any of which can be used to excite the specimen) and 258 nm (purple) (used to generate photoelectrons). The fourth-harmonic of an electronically triggered ps-laser (1064 nm fundmental) can also be employed to examine dynamics from the ns to ms timescales.

The meter-long delay stage is sufficient for examining material response from the few fs timescale (and is only limited by the incremental resolution of the delay stage steps) to the few ns timescale (limited by the maximum path-length addition upon propagation down the delay stage; i.e. ~2 m). For dynamics occuring between the ns and ms time-scales, an electronically triggered Nd:YAG (1064-nm fundamental output) laser with ~500ps pulse duration is employed. The same stroboscopic principles apply for these experiments, but the implementation of the precise delay is acheived via an electronic delay generator. Through versatility of laser system employed, we are in principle able to examine material response across time-scales spanning 12 orders of magnitude – that is, from the few-fs range out to the CCD-limited few-ms timescale.

2.1.3 | Confocal Raman Microscopy

Raman spectroscopy provides sensitive insight on the bonding environment of a material, which in the case of graphene, can greatly vary in the vicinity of defects, bi- and multi-layers, and wrinkles.[76] This technique excites a specimen with monochromatic light and detects the shift in frequency of the reflected light due to the inelastic scattering of the photons by phonons. Conservation of energy and momentum requires that phonons emitted must obey the fundamental Raman selection rule, $\mathbf{q} \approx 0$; that is, only phonons

17

with very small momentum or multiple phonons whose momentum sums to zero can contribute to Raman signal.[77] Electrons scattered by defects can cancel the non-negligible momentum of an emitted phonon as well. Summarized in Figure 2.4, Raman spectroscopy data contains valuable information on the electronic structure, and thus the local defect structure, of graphene arising from various allowed transitions. Confocal Raman microscopy employs a monochromatic laser focused to spot-size nearing the diffraction limit to sample an area of hundreds of nanometers. The probe is scanned across an area of tens to hundreds of square microns, and spectroscopic mapping provides an image containing electronic and vibrational structure information.
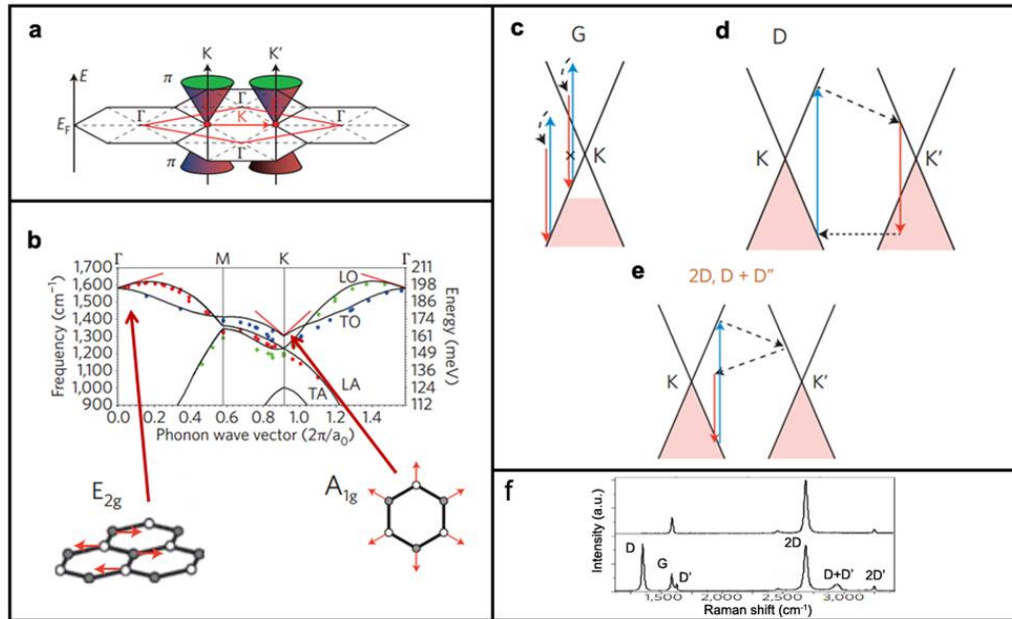


**Figure 2.4** The conical electronic band structure of graphene (a) enables a variety of intra- and interband electron relaxation processes. The phonon band structure (b) is dominated by modes away from the Γ-point which do not meet the fundamental Raman selection criteria. Zero-momentum one phonon processes (c) make up the G peak and

give insight on doping level; however, breathing modes with non-negligible momentum only contribute to the Raman spectrum if electron-defect scattering occurs (d) or for two-phonon processes (e). The observed spectrum (f) gives insight on the Raman processes occurring and thus the electronic and vibrational environment of graphene films. Adapted from ref. [77].

## 2.2 | Methods

### 2.2.1 | Sample Preparation and Characterization

*Polycrstalline Graphene Membranes*

Chemical vapor deposited (CVD) graphene was chosen as a specimen well aligned with the goals of this project. Aside from the industrial viability of the CVD process, CVD graphene is polycrystalline in nature, and its grain boundaries act as a well defined interface/defect for exploration with UEM. Graphene grown on a copper substrate was received from the Graphene Supermarket and displayed ~95% monolayer coverage of the substrate. In order to prepare free-standing graphene films suitable for TEM, substantial effort was put into developing a process to transfer the graphene from the copper substrate to a TEM grid. Traditional polymer transfer techniques[78] used in large scale transfer of graphene films generally result in a non-negligible amount of residual polymer molecules left of the surface of the film,[79] posing a problem for atomic-scale analysis. However, other direct techniques[80] avoiding the use of polymer do not have the capability to yield large area (>100 μm) films. A technique combining the benefits of these methods was developed in our lab and is shown schematically in Figure 2.5. A holey film of

amorphous carbon on a TEM grid is directly adhered to the surface of a graphene-on-copper coupon, and, after a mask is placed on the grid to prevent contact of the polymer with the graphene surface, a polymer is subsequently drop-cast on top of the grid for additional support. The copper is then etched away in an aqueous etching bath, and afterwards the polymer and mask are detached from the grid in an organic solvent leaving the graphene to blanket the grid's holey film.
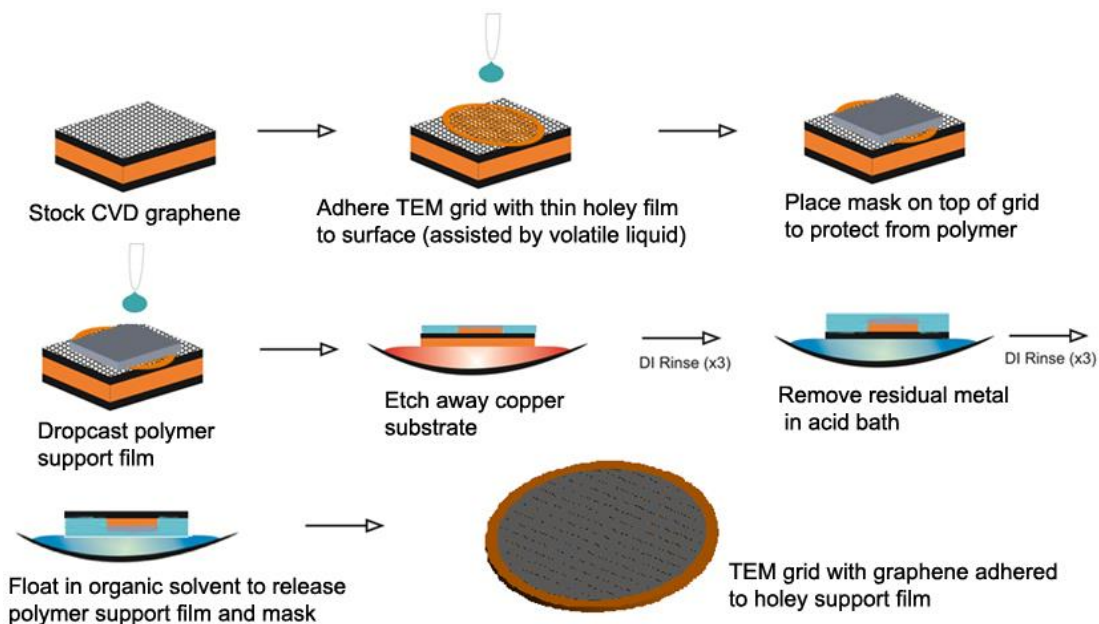


**Figure 2.5** A schematic representation of the semi-direct graphene transfer process. Avoiding direct contact of the polymer support with the graphene adhered to the TEM grid results in films that can be atomically clean.

The quality of the graphene film is verified with both TEM and Raman spectroscopy as illustrated in Figure 2.6. In low-magnification TEM images, subtle intensity variation between covered and uncovered holes in the support film is highlighted by contrast enhancement to determine the extent of graphene coverage. Although this technique

20

provides throughput comparable to optical microscopy, the existence of bilayers, wrinkles, and residual components from the transfer process remains unknown. Regions of interest are further probed with Raman spectroscopy to give sensitive information on these features, verifying the pristine nature of the free-standing graphene. Crystallinity of the specimen is determined with selected-area electron diffraction (SAED) within the TEM, and individual grains can be visualized in DF-TEM images. Shown in Figure 2.7, composite DF-TEM images of different crystalline domains highlight the grain boundaries present, and SAED diffraction patterns reveal the angular orientation of the grains which define the interface. The visualization of domains corresponding to specific diffraction spots provides a valuable link between real-space and reciprocal-space to be exploited in ultrafast electron crystallography experiments.
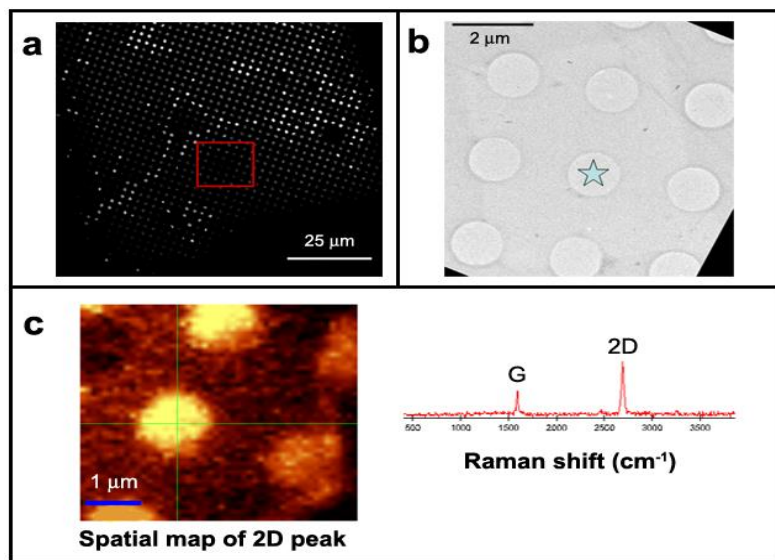


**Figure 2.6** Determining high-quality, suspended areas of monolayer graphene. Low-magnification, contrast-enhanced TEM images (a) reveal coverage of the holey support film. Bright-field TEM images (b) of regions of interest (square in a) are compared with

21

Raman maps (c) to verify the pristine nature of the films. A representative spectra taken at the star in (b) is shown.
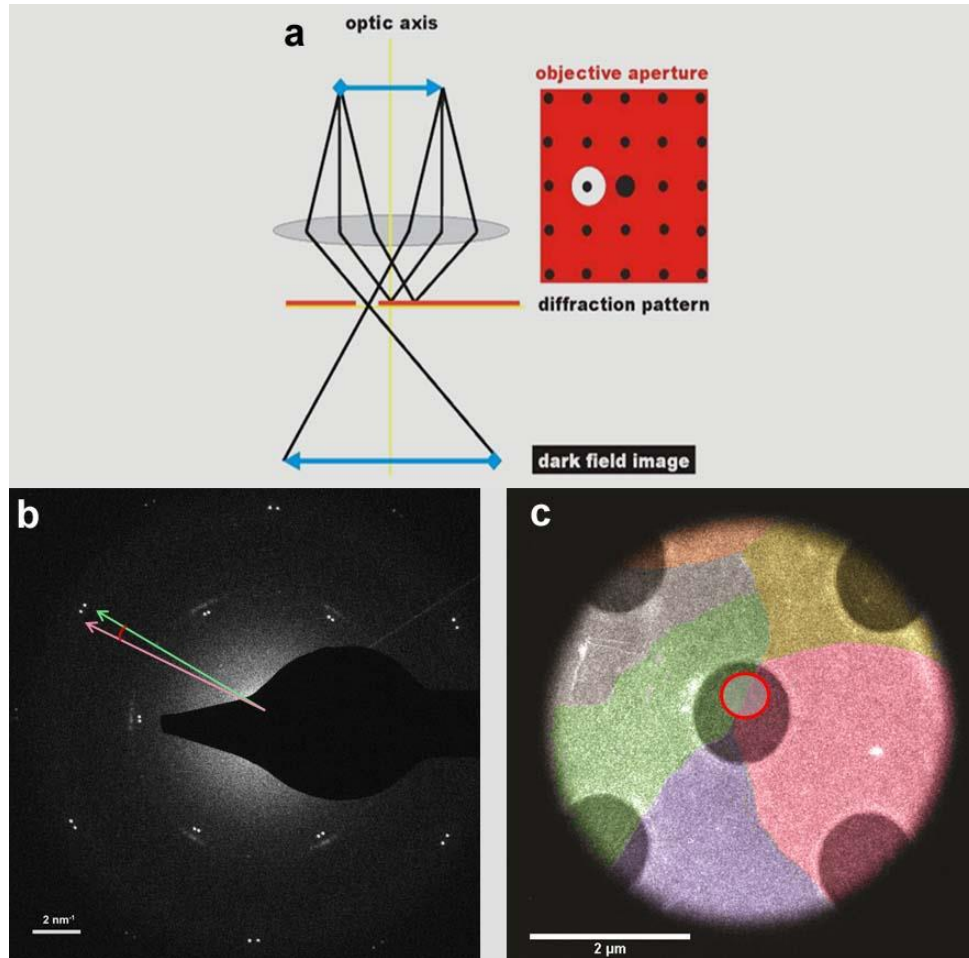


**Figure 2.7** Characterization of graphene grain structure. Dark field images obtained by using only a specific beam of diffracted electrons, schematically shown in (a), allow for visualization of specific crystal domains. An aperture is placed in front of a beam chosen from the SAED pattern (b) and composite images (c) are false colored to highlight the interfaces between the grains.

*Exfoliated Flakes of TMDCs*

Few-layer $WSe_2$ (2-H) and $TaS_2$ (1-T) flakes were prepared via mechanical exfoliation of a single-crystals obtained from Nanoscience Instruments ($WSe_2$) and HQ-Graphene ($TaS_2$). Isolated flakes were transferred to an atomically-flat, cleaved (100) NaCl substrate (Ted Pella) before a polymer support film was deposited by drop-casting 20 µl of a solution of 2-wt% polymethyl methacrylate (PMMA) in anisole. The NaCl substrate was etched for 10 to 15 minutes in a DI water bath, leaving the flakes supported by the PMMA film. The specimens were then positioned on various TEM supports (2000- and 1000- mesh Cu grids, as well as holey $Si_3N_4$ support films) via micromechanical manipulation followed by dissolution of the PMMA support film in an acetone bath overnight.

In order to locate and characterize specific defects and other nanoscale imperfections of interest, the few-layer flakes were initially surveyed using bright-field imaging and parallel-beam electron diffraction. Static structural and morphological characterization of specific specimen regions of interest, on which subsequent fs electron imaging studies were conducted, are summarized in Figure 2.8. As can be seen from the diffraction patterns, the $WSe_2$ are oriented such that the electron beam travels approximately down the [001] zone axis, respectively [Fig. 2.8(c)]. Combined, the bright-field images and corresponding diffraction patterns illustrate the macroscopically-crystalline but microscopically-disordered nature of the regions. From the images, several features of interest for the present study can be identified, which, conversely, are not readily apparent from the diffraction patterns alone. These include step-edges and

terraces, wrinkles, folds, vacuum-crystal interfaces, and cracks. In addition, bend contours are quite prominent and widespread, as are Moiré fringes in the $WSe_2$ specimen.
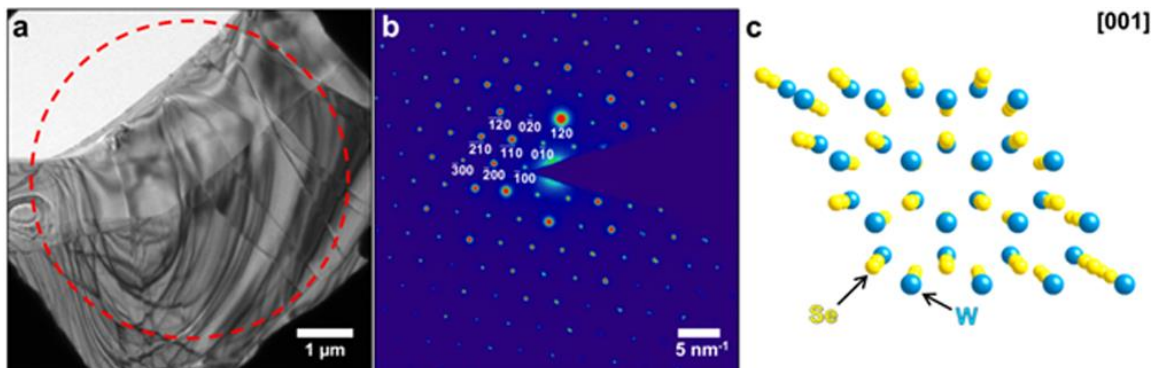


**Figure 2.8** Morphological heterogeneity and atomic-scale order of $WSe_2$ specimens. (a) Bright-field images of (a) a few-layer $WSe_2$ flake. The red, dashed circle denotes the position of the selected-area aperture used to generate the diffraction patterns shown in panels (b). Scale bars = 1 µm. (b) Corresponding selected-area diffraction patterns obtained approximately along the [001] with several Bragg spots indexed. Scale bars: (b) = 5 nm$^{-1}$. (c) Crystal structures of $WSe_2$, as viewed down the [001] zone axis. In (c): yellow spheres = Se; blue spheres = W, as labeled.

*TaS₂ Characterization*

The as-obtained $TaS_2$ was of the 1T-polytype; however, after exfoliation and transfer we observed a variety of polytypes. Shown in Figure 2.9, we observe superlattices in electron diffraction characteristic[81] of both the 1T-polytype [Fig. 2.9B] and the $4H_B$-polytype [Fig. 2.9D]. Each polytype has unique stacking of layers and coordination of atoms. The 1T-polytype consists of octahedral coordinated layers stacked directly on top of one another (unit cell shown in [Fig 2.9A]), while the $4H_B$-polytype consists of alternating layers of trigonal prismatic and octahedral coordination (unit cell

shown in [Fig. 2.9C]).[82] Each of these polytypes also display dissimilar bright-field contrast; the stripy, Moiré-type contrast is characteristic of the 1T-polytype, while the fragmented dislocation facilitated contrast occurs for the $4H_B$-polytype. While the stripy contrast is generally negligibly effected by laser –excitation, the fragmented "gates" such as those in Fig. 2.9C often chaotically change morphology. We believe this arises from dislocation motion arising from shear waves formed via laser excitation.
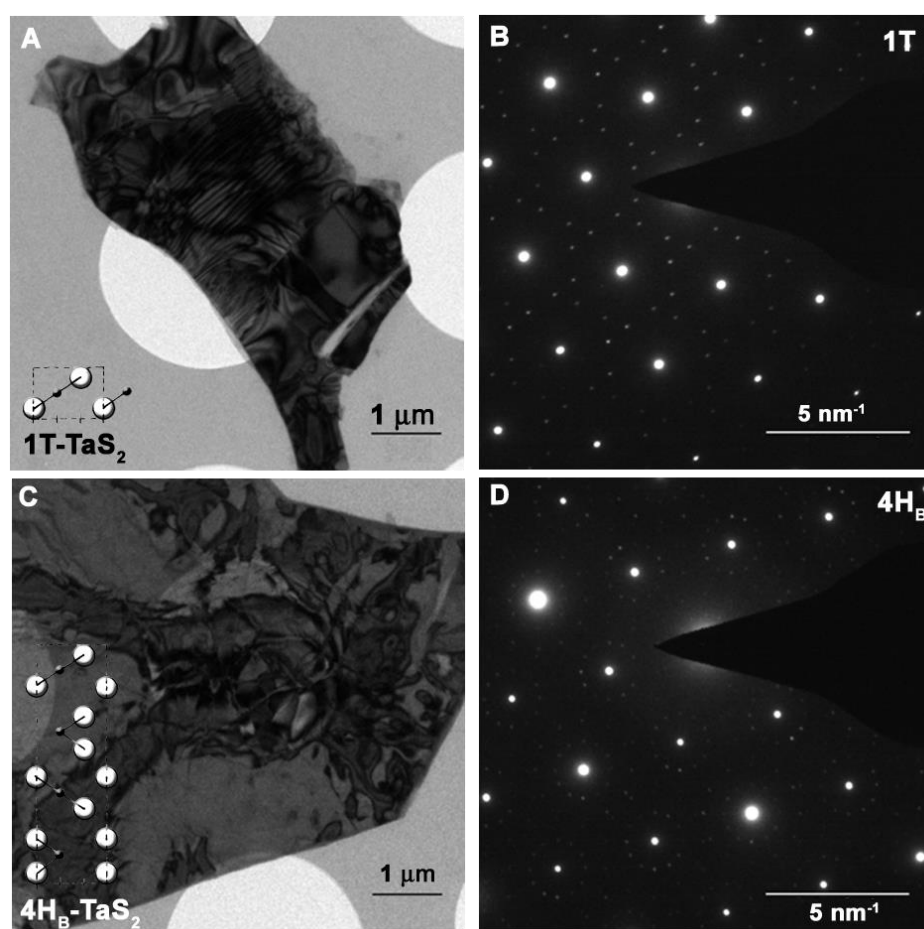


**Figure 2.9** Bright-field images and selected area electron diffraction of 1T- and $4H_B$-polytypes of $TaS_2$. (A, C) Bright-field images of flakes of 1T- (A) and $4H_B$- (C) $TaS_2$.

Their stacking structure is schematically shown down the [010] zone. (B, D) Electron

diffraction from 1T- (B) and 4H$_B$- (C) flakes.

Indeed, these different structures facilitate different charge-order superstructures

with varying thermodynamic stability. At room temperature, we observe a nearly

commensurate $\sqrt{13}a_0$ superlattice in the 1T-flake and a $13a_0$ superlattice in the 4H$_B$-flake.

The hypothesized structures illustrated in real-space are shown in Figure 2.10. The

superlattice observed in the 4H$_B$-flakes arises from superposition of alternating domains

of the $\sqrt{13}a_0$ structure rotated ~28° with respect to one another.[82] At elevated temperature

(above ~340 K), both polytypes show an incommensurate phase.
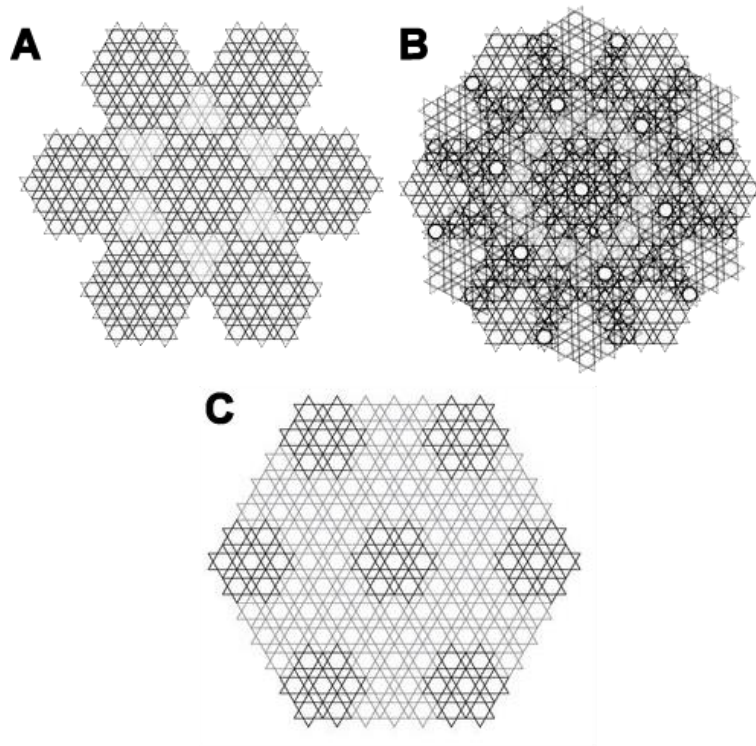


**Figure 2.10** Illustration of charge-order structures in real-space. (A) Nearly-

commensurate phase common in 1T-flakes with a $\sqrt{13}a_0$ superlattice. (B) Textured

nearly-commensurate phase observed in 4H$_B$-flakes in which two nearly commensurate

domains rotated 28° with respect to one another are superimposed. (C) Incommensurate phase observed for both polytypes at higher temperatures.

2.2.2 | Characterization of Instrument Response

Temporal overlap of the pump laser pulse and probe photoelectron packet was determined via a plasma-lensing effect.[83, 84, 85] The specimen target used here was a 1000-mesh Cu TEM grid (Ted Pella). Each experiment consisted of a series of low-magnification bright-field UEM images of a single grid square acquired at different time delays (Figure 2.11a). Difference images generated from averaged pre-time-zero frames contain contrast arising only from the lensing effect. Analysis of the image series enables determination of time zero (defined as the time at which the image-intensity change reaches 50%) and the instrument-response time ($\sigma_t$), assuming plasma generation occurs on a timescale much shorter than the pump-pulse duration. Space-time contours generated by averaging along the Y-direction in the difference images at each time point illustrate the varied temporal response that occurs throughout the vacuum region within the grid square (Figure 2.11b). To ensure sampling of only pseudo-instantaneous dynamics, time traces having maximum spatial gradients in the difference images were isolated (vertical red line in Figure 2.11b). The extracted traces are normalized to the second percentile, baseline subtracted, and then fit with the function shown in Equation 2.1 below:

$$I(t) = \frac{A}{2}\left[\text{erf}\left(\frac{t-t_0}{\sqrt{2}\sigma_t}\right) + 1\right] \qquad \text{(E2.1)}$$

27

Here, $A$ and $t_0$ are the extracted amplitude and time-zero position, respectively. Note that $\sigma_t$ is the standard deviation of a Gaussian peak function (*i.e.*, the derivative of Equation 1).
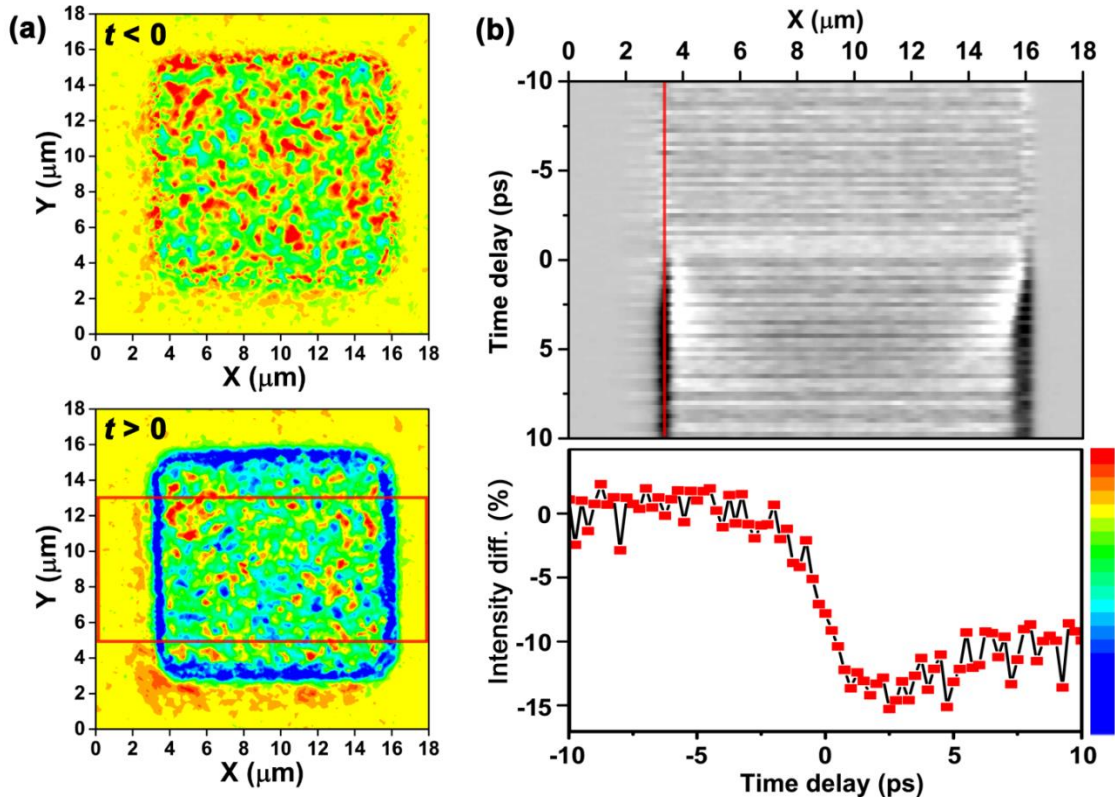


**Figure 2.11** Plasma lensing, time zero, and instrument-response time via bright-field UEM imaging. (a) Low-magnification difference images of a 1000-mesh Cu grid square acquired before (upper panel, $t < 0$) and after (lower panel, $t > 0$) time zero. The color bar [shown to the right of the time trace in (b)] for the image false coloring shows cooler colors indicate electron depletion (*i.e.*, a reduction in image intensity). The red box in the lower panel indicates the area over which the space-time contour plot in (b) was generated. The unchanged yellow border is the Cu grid, and the centered square (within which the intensity change occurs) is vacuum. (b, upper panel) Space-time contour plot

28

generated by averaging over the Y image direction for each time delay. The red vertical line near X = 3.7 μm is the region from which the time trace was generated. (b, lower panel) Time trace illustrating the instrument-limited onset of electron depletion (*i.e.*, the blue region in the difference images).

Response times are extracted from the spatiotemporally-varying contrast illustrated in Figure 2.12a via systematic image analysis aimed at avoiding experimenter bias. For a particular image scan, kinetic traces are extracted for each edge of a copper grid square that is observable within the field of view (*e.g.*, nine grid squares and 36 total edges at a UEM magnification of 120x). Shown in Figure 2.12b, appropriate kinetic traces are selected from the spatially-varying contrast dynamics by isolating the temporal response at inflection points near the grid edges (red squares in Figure 2.12b). For each edge of a grid square, a dynamic trace is generated (*e.g.*, Figure 2.11b), to which Equation 2.1 is fit. Following this, the value of $\sigma_t$ that is reported here and in the main text is the median value of all the extracted fits for a given experiment that meet the following criteria: (1) the amplitude ($A$) is larger than 0.85 and (2) the residual norm is less than three times the minimum residual norm observed for that experiment. These criteria were chosen in order to eliminate artifacts resulting from regions where the signal-to-noise ratio was insufficient for extraction of a dynamic response.
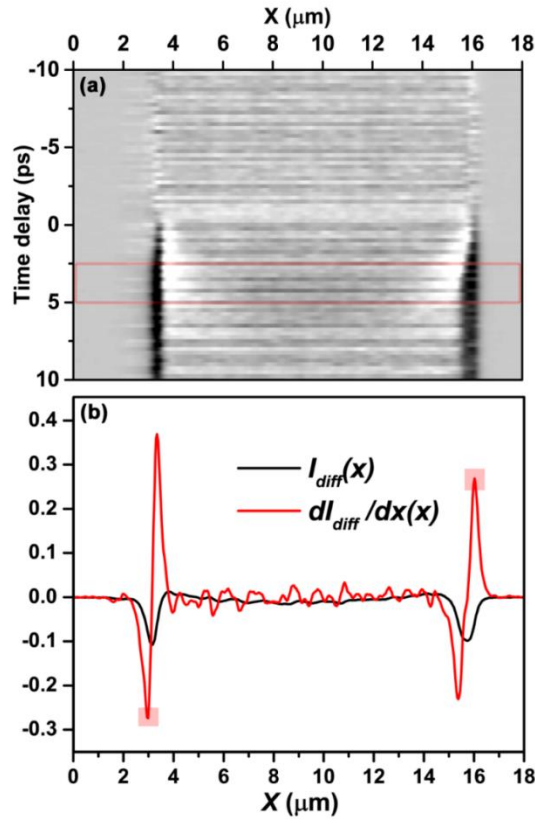
**Figure 2.12** Isolating pseudo-instantaneous plasma-lensing dynamics. (a) Space-time contour plot generated from the spatial-averaging method discussed in main text. The red box indicates the time-averaged region from which the spatial trends shown in (b) are plotted. (b) Spatial variance ($I_{diff}$, black) and gradient ($dI_{diff}$, red) of time-averaged difference images generated from pre-time zero images. The red, partially-transparent boxes indicates the spatial region from which the kinetic traces are generated; these are the inflection points of differential intensity occurring at the edge of the grid square.

2.2.3 | Stroboscopic Bright-field Imaging and Diffraction Parameters

All ultrafast experiments were performed with a Tecnai Femto ultrafast electron microscope (FEI Company) operated at 200 kV in both thermionic and photoelectron modes. In both modalities, truncated, flat $LaB_6$ cathodes (Applied Physics Technologies)

30

are used. We have found that 50- and 100-μm flat (diameter), LaB$_6$ photocathodes encircled with a concentric graphite ring (65- and 40-μm in annular width, respectively) improve beam stability and reduce deleterious emission from the shank portion of the cathode assembly. The 50- and 100-μm cathodes were positioned 250 and 350 μm, respectively, behind the Wehnelt aperture within the cylinder; indeed, positioning the cathode within the Wehnelt assembly affects collection efficiency into the illumination system of the Tecnai Femto, and we aim to systematically determine optimal positions in future work.[44] In order to capture the greatest number of photoelectrons at the relatively low repetition rates used here (i.e. 5 to 50 kHz), a custom 1,250-μm condenser aperture and 2-mm Wehnelt aperture was employed for all experiments. For all bright-field experiments, a 40-μm objective aperture was used. For all selected-area diffraction experiments, a 200-μm projection aperture was used, which collected electrons passing through a 20-μm$^2$ area. Images were recorded with a Gatan Orius SC200B 2,048 x 2,048 CCD camera and with integration times ranging from 10 to 45 seconds per frame. Based on the total electron counts [approximately ($1 \times 10^8$) to ($5 \times 10^8$)] acquired with the beam focused to the size of the CCD chip for a given exposure time and repetition rate, it is estimated that 200 to 1,000 electrons per pulse were used for image formation.

2.2.5 | Control Experiments

In order to exclude a host of potential artifacts and undesirable instabilities of the experimental system as the cause of the observed propagating contrast waves, a series of control experiments are typically performed immediately following successful scans (i.e. those in which we believe dynamics occur) using the same experimental parameters. (1)

A control experiment for specimen drift/tilt is performed by acquiring images at a fixed time delay (*e.g.*, -100 ps) in order to replicate the duration of a full time scan (*e.g.*, 20 minutes). (2) A control experiment for image fluctuations due to potential photoelectron-source instabilities is performed by acquiring images over ~20 minutes without specimen excitation. (3) A control experiment for beam instabilities due to movement of the delay stage is performed by acquiring images without specimen excitation but still translating the delay stage on the laser table as if a scan were being performed. (4) A control experiment for the equilibrium thermal effects of pumping the specimen is performed by acquiring a series of images over ~10 minutes spanning a delay range but using a thermionic rather than photogenerated electron beam. These control experiments separate real-time specimen or environmental instabilities from stroboscopic dynamics.

## 2.3 | Summary

In this chapter we have summarized important equipment and unique methodology, largely developed within our group, critical to the goals of this project. Operating principles of conventional TEM, UEM and Raman spectroscopy were described, and specimen preparation and characterization procedures specific to graphene, $WSe_2$, and two polytypes of $TaS_2$ were outlined. Additionally, we have presented framework for experiments unique to UEM including plasma-lensing instrument response characterization, fs- imaging and diffraction, and the appropriate controls. The methods here form the basis for observations described throughout the dissertation.

# 3 | *In-situ* and Correlative Investigation of Thermal Transport in Single-Layer Graphene

In this chapter, we summarize our efforts to develop a robust platform for investigating phonon transport in suspended monolayer graphene with various crystallographic and morphological defects such as grain boundaries. Implementing an opto-thermal Raman thermometry technique[86, 87] on membranes with precisely characterized grain structure unveils the functional dependence of thermal conductivity of grain size, revealing contributions to phonon scattering within the lattice and at grain boundaries. Examining the nature of the phonon modes, however, requires atomic sensitivity, and as such we implement in-situ selected area electron diffraction (SAED) as a probe of elastic scattering suppression arising from laser-excited atomic-displacements via extraction of the Debye-Waller factor (DWF). Additionally, we employ diffraction spots corresponding to individual grains act as indicators of vibrational amplitudes within confined grains. We find that the two techniques offer auxiliary information and discuss potential extension of the in-situ technique to the stroboscopic domain to examine phonon scattering processes on their native time-scale.

## 3.1 | Opto-thermal Raman Measurement of Grain-Size-Dependent Thermal Conductivity

### 3.1.1 | Overview of Technique

To examine the effect of varying grain structure on the mechanical and thermal properties of suspended graphene membranes, graphene grown on a copper substrate via chemical vapor deposition (CVD) was transferred to a holey silicon nitride TEM grid (see methods). While the as-grown CVD graphene is nominally polycrystalline with average grain sizes of a few microns, the effective grain sizes of the suspended membranes depend on the portion of the graphene which cover the ~2.5 μm holes in the $Si_3N_4$ film and vary from a couple hundred nanometers to a couple microns (i.e. a single grain covers the hole).

Two analogous laser-heating techniques were used to discern both thermal and mechanical properties of the suspended membranes. The first, a confocal Raman microscopy setup outlined in Figure 3.1, relies on continuous wave laser light focused to near the diffraction-limit by an objective lens to both locally excite membranes and probe their temperature via bond-softening peak-shifts in the resulting Raman spectra (Fig. 3.1C). As previously described for graphene[86, 87] and other suspended thin films,[88, 89, 90] the thermal conductivity of the membrane, $k$, is related to the change in G-peak position for a given change in power absorbed ($\delta\omega_G/\delta P$) by Equation 3.1:

$$k = \chi_G \alpha (\tfrac{1}{2} h\pi)(\tfrac{\delta\omega_G}{\delta P})^{-1} \qquad (E3.1)$$

34

where $\chi_G$ is linear coefficient describing peak shift as a function of temperature, $\alpha$ is the percentage of laser light absorbed by the graphene, and $h$ is the thickness of the graphene film. In this manner, the effective thermal conductivities of various membranes can be extracted from raster-scans over the specimen (Fig. 3.1B) at varying laser power by tracking the G-peak positions of spectra taken in the center of the membranes (Fig. 3.1D).
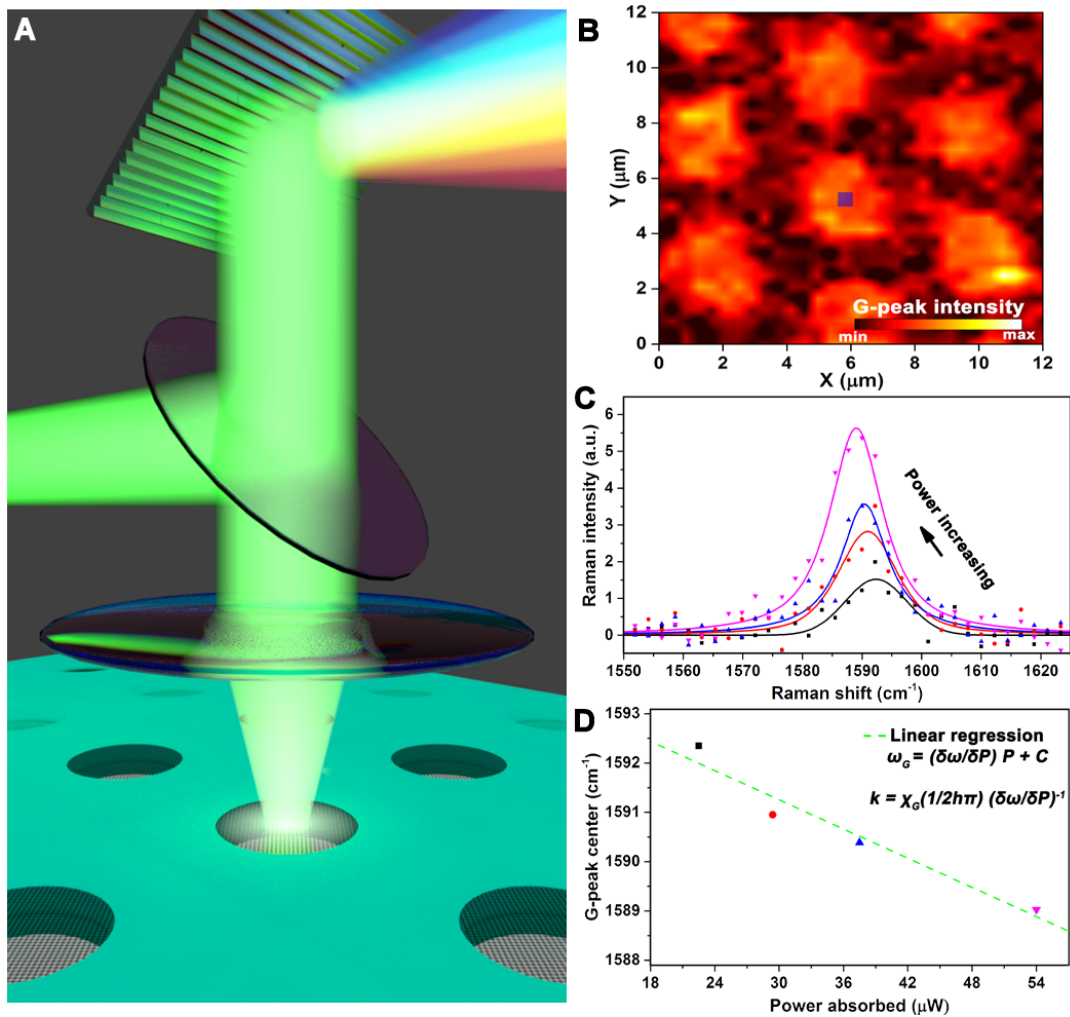


**Figure 3.1** Micro-Raman thermal conductivity measurements. (A) Schematic illustration of the opto-thermal Raman method in which focused laser light locally heats a suspended membrane of monolayer graphene. (B) Raman map of the G-peak intensity of several

suspended membranes. The blue square marks the pixel in which spectra are analyzed to determine thermal conductivity. (C) Raman spectra taken at the from the blue square in (B) at increasing laser power (D) Extracted G-peak centers for the spectra in (C) and the resulting slope (dotted green line) are used to determine the thermal conductivity of the membrane via Equation 3.1.

### 3.1.1 | Grain-size dependent Behavior

Thermal transport measurements were conducted on layer-area regions of the transferred graphene free of wrinkles, tears, edges, residual polymer/copper from the transfer process, and bi-/tri-layer islands. Conducting the experiments on TEM grids allowed for post-measurement inspection of the selected membranes for morphological defects and correlative identification of the grain structure. Shown in Fig. 3.2, average grain sizes were quantified by acquiring electron diffraction patterns illuminating the suspended portion of the membranes and azimuthally integrating the (110) peaks; the geometric mean of the amplitudes of all identified peaks is used to quantify a characteristic grain size for each membrane. In Fig. 3.2C, a clear decline in thermal conductivity is observed with decreasing grain size, reducing by about a factor of five from the effectively single-crystal membranes to the smallest grain size (~400 nm). As previously observed,[56] the effective thermal conductivities show a Matthiessen's-rule type behavior whereby the inverse of the effective thermal conductivity, $k^{-1}$, is related to contributions from within the lattice and from defects (i.e. grain boundaries) by:

$$k^{-1} = k_g^{-1} + L^{-1}G_B^{-1} \qquad \text{(E3.2)}$$

where $k_g$ is the thermal conductivity of the lattice, $L$ is the grain size, and $G_B$ is the thermal boundary conductance at the grain boundaries. With this model, we extract a thermal boundary resistance of $\sim 5*10^8$ Wm$^{-2}$K$^{-1}$ and a lattice thermal conductivity of $\sim 5400$ Wm$^{-1}$K$^{-1}$.
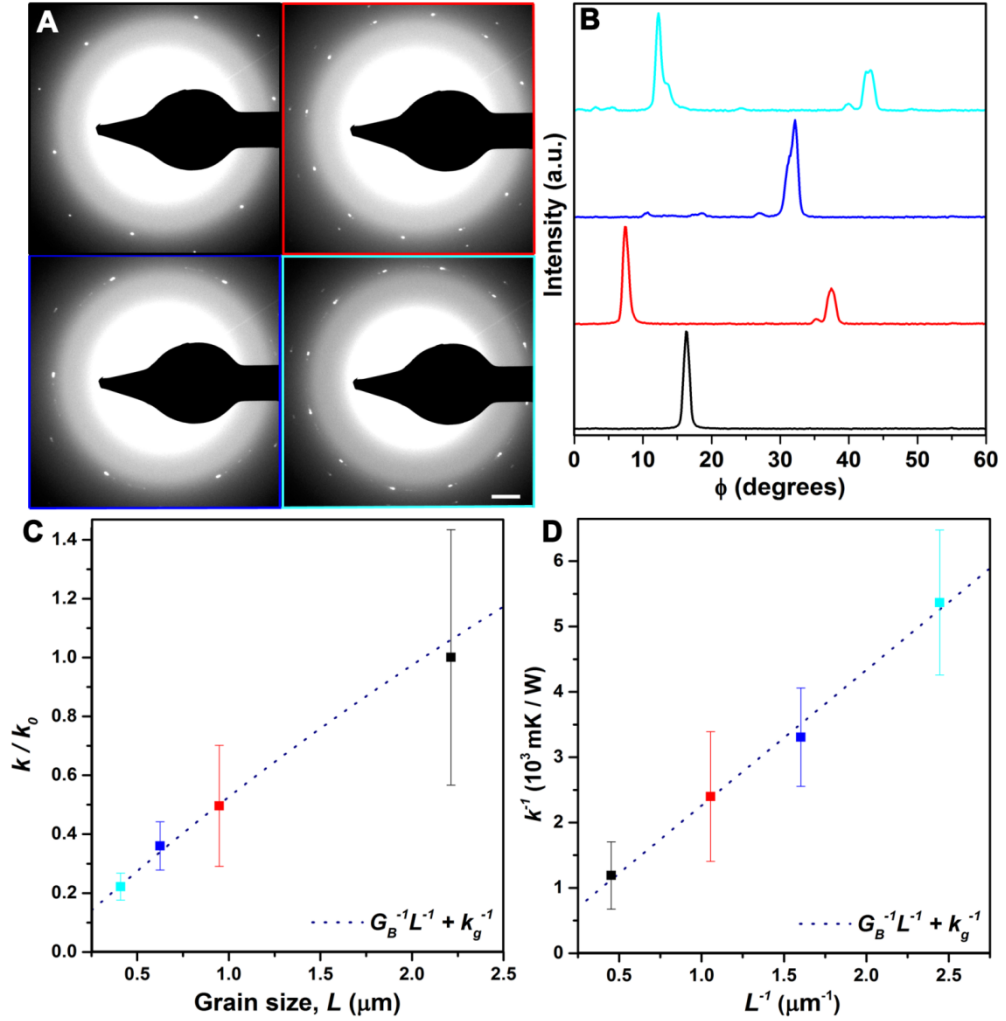


**Figure 3.2** Thermal conductivity versus grain size. (**A**) Thresholded electron diffraction patterns acquired for four membranes (denoted with a corresponding color border) examined with the micro-Raman technique. The patterns were acquired with the beam illuminating the entire suspended portion of the membrane. (**B**) Normalized azimuthally

integrated traces of the (110) reflection used to measure grain sizes for the membranes examined. The plots are offset for clarity. (**C**) Thermal conductivity (normalized to that observed for a membrane with a single grain) versus grain size and the Equation 3.2 fit (dashed blue line) Error bars represent propagated normal error of the slopes in linear fitting of $\omega_G$ versus $P$.

While the observed lattice thermal conductivity and thermal boundary resistance are reasonably consistent with accepted literature values ($k_g = $ ~5200 Wm$^{-1}$K$^{-1}$; $G_B = 10^9$ to $10^{11}$ Wm$^{-2}$K$^{-1}$),[56, 86] it is important to note potential sources of error and ambiguity in the measurement technique.[91] First, we assume that for each membrane the graphene absorbs 2.3% of the incident light and the G-peak shows a linear dependence on temperature for the given range of laser-powers (i.e. $\omega(T) = \omega_0 + \chi_G T$, with $\chi_G$ taken as -1.6 $*$ 10$^{-2}$ cm$^{-1}$/K) for each membrane. Additionally, it is assumed that the relevant spectra are acquired with the laser precisely centered in the membrane. As the extracted thermal conductivities are sensitive to the absorbed power term and the bond-softening coefficient $\chi_G$ via Equation 3.1, we expect these inferred conditions to be primary sources of systematic error in the measurements. The relative values of thermal conductivity (i.e. normalized to the quantity observed for the effectively single-crystal membrane), however, are likely more precise given that the uncertain quantities of $\alpha$ and $\chi_G$ have been divided out. It is important to note that, while Raman measurements of effective membrane thermal conductivity give estimates of the contributions to phonon-scattering of the GBs collectively, we obtain no insight into the scattering behavior of individual GBs which may vary significantly depending on their misorientation angle and

morphology.[92, 93] This type of insight would require experimental determination of temperature profiles within individual grains and across isolated grain boundaries.

## 3.2 | Atomic Vibrations in Suspended Single-Crystal and Polycrystalline Membranes

### 3.2.1 | *In-situ* SAED of Laser-Heated Membranes

While the micro-Raman technique is a widely used tool for examining thermal properties of suspended thin films, we aimed to develop an analogous technique for membranes heated *in-situ* inside a TEM such that local vibrational amplitudes could potentially be probed from smaller sample regions via selected area electron diffraction and with simultaneous knowledge of grain structure and grain boundary morphology. Illustrated in Fig. 3.3, the membranes are excited with 515 nm laser light directed to the specimen region with a periscope and aluminum mirror near the TEM column. An aperture is placed in an intermediate image plane below the objective lens such that only electrons scattered from the selected sample area (i.e. the bright circle in Fig. 3.3C) contribute to the observed diffraction patterns. Local vibrational amplitudes – that is, the mean squared displacements of atoms $<U^2>$ – are then extracted via measurement of the Debye-Waller factor in observed elastic scattering. For unperturbed membranes at room temperature, absolute Debye-Waller factors are obtained by fitting the electron counts, $N_p$, versus scattering vector, $G$, with a previously described model:[94]

$$N_p = \frac{I_0}{(\mu^2+G^2)^2}\exp(-<U^2>G^2) \quad \text{(E3.3)}$$

where the free parameter $I_0$ is a constant encompassing non-scattering-vector-dependent quantities including beam-current, and $\mu$ is the inverse Coulomb screening length. For excited membranes, we measure the change in $<U^2>$ by tracking the suppression of elastic scattering of the excited membranes as compared to the unperturbed membranes. In this case, the log of the intensity ratio, $I/I_0$, is linearly proportional to the squared scattering vector magnitude, $G^2$, as:

$$-LN\left(\frac{I}{I_0}\right) = \Delta < U^2 > G^2 + C \qquad \text{(E3.4)}$$

In this manner, the local, laser-induced thermomechanical modulations in the lattice are measured as a function of excitation power (Fig. 3.3G).
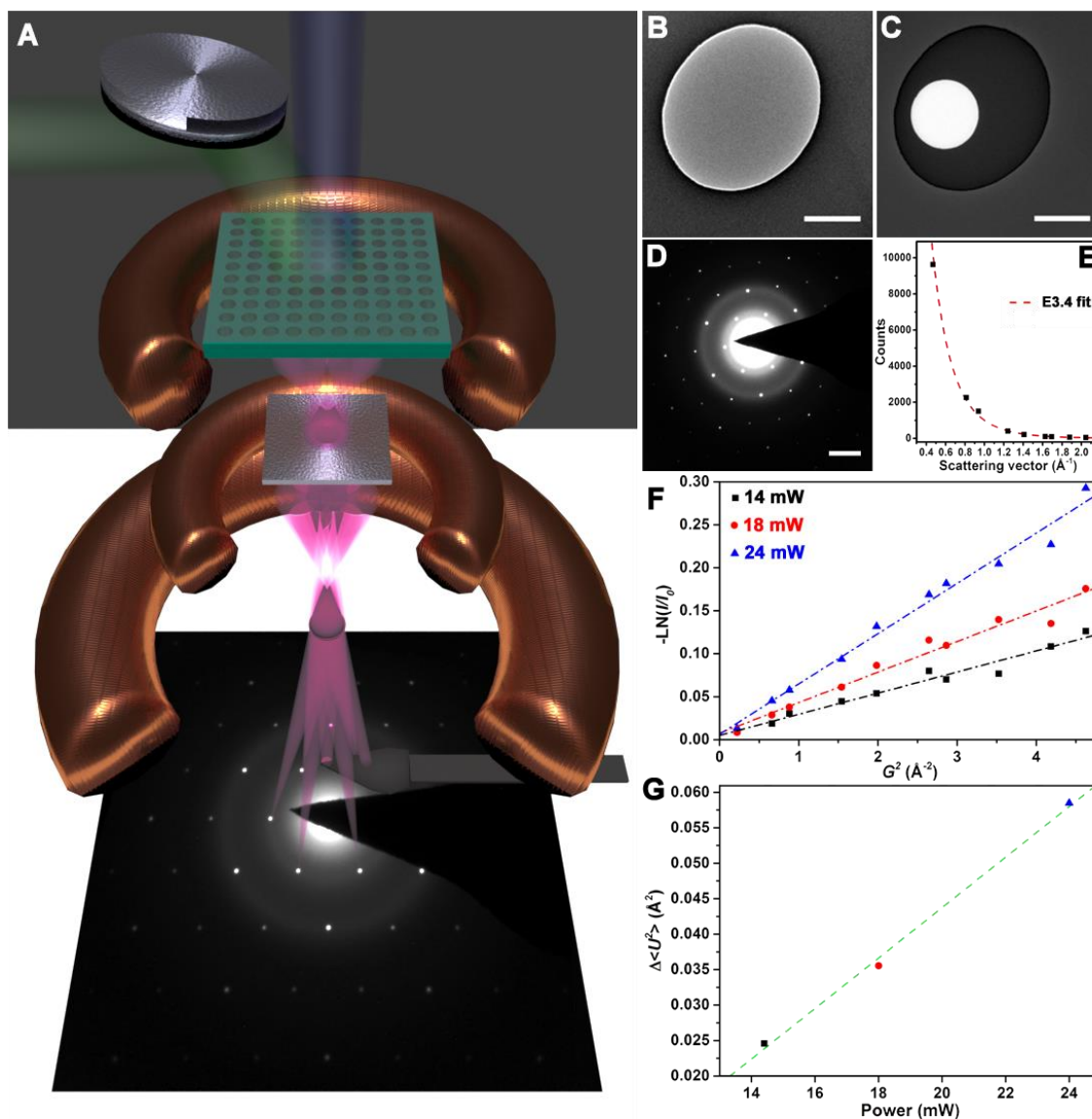
**Figure 3.3** *In-situ* selected area electron diffraction of laser-heated graphene membranes.

(**A**) Schematic illustration of laser-heating in the TEM and the formation of selected-area

diffraction patterns from elastic scattering (pink beams). Laser-light (515 nm) is directed

to the specimen region by an aluminum mirror and excites a ~120 μm area. (**B**) Bright-

field image of a graphene membrane (scale bar: 1 μm) (**C**) Composite bright-field image

displaying the selected region (white circle) which contributes to the observed electron

diffraction. Scattering from the region is isolated via insertion of an aperture [metallic square in (A)] in an intermediate image plane. (**D**) Selected-area diffraction pattern of a single-crystal membrane (scale bar: 0.5 Å$^{-1}$) (**E**) Plots of electron counts versus scattering vector enable extraction of the Debye-Waller factor via Equation 3.4. (**F**) Plots of − LN($I/I_0$) versus $G^2$ are used to monitor changes in the amplitudes of atomic vibrations (i.e. $\Delta<U^2>$) for varying laser power. (**G**) Extracted $\Delta<U^2>$ values linearly increase with laser power.

3.2.2 | Mean-squared Displacements in Single-Crystal Membranes

To evaluate the utility of SAED as a non-contact thermal probe sensitive to individual grains, we obtained measurements of the DWF for both single-crystal and polycrystalline graphene membranes excited with 515nm laser light. Illustrated in Figure 3.4 for the effectively single-crystal membranes, the intensity of diffraction spots out to tenth-order were tracked as a function of laser power and used to extract the mean-squared atomic displacements. Fitting electron counts to Equation 3.4 for diffraction patterns acquired with the laser off (Fig. 4D), we find values of $0.22 \pm 0.05$ Å$^2$ and $0.47 \pm 0.08$ Å$^{-1}$ for the room-temperature mean-squared displacements $<U^2>$ and inverse Coulomb screening length $\mu$, respectively.
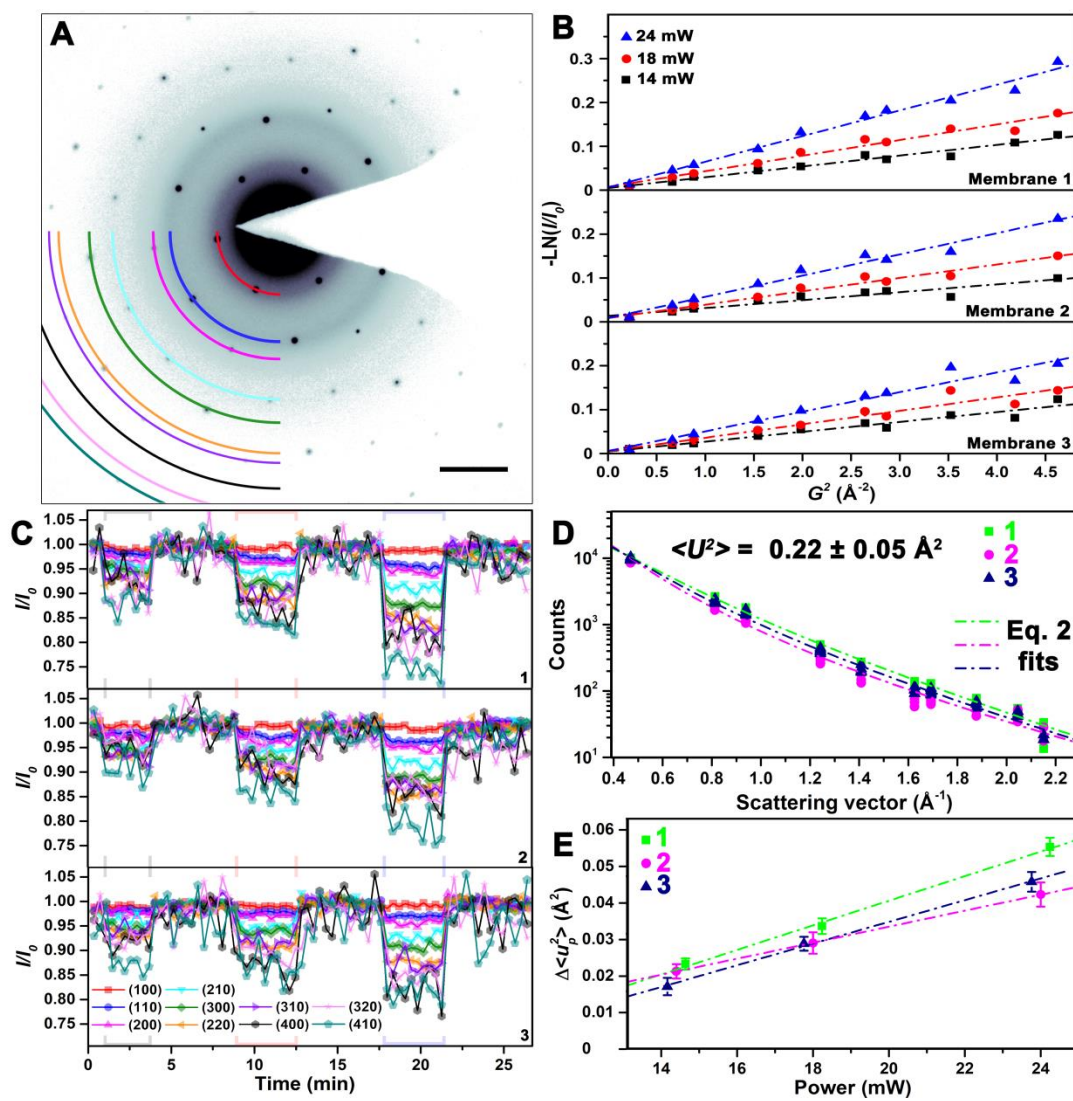
**Figure 3.4** Non-excited and laser-excited mean-squared displacements of single-crystal membranes. (**A**) Example selected-area diffraction pattern of a single-crystal graphene membrane (scale bar: 0.5 $\text{Å}^{-1}$) indexed by color arcs whose intensity are displayed in (C). (**B**) Plots of $-\text{LN}(I/I_0)$ versus $G^2$ with dashed lines representing linear fits used to extract $\Delta<U^2>$. (**C**) Intensities of diffraction spots out to tenth-order normalized to median laser-off values. The colored dashes on the x-axis represent the shutter opening and closing to direct 14 mW (black), 18 mW (red) and 24 mW (blue) of green laser power to the

specimen. (**D**) Plots of absolute electron counts versus scattering vector used to extract non-excited mean-squared amplitudes via fitting with Equation 3.4. (**E**) Extracted values of $\Delta{<}U^2{>}$ for three single-crystal membrane. Error bars represent normal error of slope from linear fitting of $-LN(I/I_0)$ vs. $G^2$. The data is offset marginally on the x-axis for clarity.

The surprisingly large values of $<U^2>$, corresponding to a root-mean-squared (RMS) displacement length of 0.47 Å (nearly a thrid of the carbon-carbon bond-length), likely arise from out-of-plane displacement contributions due to nanoscale corrugations in the suspended membranes. Indeed, contributions from in-plane ($U_{xy}$) and out-of-plane displacements ($U_z$) to the observed $<U^2>$ depend on the incidence angle $\theta$ of the electron beam as $<U^2> = (U_{xy}cos\theta)^2 + (U_z sin\theta)^2$.[95] While nominally the experiments were executed under normal incidence (i.e. down the [001] zone-axis), corrugations in the specimen result in tilting locally and allow for non-negligible contributions from of out-of-plane displacements. For reference, the corrugations observed by Meyer *et al.*,[60] with an average waviness of 5° and 5 Å amplitude (corresponding to an average out-of-plane displacement of ~3.2 Å), would lead to an observed RMS displacement length of ~0.28 Å, roughly half that observed here. Interestingly, previous measurements[94, 95] at normal incidence found RMS displacements about an order-of-magnitude lower than those observed here. We hypothesize that the disparity in suspended area results in varying degrees of corrugation in the suspended graphene and thus accounts for the dissimilar observations.

Shown in Fig. 3.4 B and C, we observe an additional suppression of elastic scattering upon laser excitation at three different powers, and the change in $<U^2>$ is extracted from the slope of the linear fits of $-LN(I/I_0)$ versus $G^2$. Plotted in Fig. 3.4E, $\Delta<U^2>$ increases linearly with excitation power from ~0.02 $\text{Å}^2$ to ~0.05 $\text{Å}^2$ for each membrane over the given power range. Notably, we do not observe an increase in strain greater than 0.1% for any membrane at any laser power. The absence of in-plane thermal expansion upon the large increase in atomic displacements (RMS ~0.14 Å to ~0.22 Å) implies that out-of-plane displacements from increased corrugation amplitude likely account for the observations; in other terms, the power absorbed by the membranes results in further population of out-of-plane flexural phonon modes. Additionally, the increased width of high-order diffraction spots upon increasing laser power indicates the Ewald sphere intersects widened rel-rod cones, confirming a variance increase in the surface normals associated with heightened corrugation amplitude.

3.2.3 | Mean-squared Displacements in Polycrystalline Membranes

Similar experiments were also performed on two polycrystalline graphene membranes whose SAED patterns are shown in Fig. 3.5 A & B. In this case, the integrated intensity of the first six radii were tracked as a function of laser power (Fig. 3.5 C & D), and modulations of $<U^2>$ were extracted from plots of $-LN(I/I_0)$ versus $G^2$ (Fig. 3.5 E). We performed the same radial-integration technique on the single-crystal membranes such that direct comparison between the membranes remains appropriate (indeed, the two data-analysis techniques performed show similar results). The $\Delta<U^2>$ versus laser power plots in Fig. 3.5 F indicate that no statistically significant differences

were observed between the two polycrystalline membranes or as compared to the single-crystal membranes. We should note here that, while the laser spot-size (<1 μm FWHM) in the opto-thermal Raman technique results in heat-dissipation occurring entirely within and at the boundaries of a single membrane, the laser spot-size exciting the specimen in the TEM (~120 μm FWHM) is much larger than the membrane radii. As a result, the observed pseudo-steady-state temperatures of the membranes are largely dictated by the heat dissipation conditions of the supporting grid and holey $Si_3N_4$ film, and measurements are insensitive to minor variations in thermal transport properties of different membranes. Nonetheless, it is interesting that equally large displacement amplitudes are observed for the polycrystalline membranes, indicating population of out-of-plane phonon modes also occurs in smaller grains.



46
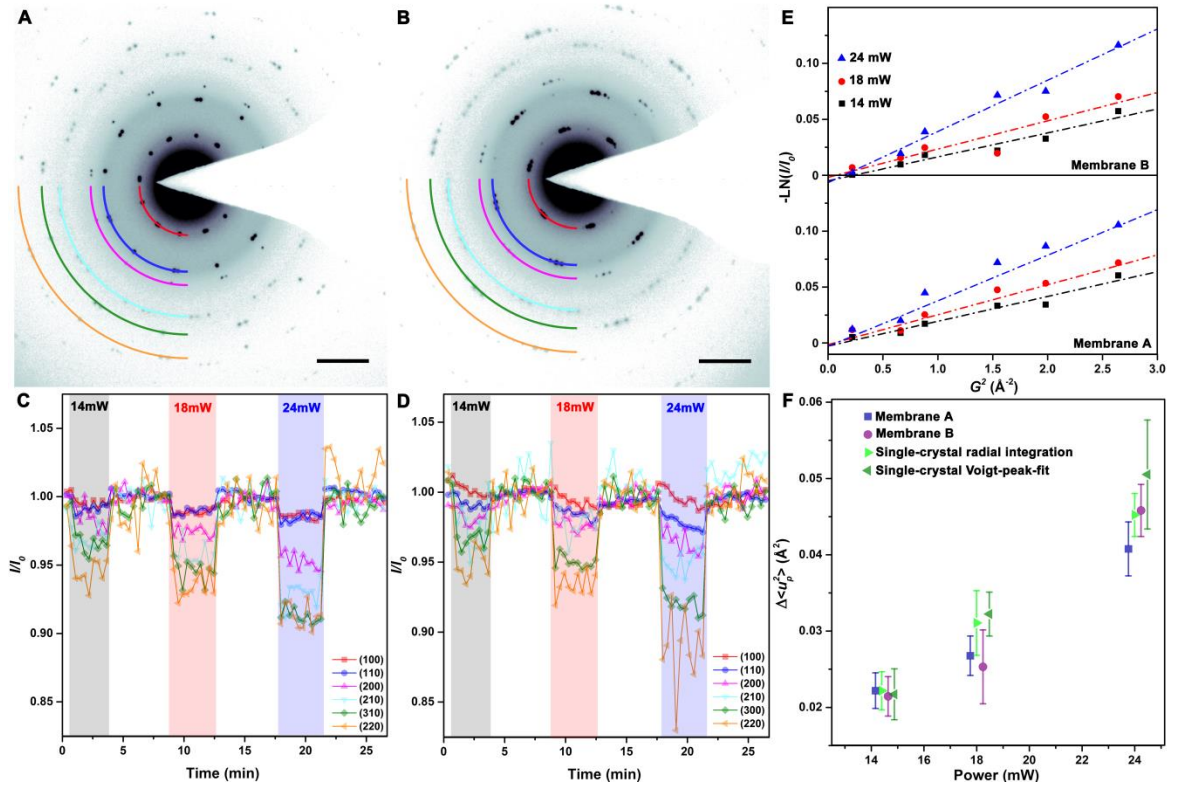
**Figure 3.5** Non-excited and laser-excited mean-squared displacements of polycrystalline membranes. (**A, B**) Selected-area diffraction pattern of the two analyzed polycrystalline graphene membranes (scale bar: 0.5 $\text{Å}^{-1}$) indexed by color arcs whose intensity are displayed in (C, D). (**C, D**) Intensities of diffraction spots out to sixth-order normalized to median laser-off values. The transparent colored boxes represent the an open shutter with 14 mW (black), 18 mW (red) and 24 mW (blue) of green laser power directed to the specimen. (**E**) Plots of $-\text{LN}(I/I_0)$ versus $G^2$ with dashed lines representing linear fits used to extract $\Delta{<}U^2{>}$ for the two membranes in (A) and (B) (**F**) Extracted values of $\Delta{<}U^2{>}$ for the two polycrystalline membranes as compared to the single-crystal membranes. Error bars for the polycrystalline data points represent normal error of slope from linear fitting of $-\text{LN}(I/I_0)$ vs. $G^2$. Error bars for the single-crystal data points represent the standard deviation of the extracted values for three different single-crystal membranes. The data is offset marginally on the x-axis for clarity.

### 3.2.4 | Atomic Vibrations within Individual Grains

Probing vibrational amplitudes with SAED offers the additional utility of examining grains individually – that is, elastic scattering from misoriented grains can be analyzed independently. Shown in Fig. 3.6 A, azimuthal integration over a fixed scattering vector magnitude isolates discrete peaks with intensity sensitive to atomic displacements only within that particular grain. However, minor sample drift upon laser excitation results in varying areas of illumination within the selected-area aperture region and thus intensity variations of peaks relative to one another. As such, extraction of the DWF for individual grains is modified such that each time-point is normalized by a low-

47

order diffraction spot, canceling the illumination dependency. The change in mean-squared displacements, $\Delta<U^2>$ is then given by Equation 3.5 below:

$$\Delta<U^2>=\frac{LN(\frac{I_j}{I_i})_{laser\ on}-LN(\frac{I_j}{I_i})_{laser\ off}}{G_j^2-G_i^2} \qquad (E3.5)$$

where $I$ is the intensity of an azimuthal peak at radii indicated by the subscripts $j$ and $i$, and $G$ is magnitude of the scattering vector at radii $i$ and $j$.
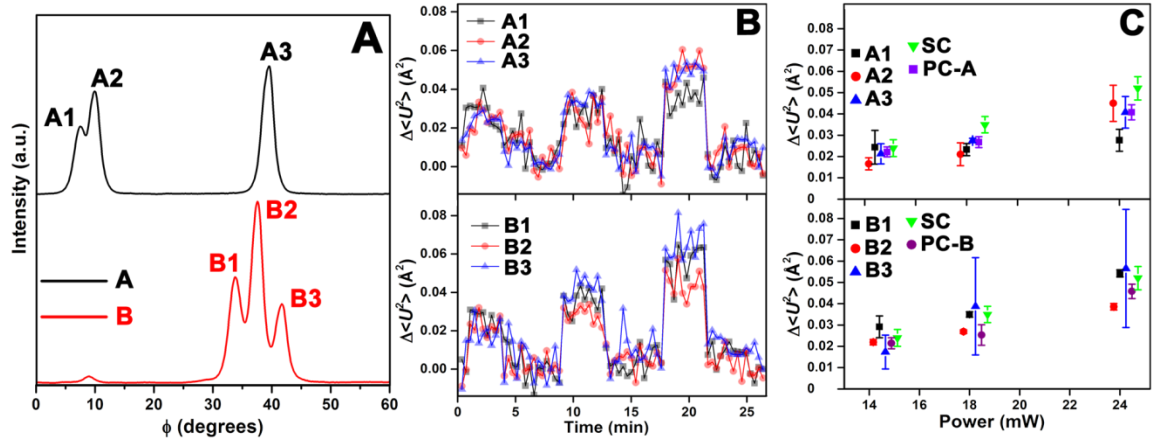


**Figure 3.6** Mean-squared displacements within individual grains. (**A**) Azimuthally integrated traces of the (110) reflection with labeled peaks corresponding to the individual grains analyzed. (**B**) Values of $\Delta<U^2>$ extracted for 3 grains in two polycrystalline membranes via application Eq. 5 and averaging calculations with $j = 5, 6$ and $i =1, 2$. (**C**) Extracted values of $\Delta<U^2>$ for the three grains in each polycrystalline membrane as compared to the single-crystal membranes (green) and the collectively analyzed polycrystalline membrane (purple square/circle). Error bars for the polycrystalline data points represent the standard deviation of 4 calculations of $\Delta<U^2>$ with $j = 5, 6$ and $i =1, 2$. Error bars for the single-crystal data points represent the standard deviation of the extracted values for three different single-crystal membranes.

48

Again, we test the analysis on single-crystal membranes and compare the measurements with three grains in each polycrystalline membrane. Displayed in Fig. 3.6C, we identify a grain in both membranes whose atomic displacement modulation varies significantly from other grains in the membrane and that of the single-crystal membranes; particularly at high-powers, it appears the increase in out-of-plane displacements is quenched in grains A1 and B2 as compared to the other grains. While it is unclear why this behavior arises for certain grains, the collective $\Delta<U^2>$ of the PC membranes, somewhat expectedly, lies near the average of the individual grains. We expect that further systematic experimentation with more precisely controlled grain morphologies and misorientation angles will be required to elucidate the observed dissimilarities.

## 3.3 | Outlook

The *in-situ* laser-heating experiments presented here offer a depiction of the vibrational behavior of the graphene membranes at pseudo-equilibrium conditions with temperatures dictated by heat-dissipation of the support structure. While the measurements indicate the magnitude of projected out-of-plane displacements at different excitation conditions, phonon kinetics within the membrane occur at time-scales well below those achievable under the present experimental conditions. However, access to non-equilibrium phenomena could be achieved via stroboscopic extension of the current techniques – that is, exploiting the SAED modality of fs- and ns- ultrafast electron microscopy (UEM). Indeed, the rippling dynamics of large-area single-crystal graphene

membranes have been investigated with this technique,[96] and the results showed – after an initial lattice expansion flattened the corrugations (~5 ps time-scale) – the onset of a long-lifetime amplitude enhancement of the intrinsic ripples. Similarly, flexural modes conforming to corrugated specimen morphology have been observed on these time-scales via fs-bright-field imaging.[43] We envision that phonon kinetics in polycrystalline graphene could be monitored by tracking the DWF associated with each individual grain as a function of time-delay. In this case, dynamical phonon population and relaxation in sub-lattices would be sensitive to scattering events at individual interfaces and mode confinement within grains of specific size and morphology. While the proposed experiments offer unique insight, a variety of practical challenges – largely pertaining to obtaining beam-current sufficient for adequate signal-to-noise – must be mitigated to render them feasible.[75]

## 3.4 | Summary

In conclusion, the two non-contact laser-heating "thermometry" techniques employed here provide auxiliary insight into thermal transport and vibrational modes in suspended graphene structures. The small exitation spot-size of the Raman "laser-flash" technique offers sensitivity to deviations in heat conduction arising as contributions to phonon-scattering from GBs dictate effective transport properties, and we observe a five-fold reduction in thermal conductivity upon reducing grain sizes from ~2.1 μm to ~ 400 nm. Atomic structural information afforded by *in-situ* SAED, on the other hand, unveils the large population of out-of-plane vibrations which persist for membranes of dissimilar grain size. The experimentally determined values of RMS displacements – nearly 0.47 Å

at room-temperature and increasing linearly from 0.61 to 0.69 Å upon laser excitation spanning 14 to 24 mW – suggest out-of-plane contributions dominate elastic-scattering supression and the commensurate DWF. While flexural phonon modes are known to dominate thermal transport in monolayer graphene, the extreme out-of-plane amplitudes observed (as compared to previous measurements of the DWF) motivate further systematic study into the thermomechanics of suspended 2D structures with varying levels of support.

Additionally, we have extracted vibrational dynamics of individual crystalline grains via analysis of their isolated diffraction spots, and we expect the experimental framework outlined here will aid in future quantitative measurements of properties local to grains just a few nanometers in size. Further, extension of the technique to the stroboscopic domain (i.e. ns or fs-UEM) would enable non-equilibrium depictions of phonon population and relaxation within individual grains and offer insight into interfacial confinement and scattering. The results reported here illustrate the utility of both correlative and *in-situ* electron diffraction techniques in investigating modes of thermal transport in nanostructured thin-film materials.

# 4 | *In Situ* and Ultrafast Structural Transitions in TaS$_2$: An Illustration of Operational Challenges in UEM

In this chapter, we discuss a variety of *in situ* and stroboscopic experiments performed on exfoliated flakes of TaS$_2$ with 1T- and 4H$_b$- polytypes. The material exhibits a superlattice of charge-ordering known as charge-density waves with structure highly-dependent on temperature, stacking-order, and doping level.[81, 82, 97] The complex phase equilibria and resulting physical phenomena occurring at different thermodynamic conditions represent open questions regarding structure-function relationships in the material and make it a promising candidate for study with non-equilibrium techniques such as UEM. However, the complexity of the charge-ordering phase-diagram with respect to temperature and stacking-order also magnify a variety of practical challenges associated with UEM experiments. For one, the elevated operating temperatures associated with employment of intense high-frequency (~10 kHz to 1 MHz) laser pulse-trains often lead to pseudo-steady-state conditions well outside of the range where charge-ordering occurs. Second, strong shear-waves resulting from laser-excitation can lead to irreversible changes in local polytype and thus preclude stroboscopic operation.[98]

Finally, time-scales[69, 99] for charge-order melting are on the order of the electron packet duration in UEM and care must be taken to deconvolute intrinsic time-scales for material response from instrument response. Here, we discuss observations in the context of applying appropriate experimental parameters in UEM operation.

## 4.1 | COMSOL Simulations of Rep. Rate Dependent Specimen Temperature

To illustrate and investigate the range of pseudo-steady-state operating temperatures in UEM, we have performed time-dependent finite-element simulations with the COMSOL Multiphysics heat-transfer module. Laser-excitation is simulated by employing a time-dependent volumetric heat-source which represents optical absorption of a laser-pulse with defined pulse energy (~0.1 μJ) within the specimen volume. We follow the specimen heating conditions (via continuum heat transfer with relevant conduction and radiation terms) over the microsecond to millisecond time-scales as the pulse-trains result in convergence to a pseudo-steady-state temperature. We have studied two common support structures in TEM experiments: a holey silicon nitride support film and a bulk crystal polished to a wedge.

Shown in Figure 4.1, the holey $Si_3N_4$ and Ge wedge take ~0.1 ms and ~0.2 ms, respectively, to relax back to room-temperature after a single-pulse, and thus any repetition rate above 5 kHz ($Si_3N_4$) and 10 kHz (Ge) results in elevated operating temperatures. Indeed, we can see that over the course of a millisecond temperatures can exceed 1000 K for both specimens at repetitions rates greater than 200 kHz and exceed 400K for the $Si_3N_4$ support even at 50 kHz. Despite minimal optical absorption, the

silicon nitride film suffers from poor thermal conductivity and insufficient thermal flux to a surrounding heat sink. As such, this support structure is far from an ideal UEM specimen if we seek to operate at elevated rep. rates often required for sufficient beam current.
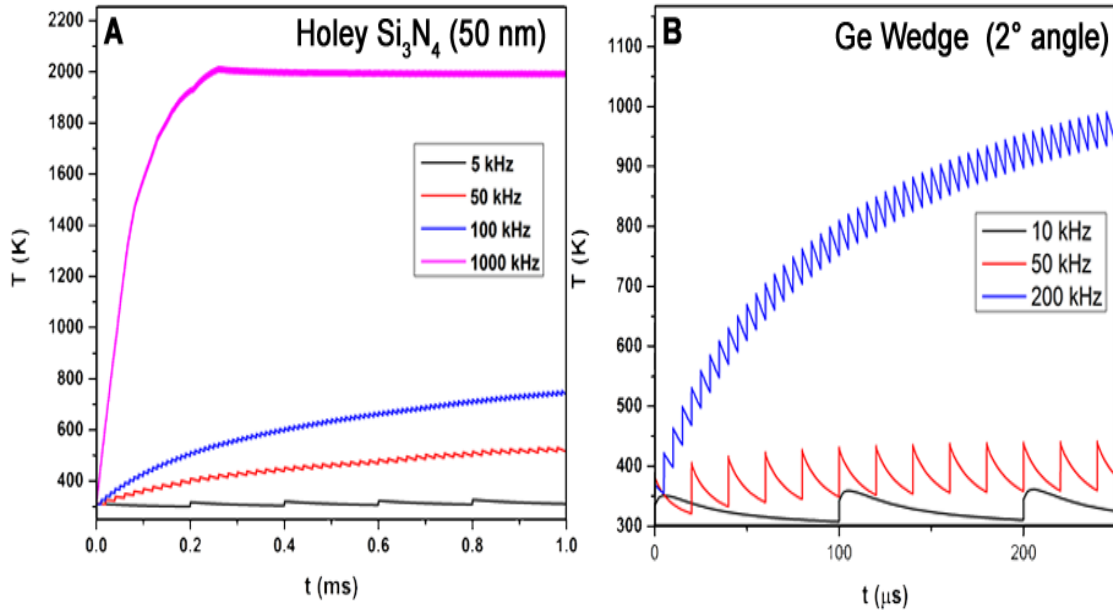


**Figure 4.1** Elevated pseudo-steady-state operating temperatures of UEM specimens. (A) Heat-transfer dynamics of a holey silicon nitride support film (B) Heat-transfer dynamics of a polished Ge wedge

For the Ge wedge, we also investigated the dependencies of operating temperature on the spatial position of the pump on the specimen and with respect to various regions of interest. Figure 4.2 shows the heat-transfer dynamics of regions of interest at the center of a pump beam located in three spots on the edge of the wedge. While we see marginal changes in temperature due to the tilted contact with support slot grid (i.e. the heat sink is further away from corner 1 than corner 2), the effect of moving the pump beam to a thicker portion of the wedge results in much greater temperature disparities. In Figure

4.3, we show the temperature at corner 1 with the pump beam centered at the corner and with it moved forward and backward 100 μm. With the pump beam centered in a thicker region of the wedge, we not only see a ~300 K increase in operating temperature at 200 kHz but a delay in the onset of dynamics resulting from heat propagation to the region of interest. These conditions are not ideal for UEM and illustrate the importance of pump-beam alignment on the specimen. Moving the pump beam towards the vacuum region 100 μm, however, effectively reduces the fluence and thus decreases both the magnitude of the individual temperature jumps and baseline operating temperature. Fig. 4.3B illustrates various laser conditions comparing the pump beam centered at the edge and towards the vacuum; the results suggest intentionally placing a portion of the beam over the vacuum region could result in decreased operating temperatures at much higher rep. rates (blue trace) or heightened pulse energies (red trace). Nonetheless, we can discern that the heat-transfer conditions of the specimen are of critical importance in practical execution of delicate UEM experiments.
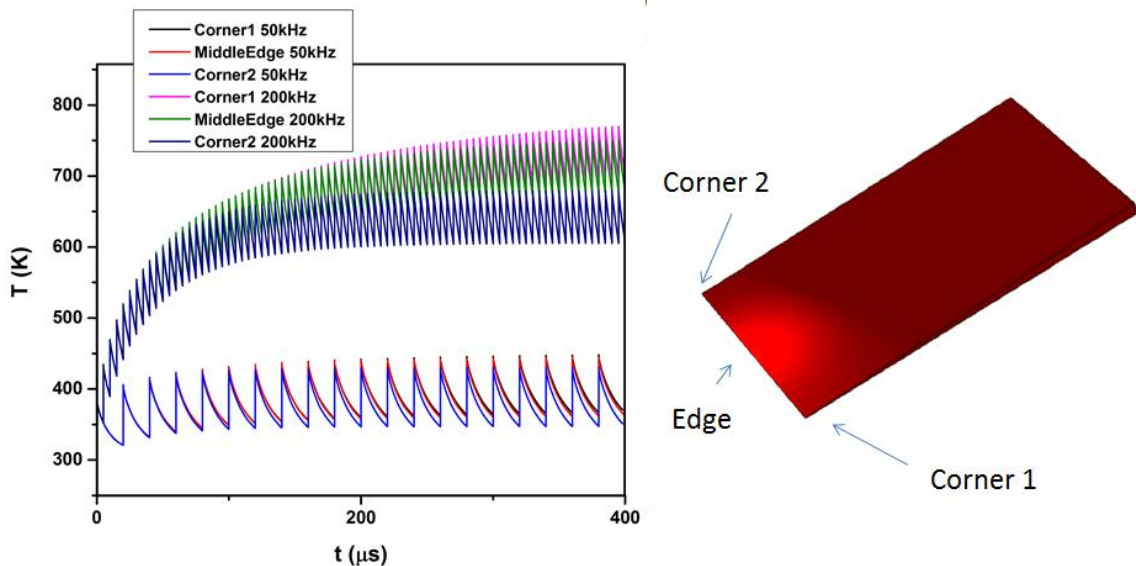
**Figure 4.2** Temperature dependence on the spatial position of the pump beam on the edge of the wedge. Temperatures of probed within the center of the beam
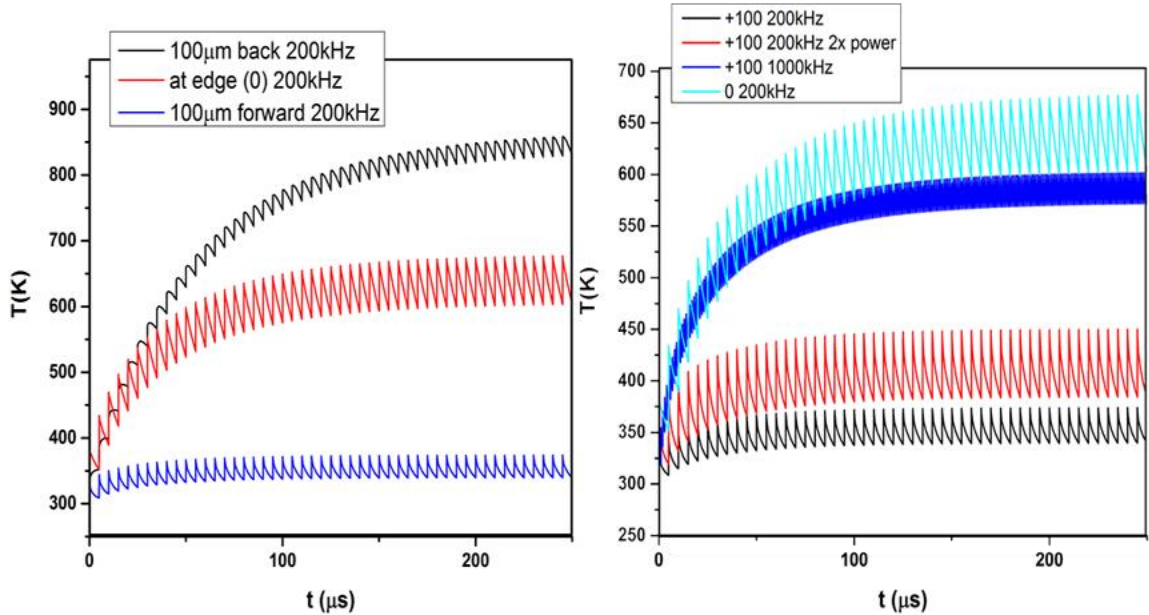


**Figure 4.3** Temperature dependence on the spatial position of the pump beam with respect to the edge of the wedge. Temperatures of probed at the corner of the wedge for all pump positions. (A) Moving the pump beam from the vacuum region to the corner of the wedge, and to a thicker portion of the wedge results in a large increase in operating temperature due to increase volumetric absorption in thicker regions. (B) Delocalizing the pump beam toward the vacuum region could potentially decrease the operating temperatures for similar pump conditions (black), increased individual temperature jumps (red), or higher rep. rates (blue) with respect to a pump beam centered on the corner of the specimen (light blue).

## 4.2 | *In Situ* Structural Phase Transitions in TaS2

4.2.1 | Laser-heating $4H_B$- and $1T$-$TaS_2$ Flakes

While numerous open questions remain regarding the role of atomic structure and structural perturbations (i.e. dislocations, phonons, etc.) on correlated electronic phenomena in $TaS_2$,[70, 100, 101] the complex phase equilibria make $TaS_2$ a delicate specimen-of-interest in UEM. As discussed the previous section, pin-pointed the operating temperature (and the consequent ground-state thermodynamic equilibria) can be a non-trivial task. To determine suitable repetition rates for studying phase transitions − that is, finding operating conditions such that the ground state lies in a specific portion of the phase diagram and laser-excitation drives a transition to a new phase − we have performed *in situ* electron diffraction in thermionic mode (i.e. temporal resolution on the millisecond to second time-scales) with laser excitation at variable repetition rates. Figure 4.4 shows the results of laser excitation at rep. rates between 1 and 13.3 kHz for two different $TaS_2$ flakes. Both flakes are exfoliated thin-flakes (~50 nm thick) with lateral dimensions of ~2 μm supported by a 50nm thick holey $Si_3N_4$ support. It is immediately apparent that the flakes show different charge-ordering structures which result from different polytypes. Although the as-acquired flakes (HQ Graphene, Inc.) were nominally 1T type (as determined by XRD) the different flakes appear to show $4H_B$ behavior (top) as well as 1T behavior (bottom). While it is unclear whether this transition occurs during the exfoliation process, it is likely that some flakes undergo a transition after intense laser-excitation − that is, they are quenched to a new phase after intense heating and subsequent rapid cooling occurs upon turning off the laser. Nonetheless, we can compare the behavior of the $4H_B$- and 1T- polytypes.

For the laser-heating studies we switch back and forth between illumination at 1 kHz and illumination at a specified higher rep. rate to both observe phase transitions and determine their reversibility. Figure 4.4 shows the electron diffraction patterns at different rep. rates for the $4H_B$- and 1T-flakes and the intensity of a selected radius as a function of azimuthal angle; the transparent red regions represent the laser-on at higher rep. rates.   For the $4H_B$-flakes we observe a suppression of the intensity of the satellite spots (corresponding to the $13a_0$ superlattice) just above 5 kHz. Interestingly, as the intensities of these spots fade, we see an additional diffuse spot appear in between the two spots. In each case, the previous phase can be restored by lowering the rep. rate to 1 kHz. It is likely that this behavior corresponds to a transition from a nearly-commensurate phase with two superimposed, rotated domains (the α- and β-rotated $\sqrt{13}a_0$ superlattices)[82] to an incommensurate phase observed in $1T\text{-}TaS_2$ also. This transition likely occurs near 315 K as resistivity traces indicate a $1^{st}$-order transition near this temperature.

Seen in the bottom of Figure 4.4, we examine the behavior of the $1T\text{-}TaS_2$ of the $\sqrt{13}a_0$ diffraction spots. In this case, we see only marginal fading until the spots disappear completely at 10 kHz (they are reversible, though the laser off behavior is not shown here). Notably, $13a_0$ spots are not visible at any rep. rate; it is unclear whether this is because they are too faint to achieve good signal-to-noise or that symmetry isn't satisfied in this particular flake. Nonetheless, the transition observed likely corresponds to the well-studied nearly-commensurate to incommensurate transition that occurs around 350 K.
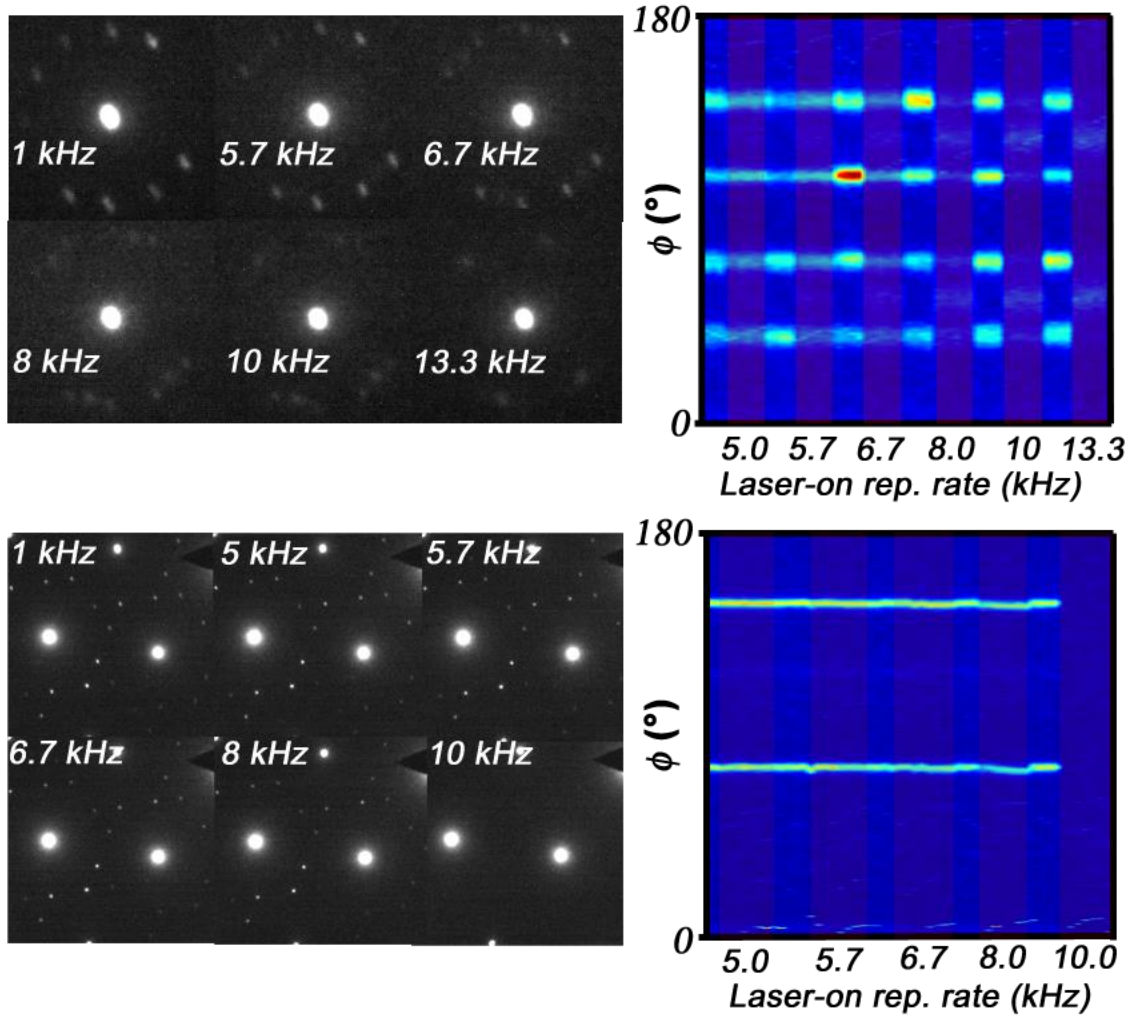
**Figure 4.4** TaS$_2$ Phase Transitions Driven by Laser-heating at Varying Rep. Rates. (Left) Electron diffraction acquired with laser-excitation at the specified rep. rates for the 4H$_B$- (top) and 1T- (bottom) polytypes. (Right) Azimuthally integrated rings for the 13a$_0$ superlattice in 4H$_B$-flakes (top) and $\sqrt{13}$a$_0$ superlattice in 1T-flakes (bottom). The transparent red regions indicate an increase in rep. rate to that specified on the x-axis.

The relatively low rep. rates in which these transitions occur would make UEM study of these materials quite difficult owing to the simultaneous requirements of low pseudo-steady-state temperatures (below 315 K for the 4H$_B$- and 350 K for the 1T-TaS$_2$)

and sufficient beam-current to discern faint superlattice spots. The results of this study and the suggestions from the COMSOL simulations indicate that the silicon nitride support structures are far from ideal and a specimen with better heat-transfer properties will likely be required for stroboscopic studies of $TaS_2$.

4.2.2 | Temperature dependence of $4H_B$-transition via electron diffraction with cryo-holder

It is important to note that the specific rep. rates where transitions occur are unique to individual flakes as each flake has different heat-transfer conditions. It would be convenient to have an idea of which temperatures (rather than rep. rates) these transitions occur. For this purpose we have obtained electron diffraction at temperatures between 90 K and 375 K with a liquid nitrogen holder equipped with a resistive heating element.  Shown in Figure 4.5, we acquire electron diffraction patterns at temperatures ranging from 90 K to 375 K on a $4H_B$-$TaS_2$ flake. The trace shows a gradual increase in the intensity of the $13a_0$ reflections from 90 K to ~225 K at which point we observe a distinct maxima. Upon a sharp decrease in the intensities of these spots, an increase in intensity is observed for the intermediate spot corresponding to the incommensurate phase. Just above 325 K we see a sharp decrease in the intensity of all superlattice spots. These results indicate that the $4H_B$-flakes gradually transition from nearly-commensurate behavior to incommensurate behavior between 275 K and 325 K and become fully incommensurate above this temperature. Additionally, the results confirm that the behavior observed in the laser-heating studies is indeed the result of steady-state temperature effects rather than some optical phenomena. Indeed the observed transition

temperatures represent an upper limit to pseudo-steady-state operating temperatures suitable for performing stroboscopic studies of particular phase transitions.
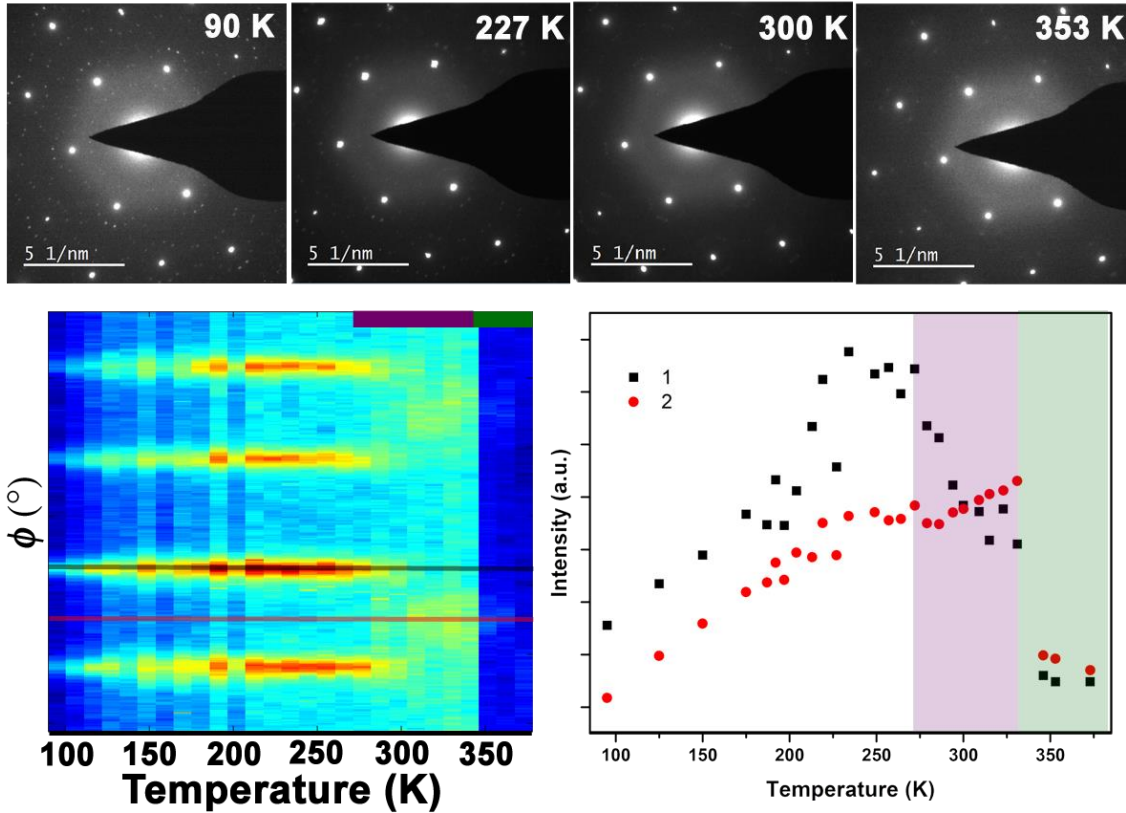


**Figure 4.5** Temperature-dependent electron diffraction elucidates $4H_B$-phase-transitions. (Top) Electron diffraction from a $4H_B$-$TaS_2$ flake at selected temperatures. (Bottom left) Azimuthally integrated rings for the $13a_0$ superlattice as a function of temperature. The purple and green blocks indicate the regions in which we observe a gradual transition from nearly-commensurate to incommensurate followed by a sharp transition to fully incommensurate. (Bottom right) Intensity traces taken from the angles specified by the colored lines in the azimuthal traces.

## 4.3 | Single-pulse Switching of Satellite-spot Orientation

Thus far we have discussed phenomena resulting from temperature rises on the millisecond time-scale dictated by specimen heat dissipation. Indeed these results, though at pseudo-steady-states, represent equilibrium phenomena. We have additionally observed metastable transitions arising from excitation with single laser pulses. This peculiar phenomena was first discerned when laser-on diffraction showed additional satellite spots not present in laser-off diffraction. Shown in Figure 4.6, diffraction patterns acquired with the laser-off (A) and laser-on at 1 kHz (B) show distinct features. First, the spots present in both patterns are much fainter. Second, a set of spots with identical symmetry, though rotated, appear upon laser excitation. Upon pulse-picking down to 1 Hz, we observed switching behavior of the orientation of the nearly-commensurate triangles present in diffraction. A composite diffraction pattern generated via subtraction of the pre-laser-pulse from the post-pulse diffraction (Fig. 4.6 C) illustrates this phenomena, and, as seen in Fig. 4.6 D & E the pre- and post- triangles are rotated by ~28 degrees. It is likely that this orientation flipping corresponds to transitions between the α- and β-rotated $\sqrt{13}a_0$ superlattices.[82]

While the mechanism of this transition is unclear, some type of dislocation motion and pinning is a likely source. Interestingly, we note that the coexistence of the α- and β-rotated $\sqrt{13}a_0$ superlattices form the basis of the superstructure of the $4H_B$-polytype. It is known that the interpolytypic transition between 1T- and $4H_B$- occurs via a shear mechanism in which layers in between partial dislocations glide to form different stacking structures.[102] We hypothesize that a shear wave generated by laser excitation alters the dislocation structures within the lattice and flips the domain after motion is

pinned. The resulting lattice indeed must have two metastable equilibrium structures and relaxes to one of the two after each shear motion.
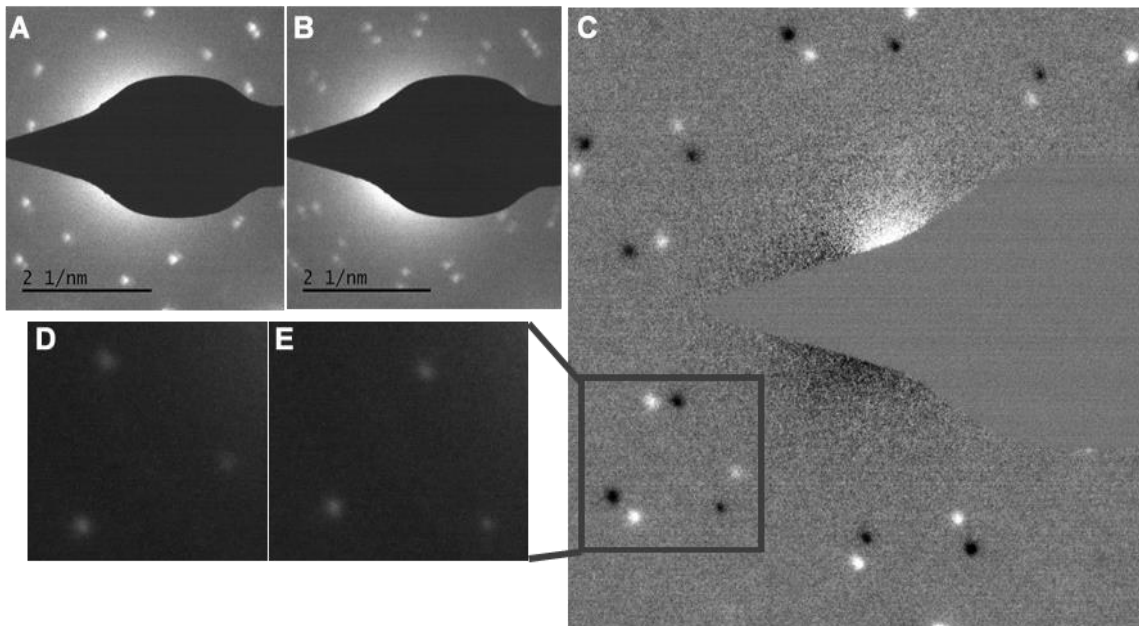


**Figure 4.6** Superstructure Domain Flipping Via Single-Pulse Optical Excitation. (A) Electron diffraction of a 1T-TaS$_2$ flake acquired with the laser-off (B) Electron diffraction of a 1T-TaS$_2$ flake acquired with the laser-on at 1 kHz showing additionally diffraction spots. (C) Composite diffraction pattern generated via subtraction of the pre-laser-pulse from the post-pulse diffraction (D, E) Rotated superstructure triangles after a single laser-pulse

The metastability on display here is another challenge in performing UEM experiments as the non-equilibrium behavior must be reversible. The peculiar switching behavior here indeed resulted in equal population of two metastable states at 1 kHz repetition rate implying the domain was continuously flipping between the states during the acquisition period. Many variants of this behavior can occur in UEM experiments. For instance, if a mechanical resonance rings longer than the appropriate relaxation time

dictated by the rep. rate, diffraction or real-space images can be acquired over a range of effective Bragg angles; thus, the resulting patterns are an average over every state present during the many pulses required for acquisition. Similarly, a structural transition which does not relax to its original state in the appropriate time (i.e. $1/f$) will contain various artifacts of aliasing. Executing proper controls for correct interpretation of dynamics is of critical importance.

## 4.4 | Ultrafast Melting of Charge-order in Real-space and Diffraction-space

To facilitate studies of the ultrafast melting of charge-order in a $1T$-$TaS_2$ flake, we prepared a sample supported by a 2000-mesh copper grid. Heat-dissipation is aided in this support structure by the 18 μm thick copper grid bars sitting in a 6 μm square lattice; thus we can operate at increased rep. rates (while maintaining low operating temperatures) and higher beam currents sufficient for achieving good signal-to-noise for the faint superlattice spots. Additionally, the flakes are suspended over an area nearly 7 times as large as the $Si_3N_4$ holes, and elastic scattering from the larger region also increases signal-to-noise for the CDW reflections.

Shown in Figure 4.7, we observe charge-order melting of the nearly-commensurate phase in $1T$-$TaS_2$ on the few-ps time-scale. We acquire electron diffraction patterns at time-delays ranging from -25 ps to 100 ps in random order as a control measure to ensure dynamics are indeed from ultrafast melting. The intensity of a spot indicated in Figure 4.7A by the square is plotted as function of time delay and fitted

to an inverted and scaled error function such that we extract an idea of the temporal

response of the melting. The observed time constant for the process is 6.6 ps.
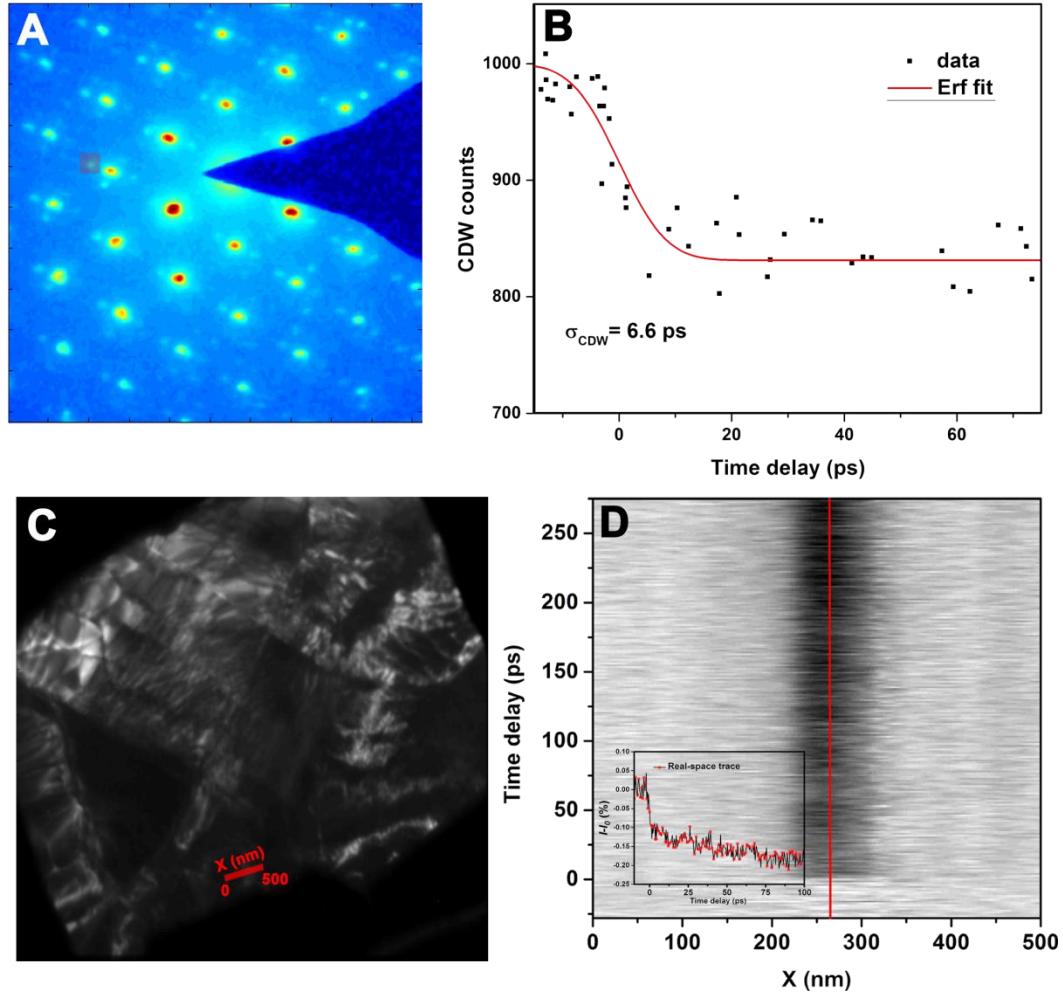


**Figure 4.7** Ultrafast electron diffraction and imaging of charge-order melting in 1T-TaS$_2$.

(A) Photoelectron diffraction pattern for the TaS$_2$ flake shown in the DF-image in (C).

(B) Ultrafast kinetics of a nearly commensurate superlattice reflection (A, sqaure)

intensity. We extract a time constant of 6.6 ps. (C) Representative dark-field image from

a ultrafast temporal scan. Analysis was performed on the region indicated by the red line

as particularly swift dynamics were observed here. (D) Space-time contour plot for the

region indicated by the red-line in (C). We believe the fast intensity suppression is a real-space manifestation of the charge-order melting observed in diffraction.

Notably, this scan was acquired with particularly high electron packet population to achieve sufficient signal-to-noise. Under these conditions, we might expect a broadening on the temporal envelope of the electron packet and effectively convolute the intrinsic material response.[30] Indeed, previous studies have seen a range of time constants for the melting process (~0.5 ps to ~5 ps),[69, 99] though each experiment has its own instrument response and indeed material responses of the many phases and morphologies of charge-ordering are likely to vary significantly. More than anything, the diffraction kinetics observed in this experiment illustrate the critical need for systematic determination of the instrument response function in UEM (we will discuss our efforts and approaches to this process in chapters 5 & 6).

We also acquired a temporal scan of dark-field images on this flake. In this case, we placed the objective aperture over a group of superlattice reflections to form the time-resolved dark-field images such as those shown in Figure 4.7C. Notably, each image was acquired over 50 seconds with a CCD binning of 4 to achieve maximum counts (binning increases effective counts by $2^n$ though reducing the sampling frequency). Shown in Figure 4.7 C & D, we have identified a region which shows modulation of contrast (in this case intensity suppression of a small contour) features on timescales similar to those extracted from the electron diffraction experiment. While a more rigorous analysis would be require to verify or indeed form an interpretation, we believe this provides enough evidence to conclude that ultrafast studies of these phase transitions could be resolved

with nm spatial resolution. However, clearly this is a delicate experiment, and optimization of electron collection and stability as well employment of a more sensitive CCD will likely be required to perform systematic experiments.

## 4.5 | Summary

In this chapter, we have outlined a variety of practical challenges in UEM which are well exhibited by experimentation on thin flakes of $TaS_2$. COMSOL simulations showed elevated operating temperatures for different support structures illuminated by a laser at rep. rates ranging from 5 kHz to a MHz. For the different $TaS_2$ flakes, this resulted in pseudo-state-operating temperatures surpassing phase transition temperatures even at modest fluences and rep. rates below 10 kHz. The temperature dependence was revealed via electron diffraction patterns acquired in a liquid nitrogen cryo-TEM specimen holder and showed that this transition indeed occurs near room temperature for the $4H_B$-polytype. Additionally, a single-pulse switching effect was observed in which the orientation of charge-order rotated by ~28° after excitation with a single laser-pulse and could be reversed with an additional pulse. This type of irreversible or semi-irreversible process complicates stroboscopic UEM studies, either hindering their interpretation or making them altogether impossible. Finally, we illustrated diffraction and dark-field image kinetics of superlattice spots on the ultrafast time-scale. Though a time constant of 6.6 ps was observed, the electron packet duration in UEM and commensurate instrument response were unknown, and intrinsic time-scales for material response must be deconvoluted from instrument response for proper interpretation. While

a plethora of challenges exist, some local real-space information was extracted and we believe direct observations of charge-order dynamics on their native spatiotemporal length-scale can indeed be achieved.

# 5 | Consequences of Spatiotemporal Overlap of Intense Laser-fields and Ultrashort Electron Packets

In ultrafast electron microscopy (UEM) experiments, the initial excitation period is comprised of spatiotemporal overlap of the pump photon pulse and probe photoelectron packet. Generation of evanescent near-fields at the nanostructure specimens produces a dispersion relation that enables coupling of the photons ($\hbar\omega$ = 2.4 eV, for example) and freely-propagating electrons (200 keV, for example) in the near-field. Typically, this manifests as discrete peaks occurring at integer multiples ($n$) of the photon energy in the low-loss region of electron-energy spectra (*i.e.*, at 200 keV $\pm$ $n\hbar\omega$ eV). In the weak-interaction regime (i.e., relatively low pump-laser fluence), the time-dependent cross-section of the zero-loss peak (ZLP) is precisely the convolution of the electron and photon temporal profiles. While this increased electron-energy dispersion holds additional imaging resolution implications from additional chromatic aberration during temporal overlap, the time-dependent behavior of electron-photon coupling acts as a sensitve indicator of electron packet properties (i.e. temporal envelope width, space-charge chirp, velocity-space correlations, etc.).

In this chapter, we describe a technique for *in situ* characterization of ultrashort

electron packets that makes use of coupling with photons in the evanescent near-field of the specimen. We show that within the weakly-interacting (i.e., low laser fluence) regime, the zero-loss peak temporal cross-section is precisely the convolution of electron packet and photon pulse profiles. Beyond this regime, we outline the effects of non-linear processes and show that temporal cross-sections of high-order peaks explicitly reveal the electron packet profile, while use of the zero-loss peak becomes increasingly unreliable.

Additionally, we examine the UEM imaging resolution implications of the strong inelastic near-field interactions between the photons employed in optical excitation and the probe photoelectrons. We find that the additional photo-induced energy dispersion occurring when swift electrons pass through intense evanescent near-fields results in a discrete chromatic aberration that limits the spatial resolving power to several angstroms during the excitation period.

## 5.1 | Instrument Response via Time-dependent Coupling of Electrons and Photons

The variable time delay dictated by the position of the stage allows one to temporally scan (in this case) the photon pump pulse across the electron probe packet, each with a fixed spatial position (i.e., at the specimen location). One consequence of illumination of the specimen with the photon pump pulse is light scattering and near-field enhancement, the intensity and spatial arrangement of which depend upon the material properties and feature shape.[103, 104, 105] When spatiotemporally overlapped at the specimen, the freely-propagating electrons (with energy $E$, e.g., 200 keV and comprising

70

the ZLP) in the probe packet can absorb photons (with energy $\hbar\omega$, e.g., 2.4 eV, where $\hbar$ is the reduced Planck constant and $\omega$ the angular frequency of light) in the pump pulse and transition into discrete excited states ($E + n\hbar\omega$, where $n$ is an integer). This process, known as the photon-induced near-field effect (PINEM), is described experimentally and theoretically in detail elsewhere.[106, 107, 108, 109] In UEM, evidence for electron-photon coupling is experimentally observed in the low-loss region of the electron-energy spectrum. Precise spatiotemporal overlap at the specimen produces discrete peaks occurring at integer multiples of photon quanta to both the loss ($-n\hbar\omega$) and what corresponds to the gain ($+n\hbar\omega$) side of the ZLP.[106, 110]

In PINEM, electrons in the probe packet gain quanta of energy only in the presence of the photon pump pulse (and only when both are spatially overlapped at the specimen). The intensity response (i.e., electron counts) of the ZLP in the energy spectrum is therefore directly related to the cross-correlation of the photon (pump) pulses and electron (probe) packets. This is because the lifetimes of the plasmonic effects that lead to generation of the evanescent near-field are much shorter than the photon pulse durations typically employed in UEM. That is, the temporal envelope of the near-field directly follows the photon pulse. As such, and akin to optical auto-correlation, this interaction can in theory be used to sample and characterize the temporal envelope of the electron packets by varying the (temporal) overlap (at a fixed spatial position) of the pump and probe and measuring the associated intensity response of the ZLP.[38, 111, 112] Because interaction between the freely-propagating electrons and the photons can occur

only in the near-field of the specimen, appropriate deconvolution allows for electron packet characterization precisely at the specimen location.

5.1.1 Energy Spectra and the Instrument Response Function

Determining the relation of the observed temporal behavior of low-loss energy spectra to the true photoelectron packet properties requires examination of the intensity dependence of PINEM transitions. Considering a first-order transition probability that is linearly proportional to the evanescent field intensity, $Q_1(t) = \alpha I_p(t)$, the probability density of the electron packet that has gained one photon of energy is given by Equation 5.1.

$$P_1(t; \tau) = Q_1(t)P_e(t + \tau) = \alpha I_p(t)P_e(t + \tau) \qquad (E5.1)$$

Here, $P_e(t)$ is the probability density of the electron packet, $I_p(t)$ is the intensity profile of the pump laser pulse, and $\tau$ is the time delay. Integration over the entire electron packet then yields a first-order population (E5.2).

$$P_1(\tau) = \int_{-\infty}^{\infty} \alpha I_p(t)P_e(t + \tau)dt = \alpha\{I_p \otimes P_e\}(\tau) \qquad (E5.2)$$

In Equation 5.2, $\otimes$ signifies cross-correlation. Thus, for electron-photon coupling in the linear regime, the temporal dependence of both the first-order peak and the ZLP, $P_0(\tau) = 1 - 2P_1(\tau)$, is proportional to the cross-correlation of the electron packet and photon pulse, which is by definition the UEM IRF.

At laser fluences typically employed in UEM experiments, electrons can absorb multiple photons, and as a result, population of $n^{th}$-order states (where $n > 1$) also contributes to depletion of the ZLP. Nevertheless, theoretical examination of the PINEM effect indicates that the linear approximation is indeed valid in the weak-interaction limit.

72

That is, it is valid when the Bessel function of the first kind describing the intensity dependence of the PINEM transition probabilities can be approximated to the first term in the Taylor series shown in Equation 5.3.[107]

$$Q_n = \left| J_n\{\beta I_p(t)^{1/2}\} \right|^2 \approx \frac{\beta^{2n}}{2^n n!} I_p(t)^n \quad \text{for} \quad \beta I_p(t)^{1/2} \ll \sqrt{n+1} \qquad \text{(E5.3)}$$

In Equation 5.3, $\beta$ is a proportionality constant, and $J_n$ is an $n^{\text{th}}$-order Bessel function of the first kind. The effects on the energy distribution when in the weak-interaction limit are illustrated in Figure 5.1, where varying overlap produces a significant depletion of the ZLP around zero time delay. The resulting temporal cross-section [Fig. 5.1(c)] takes on an inverted Gaussian shape with a total FWHM of $\boldsymbol{\Delta_0} \approx \sqrt{\boldsymbol{\Delta_e^2 + \Delta_p^2}}$, which is a convolution of the electron packet and photon pulse durations. Furthermore, in the weak-interaction limit, the Gaussian temporal widths of $n^{\text{th}}$-order peaks [side-bands in Fig. 5.1(a,b)] are $\boldsymbol{\Delta_n} \approx \sqrt{\boldsymbol{\Delta_e^2 + \frac{\Delta_p^2}{n}}}$, where $\sigma$ is the standard deviation and $\Delta = 2[2\ln(2)]^{0.5} \cdot \sigma$.
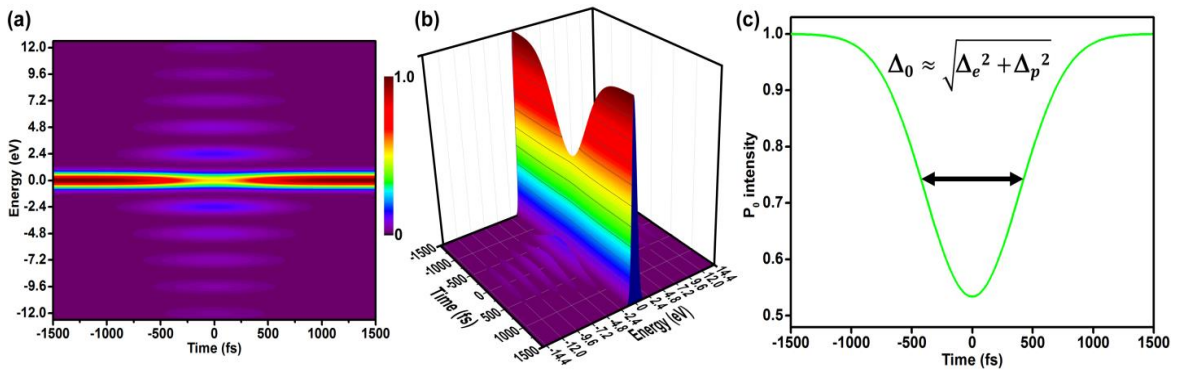


**Figure 5.1** Pulse characterization via the photon-induced near-field effect. (a,b) Calculated time/energy phase space plots. Narrowing of the temporal widths for higher order peaks is evident in (a), while depletion of the ZLP around zero time delay can be

seen in (b). (c) Temporal cross-section of the ZLP. In the weak-interaction limit, the temporal dependence of the zero energy-loss cross-section ($\Delta_o$) is the convolution of the electron packet ($\Delta_e$) and photon pulse ($\Delta_p$) temporal profiles.

Notably, $n^{th}$-order states are populated within an effective optical pulse length range of $\frac{\sigma_p}{\sqrt{n}}$; $n^{th}$-order transitions are probable only for delays in which there is sufficient overlap for $n$ transition events to occur. As also observed in the recently-reported laser-streaking approach,[113] higher orders show decreasing temporal widths, as the threshold intensity is an exceedingly small portion of the laser pulse. In principle, any of the higher-order peaks ($n > 1$) could be separated by using the effective optical pulse duration to obtain the temporal profile of the electron packet, though the ZLP is typically chosen due to its relatively large signal.

5.1.2 | Effects of Increasing Interaction Strength

In the weak-interaction limit, linear depletion of the ZLP results in a temporal signal that is precisely the convolution of the incident electron packet and photon pulse profiles. Higher-order peaks are populated in a similar manner, though the probabilities are low, and the time window for these transitions becomes increasingly narrow. In this weak-interaction regime, direct determination of electron packet properties from low-loss energy spectra is not hampered by inherent artifacts introduced by non-linear effects. For increasing interaction strengths, however, broadening of the temporal widths and deviation from Gaussian behavior have been observed.[107] These artifacts are the direct result of non-linear effects that occur at the increased fluences often employed in UEM experiments. In general, electron-photon coupling behavior is dependent on both the

intensity of the pump laser pulse and the optical properties of the specimen, which gives rise to the evanescent near-field. The interaction parameter ($\Omega$), defined as the argument of the Bessel function in Equation 5.3, encompasses these dependencies for arbitrary fluences and specimens.

For a focused electron beam, the oscillatory nature of the fluence dependence results in alternating depletion and population of peaks for different interaction strengths, as illustrated in Figure 5.2(a). For example, in the weak-interaction limit, only one PINEM event is likely to occur, meaning that the vast majority of electrons depleted from the ZLP populate the first-order peaks. As the interaction strength increases, the likelihood of two transition events becomes dominant, and the first-order peak is depleted in favor of the second-order and zero-loss peaks. Further increase in interaction strength yields higher probabilities for a greater number of transition events. This non-linear interaction gives rise to temporal signals that deviate from Gaussian shape in regions of maximum electron-photon coupling. Shown in Figure 5.2(c), the observed temporal behavior of the first-order peak diverges from the cross-correlation of the electron packet and photon pulse to a non-Gaussian temporal profile with increasing interaction parameter (e.g., $\Omega = 2$ to 18). This is due to depletion of the first-order states for delays in which a greater number of transition events are likely to occur.
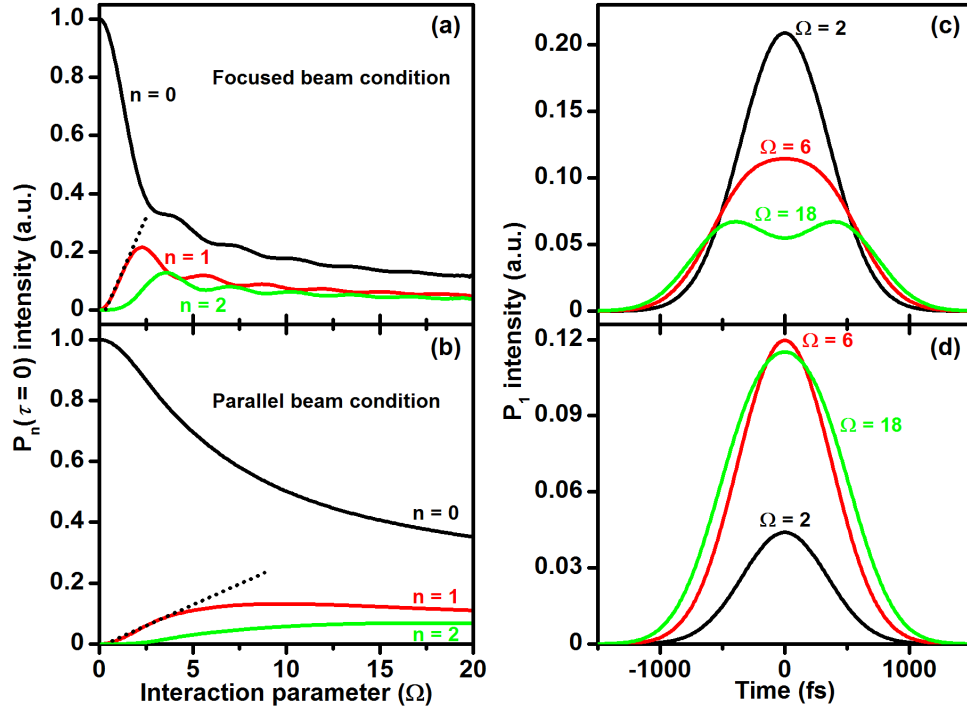
**Figure 5.2** Fluence dependence of the PINEM effect. (a,b) Intensities of low-order PINEM peaks at maximum pulse overlap versus interaction strength ($\Omega \propto I_0^{1/2}$) for (a) focused and (b) parallel electron beams. The oscillatory nature of the fluence dependence is evident in (a) but is absent in (b) due to spatial integration. The dashed lines guide the eye to linearity in the weak-interaction limit. (c,d) First-order peak temporal cross-sections. For a focused beam (c) the first-order peak is depleted near maximum pulse overlap resulting in non-Gaussian cross-sections. For a parallel beam (d), this effect is less pronounced but becomes significant at higher fluences.

In practice, pulse characterization should take place under parallel-beam (electron) illumination, where resulting low-loss energy spectra are the summation of interactions over the entire beam cross-section. Because the Fourier component of the electric field parallel to electron propagation decays exponentially with distance from the

nanostructure, the oscillatory nature of the interaction-parameter dependence is effectively averaged out [Fig. 5.2(b)]; effectively-linear coupling occurs over a greater range of interaction parameters [depicted by the dashed line in Figure 5.2(b)]. Note, however, that low-order peaks can still exhibit appreciable deviation from Gaussian shape under parallel beam illumination at high fluence due to depletion within the next effective optical pulse range [Fig. 5.2(d)]. This is a multistate analogue to the Rabi oscillation in a two-level system. Artifacts of the non-linear PINEM process generally appear as a broadened temporal signal in experimental plots and thus do not accurately portray the intrinsic pulse properties. For electron packets with durations comparable to the pump laser pulse, broadening of the ZLP signal by up to 30% is expected to occur for applicable fluences (see Appendix C). Ideally, characterization of pulse properties would take place in the weak-interaction limit where low-loss energy behavior explicitly identifies temporal properties of incident pulses. Operating in the weak-interaction limit, however, produces lower counts and is therefore more susceptible to noise.

5.1.3 | Circumventing Fluence-dependent Artifacts

One approach for determining electron packet durations in arbitrary interaction regimes is to utilize weak-interaction behavior of high-order peaks. Because these peaks experience narrowing effective-optical-pulse durations and show weak-interaction behavior at higher fluences, temporal peak widths for increasing $n$ converge to the electron packet duration $\left(\text{i.e., } \lim_{n \to \infty} \sqrt{\sigma_e^2 + \frac{\sigma_p^2}{n}} = \sigma_e \right)$. Thus, temporal cross-sections of high-order PINEM side bands are expected to reflect the intrinsic properties of the

electron packets; accurate electron packet properties can be efficiently extracted from these features.

In practice, the limit discussed above can be obtained from linear-regression analysis – plotting $\sigma_n^2$ obtained from experiments versus $n^{-1}$ and determining the y-intercept as $\sigma_e^2$. Figure 5.3 shows such an analysis for $\sigma_n^2$ versus $n^{-1}$ for several interaction strengths ($\Omega$). A variety of information can be extracted from such a plot, including – and perhaps most importantly – accurate determination of the electron packet duration regardless of the fluence. Linearity of the data gives an estimation of the interaction strength and thus the accuracy of time-dependent ZLP plots in relation to the actual UEM IRF. Increased curvature indicates higher interaction strengths; however, a linear regime always remains for small $n^{-1}$ within the weak-interaction limit.

The slopes of the best-fit lines in Figure 5.3 provide an *in situ* estimation of the photon pulse duration for comparison with (currently) external auto-correlation measurements. Table 5.1 compares the photon pulse and electron packet durations obtained by linear-regression analysis with the theoretically-observed temporal width of the ZLP. Although the observed peak widths of the ZLP broaden due to non-linear effects at high interaction strengths, electron packet properties predicted from linear regression remain accurate. Thus, this analysis effectively suppresses broadening effects in observed data giving a more accurate depiction of pulse properties and the UEM IRF.
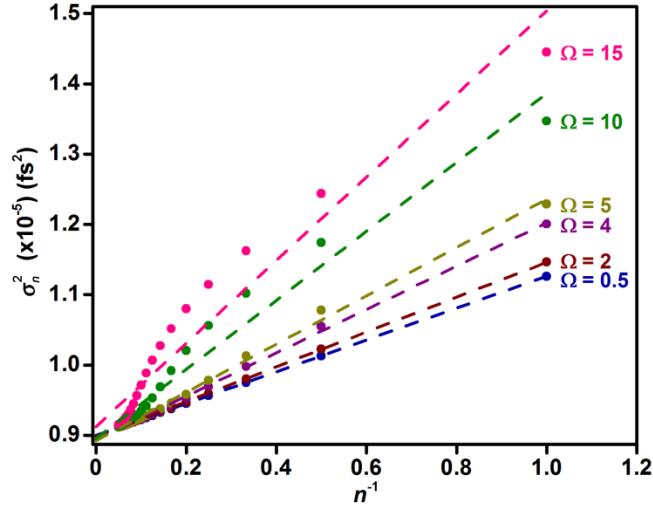
**Figure 5.3** Electron packet properties in select interaction regimes. Shown is the square of the calculated temporal widths of PINEM side bands ($\sigma_n$) plotted versus $n^{-1}$. The dashed lines are linear best fits to the calculated points and are labeled with the corresponding interaction strength ($\Omega$), which increases from 0.5 to 15.

**Table 5.1** Temporal pulse properties $(\sigma_x)^a$ as a function of interaction strength ($\Omega$) determined from linear regression analysis of the numerical simulation[b].

| $\Omega$ | $\sigma_p^{\,c}$ (fs) | $\sigma_e^{\,c}$ (fs) | $\sigma_0^{\,d}$ (fs) |
|---|---|---|---|
| 0.5 | $150 \pm 1$ | $300.0 \pm 0.5$ | $335.563 \pm 0.001$ |
| 2 | $157 \pm 4$ | $300 \pm 2$ | $337.74 \pm 0.02$ |
| 4 | $176 \pm 8$ | $299 \pm 4$ | $343.18 \pm 0.07$ |
| 5 | $185 \pm 11$ | $299 \pm 6$ | $345.0 \pm 0.1$ |
| 10 | $222 \pm 23$ | $299 \pm 12$ | $356.7 \pm 0.2$ |
| 15 | $243 \pm 30$ | $302 \pm 16$ | $364.4 \pm 0.3$ |

[a]$x = p$, $e$, or 0, where $p$ = photon pulse, $e$ = electron pulse, and 0 = convoluted pulses

[b]Simulated using temporal widths of $\sigma_p = 150$ fs and $\sigma_e = 300$ fs (see the methods section in the Appendix C)

[c]Obtained from linear regression (see Section 5.1.3).

[d]Obtained from fitting the ZLP cross-section. Note the width of the convolution is

$$\sigma_0 = \sqrt{\sigma_p^2 + \sigma_e^2} = 335.41 \text{ fs.}$$

## 5.2 | Discrete Chromatic Aberrations Arising from the PINEM Effect in UEM

In UEM, the narrow electron-energy distribution afforded by populating each packet with, on average, one photoelectron[36] can be compromised by the effects discussed in the previous sections. Inelastic interaction of swift photoelectrons with intense, photo-generated transient evanescent near-fields results in significant population of discrete energies separated from the initial state by integer multiples of the pump-photon energy.[106, 114, 115] In this section, we show that the induced electron-energy envelope arising from absorption and emission of photons in the excited-specimen near-field becomes the dominant effect with respect to the spatial resolution of UEM during the initial excitation period. Moreover, we show that certain spatial frequencies become exaggerated due to the non-linear nature of the near-field interaction.[39, 107] By applying a filter comprised of discrete, transient chromatic aberrations resulting from near-field interactions to representative lattice-fringe images of ordered nanostructures, we demonstrate that the time-dependent point spread function produces significant blurring,

the transient nature of which directly tracks the pump-pulse/probe-packet cross correlation.

5.2.1 | Point-spread Functions of Electron Packets with Quantized Energy

In order to quantify the effects described above on UEM image formation, the point spread function (*PSF*) of the objective lens is determined using spherical- and chromatic-aberration coefficients ($C_s$ and $C_c$, respectively) and operating parameters typical of a 200-kV TEM equipped with a $LaB_6$ thermionic gun (see Chapter 2). The *PSF* for a particular imaging system describes its response to a point source and thus enables visualization of the effects of particular aberrations on the images.[8] Figure 5.4 summarizes the results of convoluting the UEM discrete chromatic dispersion with a conventional *PSF*. Owing to the velocity dependence of the Lorentz force, an energy distribution such as the one shown in Figure 5.4(b) will produce a radially-symmetric projection in the Gaussian image plane consisting of concentric rings of varying intensity (ignoring conventional aberrations for the moment) [Fig. 5.4(c)]. Thus, the *PSF* describing the time-delay-dependent chromatic aberration, $PSF_c(\tau, r)$, can be represented by spatial analogues to the energy-distribution parameters $\Delta E$ and $\hbar\omega$ (E5.4 to E5.6). Here, $\tau$ is the delay time between the pump pulse and the probe packet, $r$ is the position in the image plane, and $\Delta E$ is the electron-energy distribution, which is governed by the photoemission process at the electron gun (in the case of negligible space-charge effects).

$$\delta_{\Delta E} = C_c \frac{\Delta E}{V} \beta \qquad \text{(E5.4)}$$

$$\delta_{\hbar\omega} = C_c \frac{\hbar\omega}{V} \beta \qquad \text{(E5.5)}$$

$$PSF_c(\tau,\ r) = \sum_n P(\tau,\ n\hbar\omega)\exp\left[\frac{-(r-n\delta_{\hbar\omega})^2}{2\delta_{\Delta E}{}^2}\right] \qquad (E5.6)$$

The width and separation between the concentric rings shown in Figure 5.4(c) are described by $\delta_{\Delta E}$ and $\delta_{\hbar\omega}$, respectively (E5.4 and E5.5, respectively), where $\beta$ is the collection angle and $V$ is the accelerating voltage. The amplitude of each ring is governed by the energy envelope describing the population of discrete states, $P(\tau, E)$ [Fig. 5.4(b), dotted red line]. Note that, as with the side-band peak amplitudes in energy space, the intensities of the rings comprising $PSF_c$ are spatially dependent owing to the variance of the non-dimensional interaction parameter ($\Omega$) at different points within the near-field (see Appendix D).[107] For a homogenous section of the near-field, however, $\Omega$ is assumed to slowly vary over the few angstroms in which the $PSF$ is non-zero. Evaluating populations at a fixed $\Omega$ then becomes a reasonable approximation.
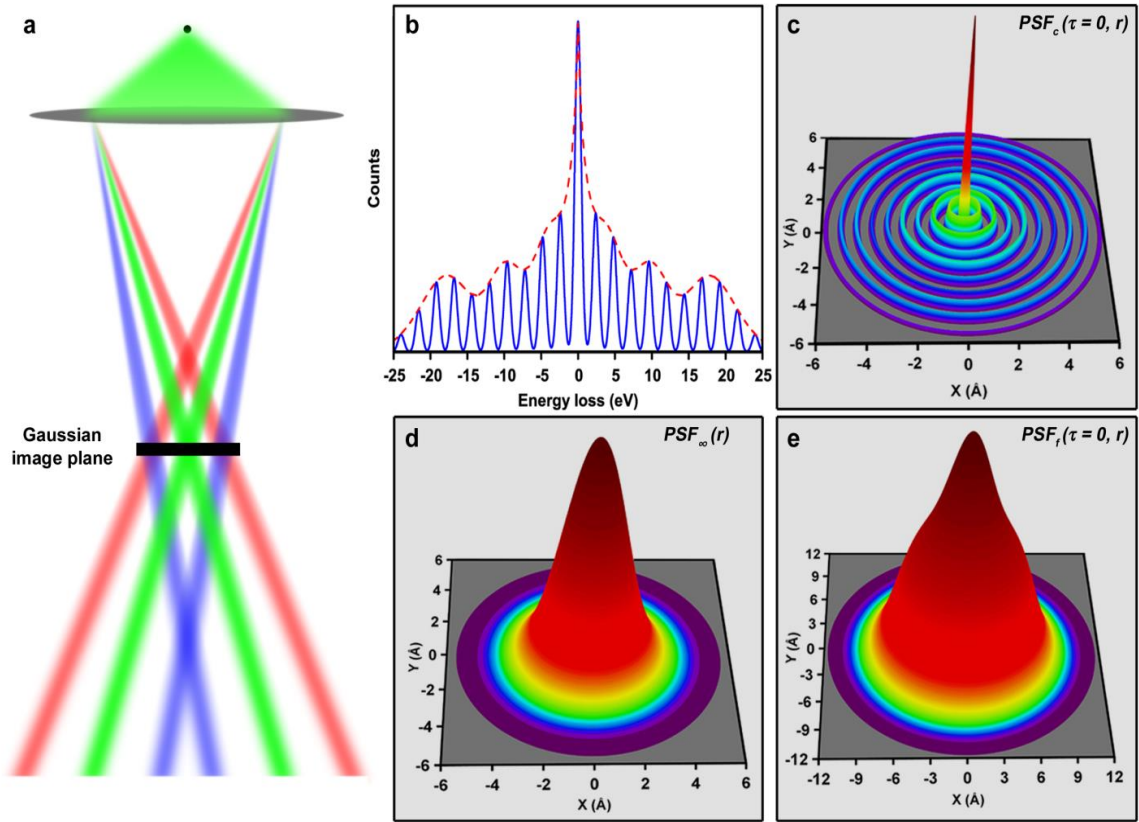
**Figure 5.4** Effects of discrete chromatic dispersion on a conventional point spread function (*PSF*). (a) Conical ray diagram depicting the spread of electrons having a discrete energy distribution on the Gaussian image plane. The green rays correspond to zero-loss (*i.e.*, $E_0 = 200$ keV) electrons, while the red and blue are those that have gained and lost one photon quanta of energy, respectively. The spread in each of the colored rays is meant to qualitatively represent the inherent energy distribution arising from the photoemission process (*e.g.*, 1 eV, absent significant space-charge broadening). (b) Non-linear envelope (dashed red line) of a typical UEM photon-induced near-field electron-energy distribution arising from a moderate interaction parameter, $\Omega$. The *x*-axis corresponds to energy loss relative to $E_0$; negative values indicate energy gains with respect to $E_0$. (c) Annular chromatic point spread function (*PSF$_c$*) at $\tau = 0$ plotted as a

83

function of $r = x,y$ Å. (d) Static *PSF* as $\tau \to \infty$ [*i.e.*, temporally far from electron-photon overlap, $PSF_\infty(r)$] encompassing the instrument spatial-resolution limit. (e) Convolution of $PSF_\infty(r)$ and $PSF_c(\tau = 0, r)$ to produce a final *PSF* [$PSF_f(\tau = 0, r)$] illustrating the effects of the UEM discrete chromatic dispersion at $\tau = 0$. Note the factor of two increase in the range of the *x* and *y* axes relative to that in (d).

To examine the regime in which near-field induced chromatic effects are prevalent, an additional Gaussian *PSF* [$PSF_\infty(r)$], which encompasses the inherent instrument-resolution limit (*i.e.*, far from temporal overlap), is introduced. For $PSF_\infty(r)$, the radius of the disk in the image plane ($r_{min}$) is fixed at 1.5 Å. Convolution of $PSF_\infty(r)$ and $PSF_c(r)$ returns the final time-delay-dependent UEM *PSF* [$PSF_f(r)$], as described by Equations 5.7 through 5.9 and shown in Figure 5.4(e).

$$\delta_{min} = \frac{2r_{min}}{2\sqrt{2\ln(2)}} \qquad \text{(E5.7)}$$

$$PSF_\infty(r) = \exp\left[\frac{-(r)^2}{2\delta_{min}{}^2}\right] \qquad \text{(E5.8)}$$

$$PSF_f(\tau, r) = (PSF_\infty * PSF_c)(\tau, r) = \int PSF_\infty(\rho)PSF_c(\tau, r - \rho)d\rho \qquad \text{(E5.9)}$$

At maximum temporal overlap (*i.e.*, $\tau = 0$), a broad shoulder is observed in $PSF_f(r)$ that corresponds to the energy envelope resulting from the photon-induced near-field effect [Fig. 5.4(e)]. Note also that the area of the *xy*-plane has expanded by a factor of four. Absent energy-filtering capabilities, $PSF_c(r)$ and, thus, $PSF_f(r)$ will significantly impact UEM image quality during the initial excitation period, as discussed below. It is worth noting that the value of $r_{min}$ does not necessarily correspond to the same focus conditions considered in the calculations of $PSF_c(r)$; the overall plane of least confusion does not

generally occur in the Gaussian image plane but rather at the Scherzer defocus. Indeed, these calculations represent a best-case scenario for chromatic aberrations, as minor focus deviations from the image plane will result in increased radii of the concentric rings that comprise $PSF_c(r)$.

### 5.2.2 | Transfer Functions of Electron Packets and Their Time-dependence

Quantifying spatial resolution can also be performed in Fourier space where non-vanishing intensity at spatial frequencies furthest from zero correspond to the smallest resolvable features in the real-space images. In reciprocal space, transfer functions that represent the imaging-system response are multiplicatively applied to the intensity spectrum of the object (E5.10 and E5.11).[8]

$$I_{observed}(\tau, r) = (I_{object} * PSF_f)(\tau, r) = \int I_{object}(\rho)PSF_f(\tau, r - \rho)d\rho \quad \text{(E5.10)}$$

$$\hat{I}_{observed}(\tau, s) = \int I_{observed}(\tau, r)exp(2\pi irs)dr = \hat{I}_{object}\hat{H}_\infty\hat{H}_c(\tau, s) \quad \text{(E5.11)}$$

Here, $I_{observed}$ and $\hat{I}_{observed}$ are the image intensity in real and reciprocal space, respectively; $I_{object}$ and $\hat{I}_{object}$ are the object intensity in real and reciprocal space, respectively; $\hat{H}_c$ and $\hat{H}_\infty$ are the Fourier transforms of $PSF_c$ and $PSF_\infty$, respectively; and $s$ is the spatial frequency. For any arbitrary object $[I_{object}(r)]$, features in the intensity spectrum $[\hat{I}_{object}(s)]$ are modulated by the envelope resulting from the product of the transfer functions upon formation of the observed image and intensity spectrum $[I_{observed}(\tau, r)$ and $\hat{I}_{observed}(\tau, s)$, respectively]. Thus, resolution limits set by separate phenomena can be evaluated by examining the behavior of the appropriate transfer function.

Figure 5.5 summarizes the effects of convolving $\widehat{H}_c$ with $\widehat{H}_\infty$ and illustrates the behavior as a function of time delay. As can be seen in Figure 5.5(a), $\widehat{H}_c$ exhibits distinct maxima at spatial-frequency values of $\pm n/\delta_{h\omega}$, with amplitude dictated by the width of the zero-loss peak. When this is convolved with $\widehat{H}_\infty$, spatial frequencies falling between those that share intensity with $\widehat{H}_c$ are significantly depleted. A one-dimensional cross-section of $\widehat{H}_c$ [Fig. 5.5(c), solid blue; from red horizontal line in Fig. 5.5(a)] resembles the Fourier transform of the population envelope $\widehat{P}$ near the distinct maxima. This indicates that the energy envelope governs the behavior of $\widehat{H}_c$ at relevant spatial frequencies (*i.e.*, those frequencies falling within non-vanishing values of $\widehat{H}_\infty$). Indeed, Figure 5.5(b) shows distinct depletion at frequencies within the envelope of $\widehat{H}_\infty$, confirming that spatial resolution near time-zero is limited by the increased chromatic dispersion.
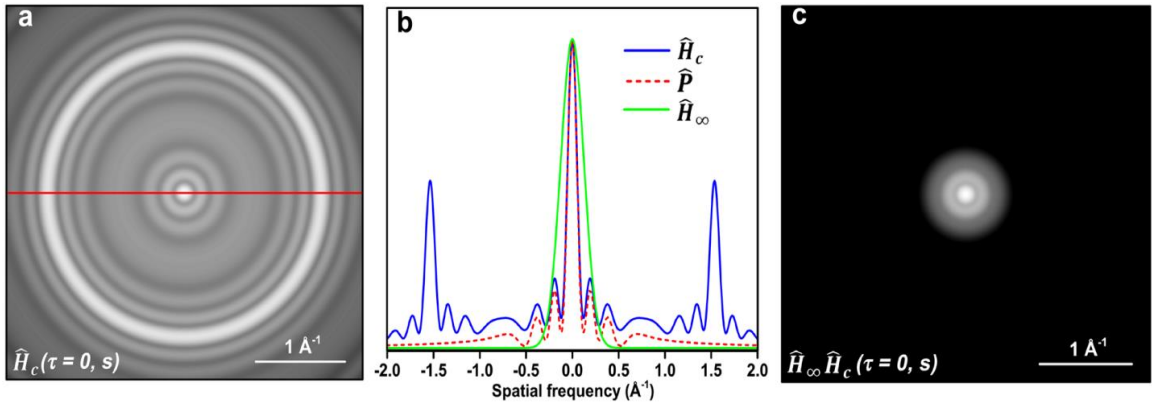


**Figure 5.5** Transient chromatic transfer functions. (a) Two-dimensional transient chromatic transfer function at $\tau = 0$ [$\widehat{H}_c(\tau = 0, s)$]. Here, $s$ = spatial frequency and $\tau$ = time delay. The horizontal red line marks the position from which the cross-section in

panel (b) was extracted (solid blue). The scale bar corresponds to 1 Å$^{-1}$. (b) Plot of the behavior of the normalized intensity dependence of $\hat{H}_c$ [solid blue curve; extracted from (a)] as a function of spatial frequency, as dictated by the particular inverse energy envelope ($\hat{P}$, dashed red curve) around the distinct maxima occurring at $\pm n/\delta_{\hbar\omega}$. The $\tau \rightarrow \infty$ transfer-function envelope ($\hat{H}_\infty$, solid green curve) is included to illustrate that multiple $\hat{P}$ sidebands fall within the $\hat{H}_\infty$ envelope. (c) Overall transfer function resulting from convolution of the transient component at $\tau = 0$ with that inherent to the system (*i.e.*, far from temporal overlap, $\tau \rightarrow \infty$) [$\hat{H}_\infty \hat{H}_c(\tau = 0, s)$]. Inclusion of $\hat{H}_c$ produces depletion of discrete intensities within the $\tau \rightarrow \infty$ transfer-function envelope. The scale bar corresponds to 1 Å$^{-1}$.

Plotting the cross-section of $\hat{H}_c$ for time delays where pulse overlap occurs [Fig. 5.6(a)] illustrates the temporal behavior of the effect; $\hat{H}_c$ is observed to gradually shift from its static form with width $1/\delta_{\Delta E}$ to its transient form with shape dictated by $\hat{P}$ approaching zero time delay. Because photoinduced chromatic effects are entirely dependent on spatiotemporal overlap of the pump laser pulse and photoelectron packet, significant intensity depletion occurs over timescales roughly corresponding to the quadrature of their temporal durations (full-width half-maximum, FWHM; $\sqrt{\Delta_e^2 + \Delta_p^2}$, where $\Delta_e$ = duration of electron packet and $\Delta_p$ = duration of photon pulse). Thus, for properties typical of fs UEM (*e.g.*, $\Delta_p \cong 100$ to 1,000 fs and $\Delta_e \cong 500$ to 1,500 fs), chromatic blurring will appear for 100s to ~1,000 fs around the initial excitation period (depending upon the precise durations). As depicted in Fig. 5.6(c), contours of the temporal duration of intensity depletion ($\Delta_t$, FWHM) at fixed spatial frequency and

fluence confirm this behavior follows for the majority of applicable fs UEM parameters. Deviations from linear coupling (where $\Delta_t \cong \sqrt{\Delta_e^2 + \Delta_p^2}$; see Appendix D) can be attributed to the increased portion of the optical pulse – with intense fields and associated with a condensed time envelope – capable of inducing several absorption and emission events.[39] Note that typical experimental cases, in which $\Delta_e > \Delta_p$, have been highlighted here. For the inverse case (*i.e.*, $\Delta_e < \Delta_p$), a condensed photoelectron packet samples only strong coupling regions of the optical pulse leading to highly non-linear population envelopes.[115] Accordingly, the chromatic transfer function exhibits an increase in the quantity and intensity of side-bands around the main peak. Nevertheless, these calculations suggest the transient chromatic aberration will be present for a large fraction of the sub-picosecond regime.
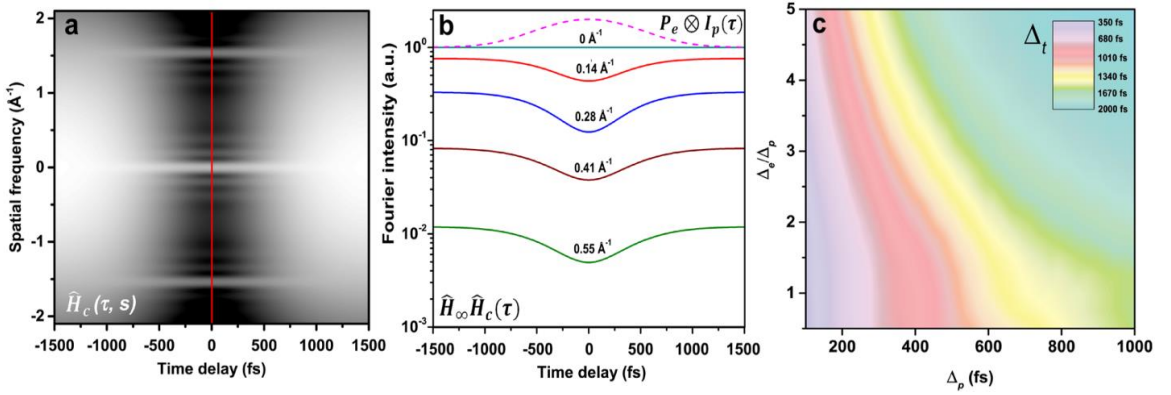


**Figure 5.6.** Temporal dependence of frequency depletions. (a) Variation of $\widehat{H}_c$ as a function of spatial frequency and time delay. The transient chromatic transfer function evolves from a Gaussian shape with width $1/\delta_{\Delta E}$ to non-monotonic behavior around $\tau = 0$. (b) Time traces of $\widehat{H}_\infty \widehat{H}_c(\tau)$ at select spatial frequencies (labeled above each curve in Å$^{-1}$). The cross-correlation of the electron packet and the pump-laser pulse temporal

profiles [$P_e \otimes I_p(\tau)$; dotted pink line] is shown for reference. (c) Contour plot of the FWHM of $\hat{H}_\infty \hat{H}_c(\tau)$ at $s = 0.28$ Å$^{-1}$ with $\Omega = 10$ for relevant electron-packet and laser-pulse parameters. Linear coupling occurs in the upper regime (*i.e.*, $\frac{\Delta_e}{\Delta_p} > 2.5$), and $\Delta_t \cong \sqrt{\Delta_e^2 + \Delta_p^2}$. As $\frac{\Delta_e}{\Delta_p}$ decreases, however, an inflection point is observed, which is indicative of non-linear coupling and results in $\Delta_t > \sqrt{\Delta_e^2 + \Delta_p^2}$.

We can extend the transfer-function approach to determine the amount of chromatic blurring that is expected to occur, and thus the effect on overall spatial resolution, as a function of photoinduced near-field strength. Figure 5.7(a) portrays the reciprocal envelope $\hat{P}$ for appropriate values of the interaction parameter $\Omega$ at maximum pulse overlap. For increasing strength, the width of the main peak becomes exceedingly narrow, limiting the resolvable spatial frequencies. It is clear that even for modest interaction parameters, the envelope width is on the order of the width of $\hat{H}_\infty$ [Fig. 5.7(a), green dashed line], indicating that a large spatial-resolution regime is impacted. The extent of this impact is also dependent on the pulse overlap occurring at different time-delays. Consequently, the effective resolution ($r_{eff}$) at each time point is estimated by adding in quadrature the reciprocal widths of the main peak of $\hat{P}$ ($\Delta_{\hat{P}}$, FWHM) and $\hat{H}_\infty$ such that $r_{eff} = \frac{1}{2}\sqrt{(2r_{min})^2 + 1/(\Delta_{\hat{P}})^2}$. The temporally varying resolution for various interaction parameters is poorest at zero time-delay, with minimum resolvable features limited to several Å for stronger fields [Fig. 5.7(b)]. Note also that the resolution does not recover until hundreds of fs after $\tau = 0$. Despite maintaining sub-nanometer

resolution, these results suggest sub-picosecond UEM imaging of few-angstrom lattice fringes may require phase retrieval with a known chromatic-dispersion filter.
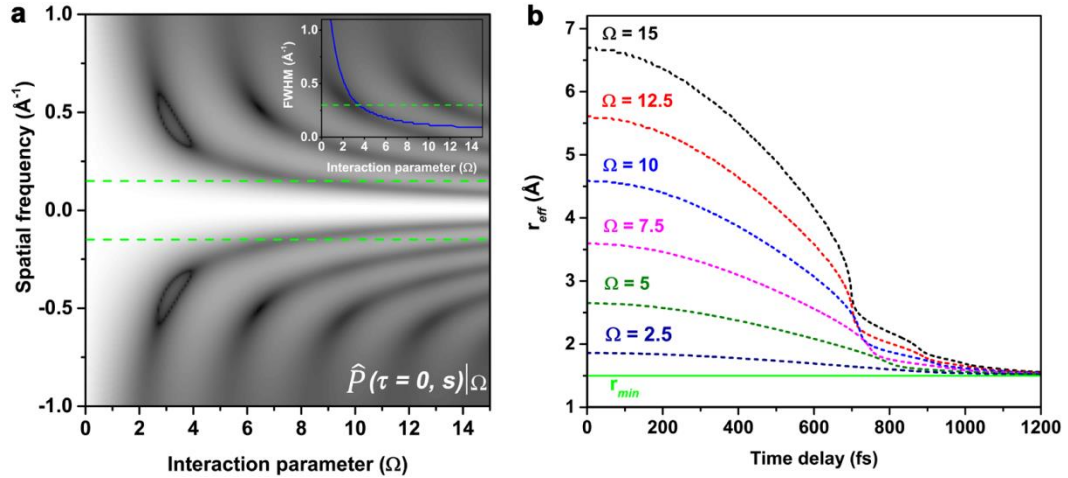


**Figure 5.7** Image resolution for varying interaction parameters (*i.e.*, near-field strengths). (a) Evolution of the inverse energy envelope (spatial frequency) as a function of interaction parameter. Widths of $\hat{P}(\tau = 0)$ rapidly become narrower than the envelope width of the static lens transfer function (inset; dashed green) with increasing interaction parameter, indicating the transient chromatic dispersion governs spatial resolution. (b) Temporal evolution of the effective resolution $r_{eff}(\tau)$ for varying interaction parameters (representative values labeled above each curve). For modest near-field strengths, the effective resolution is limited to several angstroms near $\tau = 0$ and endures for a majority of the sub-picosecond temporal regime until converging towards the static resolution ($r_{min}$, green line at $r_{eff} = 1.5$ Å).

5.2.3 | Application of Transfer Functions with Photoinduced Chromatic Dispersion to Example Images

To visually illustrate the effect of photoinduced chromatic dispersion on spatial resolution, $PSF_c(\tau = 0)$ was applied to experimental TEM images (Fig. 5.8). Lattice-fringe images of Au nanocrystals and a few-walled carbon nanotube were acquired in conventional TEM mode to represent the static resolution limit (*i.e.*, images containing $\widehat{H}_\infty$). The chromatic filter $\widehat{H}_c$ was applied in post-processing to exemplify the effect of laser-pulse/electron-packet overlap for a given time-delay and near-field strength. Figure 5.8 compares the images and FFTs of the nanostructures both far from ($\tau = \pm\infty$) and at maximum overlap ($\tau = 0$). The $\tau = \pm\infty$ image of Au nanocrystals [Fig. 5.8(a)] shows distinct fringes corresponding to the (111) planes ($d = 2.3$ Å). Because this planar spacing falls well outside the main envelope of $\widehat{H}_c$, these fringes are almost entirely unresolved in the resulting $\tau = 0$ image [Fig. 5.8(b)]. For larger spacings, such as the (002) graphitic planes of a few-walled carbon nanotube [$d = 3.4$ Å; Fig. 5.8(c)], distinct blurring is still observed in the $\tau = 0$ image [Fig. 5.8(d)], but because this feature falls within the secondary envelope, or side-peak of $\widehat{H}_c$ [see Fig. 5.8(d) inset], these planes are still faintly discernible.
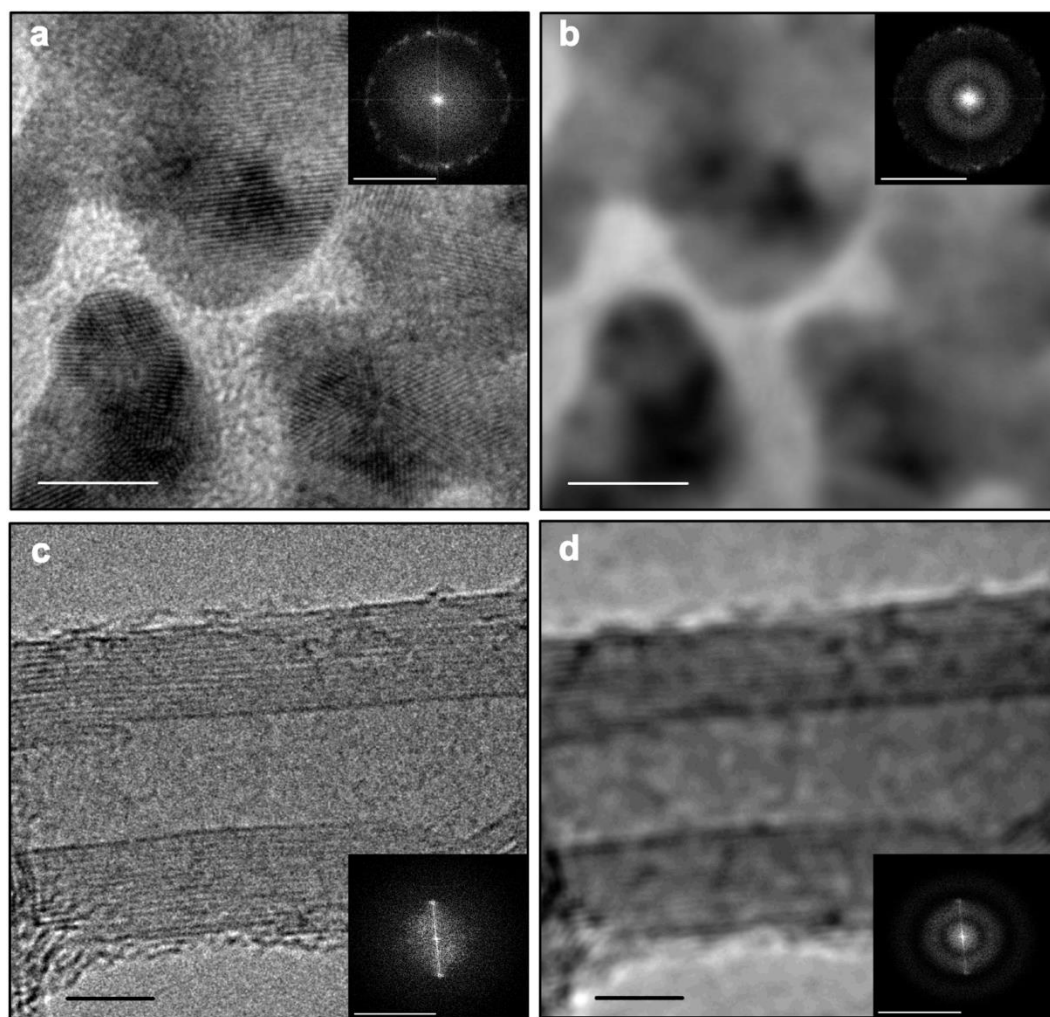
**Figure 5.8** Simulated UEM chromatic blurring in nanostructures. (a,c) Conventional TEM lattice-fringe images of Au nanocrystals (a) and a few-walled carbon nanotube (c). Intensity peaks in the FFTs (insets) illustrate the symmetry and the spacing of the observed fringes. (b,d) Simulated images at $\tau = 0$ (*i.e.*, with $\widehat{H}_c$ applied) illustrating the distinct photoinduced blurring that is predicted to occur during fs UEM. The 2.3 Å (111) atomic planes of the Au nanocrystals are almost entirely unresolvable, while the (002) graphitic planes in the carbon nanotube are faintly visible, as the corresponding peak in

the FFT falls within a side-peak of the chromatic transfer envelope (inset, d). Scale bars: images = 5 nm; FFTs = 5 $\text{Å}^{-1}$.

Although some information beyond the effective resolution defined previously ($r_{eff}$) is obtained, the observations described above have greater consequences for sub-picosecond atomic-scale imaging. Because high-resolution TEM relies on phase contrast, transient modulations of the chromatic contrast-transfer function will appear as deviations in focus conditions in the images and thus convolute the interpretation of structure for a given time-delay. It is worth noting that a spatially-homogeneous near-field over the selected area in the *x,y*-plane has been considered here. For a more general case (*e.g.*, the near-fields imaged by Piazza, *et al.*),[116] we may expect a projection of the *x,y* spatial features of the field in the form of blurring, such that distinct chromatic distortions occur in strong regions and weaker regions are only marginally affected. Nevertheless, these images embody the loss of most information pertaining to atomic planes as a result of the discrete, transient UEM chromatic aberration.

5.2.4 | Outlook

The photoinduced chromatic effects in UEM imaging discussed here represent another challenge in resolving concurrently the structure of materials in space and their ultrafast modulations in time, particularly for specimens which exhibit strong near-fields upon photoexcitation. Indeed, maintaining beam coherency and reducing temporal spread of the probing electron packet throughout the photogeneration, propagation, and imaging processes has been a theme in improving fs electron-imaging capabilities.[44] Notably, new iterations of hardware and methodology are being implemented, which

seek to achieve brighter, more coherent, and shorter electron packets through increased accelerating voltages (*e.g.*, MeV) and radio-frequency (RF) temporal-compression techniques.[117, 118, 119] Though these schemes combat complications arising during photogeneration and propagation, the resulting electron probes are still subject to effects arising at the specimen and subsequent imaging system.[120] Indeed, operating at MeV accelerating voltages generally enhances electron-photon coupling and the commensurate interaction strength. This, however, should in principle reduce the relative energy spread, which is encompassed by the *PSF* parameter $\delta_{\Delta E}$. Likewise, the condensed temporal envelope of RF-compressed electron packets are subject to strong coupling with evanescent fields [(*i.e.*, the non-linear regime shown in Fig. 5.6(c)] but are nonetheless a route to improved instrument-response times.

## 5.3 | Summary

### 5.3.1 | Instrument Response Characterizatoin via PINEM

In this chapter, we have described a robust method for *in situ* ultrafast electron packet and photon pulse characterization – in both the linear and the non-linear regimes. Current UEM experimental setups and instrument configurations are amenable to the described method owing to the sensitivity of the PINEM effect, especially in the near-collinear propagation geometry. Because electron-photon coupling occurs only in the evanescent near-fields, measured pulse properties are precisely those occurring at the specimen location; effects of angular distribution and dispersion on temporal coherence are all contained in the measurement. Linear-regression analysis of the non-linear (i.e., strong-interaction) regime demonstrates the importance of proper identification of the

experimental parameter space in order to ensure that measurements are accurate.  Finally, this *in situ* method can be used for simultaneous characterization of the instrument response and the specimen dynamics, thus providing a means to extract the initial ultrafast response to excitation, as well as an accurate determination of time zero.

5.3.2 | Discrete Time-Dependent Chromatic Aberrations in UEM

We have also outlined in this chapter how additional energy dispersion present when photoelectron packets interact with evanescent near-fields in the vicinity of the specimen results in an additional resolution-limiting chromatic aberration in UEM imaging.  Though the magnitude and the duration are a function of the excitation pulse properties, it is expected that this phenomenon will be especially apparent at magnifications that enable sub-nanometer resolutions.  Consequently, robust imaging of atomic planes and their modulations on the sub-picosecond timescale (*i.e.*, during the initial photoexcitation period) may require precise knowledge of the particular transient chromatic-dispersion function such that phase retrieval of lattice fringes may be performed.  Looking forward, continued identification of such fundamental physical processes − absent in conventional TEM − are expected to not only enable combined angstrom-fs real-space imaging, but to also lead to additional discoveries and development of new experimental approaches in UEM.

# 6 | Characterizing Instrument Response of a Thermionic Ultrafast Electron Microscope

In this chapter, we characterize the instrument response of a UEM equipped with a standard Wehnelt assembly and absent any modifications beyond the optical periscopes used for stroboscopic operation. By using a plasma lensing effect, we are able to map the photoelectron-packet population and total temporal response as a function of fs laser-pulse energy. Following establishment of the threshold for space-charge saturation and the effects of Wehnelt biasing for fixed cathode positions, we determine the instrument-response time for a range of populations spanning from near the single-electron regime up to ~$10^5$ electrons per packet. We observe a power-law trend for the total instrument-response time as a function of photoelectron-packet population, with extrapolation to the single-electron regime revealing a laser-limited temporal resolution. For populations only slightly larger than a single electron, we experimentally observe a broadening of the response time beyond the laser limit. We discuss possible mechanisms of the observed behaviors, with emphasis on identifying and controlling potential sources of error and measurement variability.

96

## 6.1 | Photoelectron Generation from a Truncated LaB$_6$ Cathode

### 6.1.1 | Photoelectron Packet Population from fs-UV pulses

In order to identify and characterize space-charge-limited effects, the photoelectron-packet population ($n_{e^-}$) as a function of UV laser-pulse energy was determined from UEM images of the cathode, with the applied Wehnelt bias effectively in an *off* or an *on* state. The electronic circuitry in the UEM used here is such that the Wehnelt bias and cathode heating supply are coupled, as in a conventional TEM equipped with a thermionic gun. Here, a bias in the *on* state refers to cathode resistive heating (thus, an applied Wehnelt bias) to a point just below the threshold for detectable thermionic emission, while the *off* state refers to no resistive heating (no applied Wehnelt bias). Data for several applied Wehnelt biases between the defined *off* and *on* states are included in Appendix E. Note that even in the *off* state, a gun crossover is generated and the cathode can be imaged, indicating a lensing effect still occurs at the Wehnelt aperture; optimal positioning of the LaB$_6$ behind the aperture ensures a high collection efficiency into the anode.[44]

Low and high UV pulse energies lead to qualitatively distinct photocathode images (Figure 6.1a). Structure is visible on the surface of the photocathode in the low-pulse-energy images but is absent at the high pulse energies, regardless of Wehnelt bias. By quantifying the behavior of $n_{e^-}$ as a function of UV pulse energy (Figure 6.1b), one can see that the images were generated in the under-saturated and nearly-saturated (*i.e.*, plateau) regimes for low and high pulse energies, respectively. This is expected, as increasing UV pulse energies with a fixed duration produce photoelectron packets of

increasing initial density until space-charge effects begin to dominate the observed

behavior. Less generally, a clear applied Wehnelt biasing effect can also be seen in the

low-pulse-energy images in Figure 6.1a; relatively low image intensity appears at an *xy*-

image position separate from the main beam. Such an effect could be due to over-

focusing of photoelectrons emitted at off-normal angles. Note that this effect was not

observed for the high pulse energies.
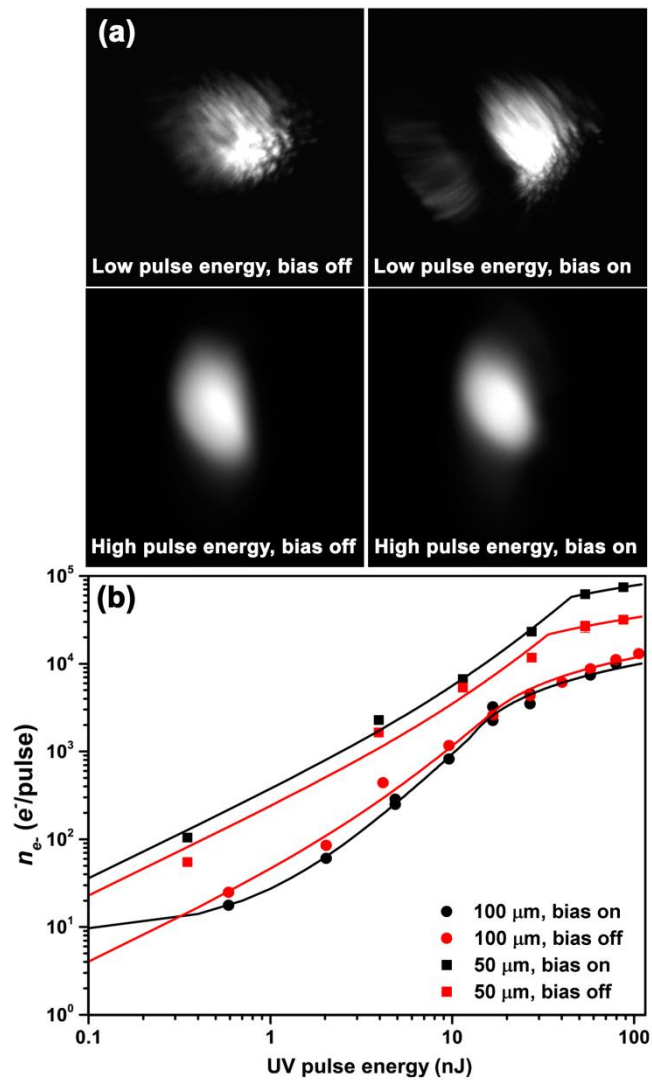
**Figure 6.1** Photoemission characteristics as a function of UV pulse energy and applied Wehnelt bias. (a) Images of the 100-μm cathode acquired for photoelectron packets generated with UV pulse energies of 0.3 nJ (low pulse energy, upper-two panels) and 90 nJ (high pulse energy, lower-two panels) with the Wehnelt bias in the *off* and *on* states (left-two and right-two panels, respectively). Note that acquisition times for the low pulse-energy images were adjusted such that contrast levels were approximately the same as for the high pulse-energy images. (b) Photoelectron-packet population ($n_{e\text{-}}$) versus UV pulse energy for the 50- and 100-μm cathodes (squares and circles, respectively) with the Wehnelt bias in the *off* and in the *on* states (red and black data points and model curves, respectively). The model and the counter-intuitive order-of-magnitude reduction in $n_{e\text{-}}$ for the larger photocathode are discussed in the text.

Quantification of $n_{e\text{-}}$ as a function of UV pulse energy from 0.3 to 100 nJ for both cathodes shows a weak (perhaps negligible) dependence on applied Wehnelt bias for the fixed LaB$_6$ positions used here (Figure 6.1b). The emission characteristics for each condition can be described with the image-charge-limited emission model outlined in Equation 6.1.[121]

$$n_{e^-} = \begin{cases} b_0 + b_1 F + \frac{b_2}{2} F^2 & F < F_0 \\ b_0 + b_1 F + \frac{b_2}{2} F_0{}^2 + n_{e^-}^{lim} \log\left(\frac{F}{F_0}\right) & F > F_0 \end{cases} \qquad \text{(E6.1)}$$

Here, a quadratic dependence on pulse energy ($F$) is assumed in the pre-saturation limit, where linear ($b_1$) and second-order ($b_2$) coefficients represent one-photon and two-photon emission processes, respectively. Above the saturation limit, which occurs at a threshold energy $F_0$ (nJ) and electron population $n_e^{lim}$ (electrons per pulse), logarithmic growth

occurs as a result of photoemission suppression due to the image-charge effect. Parameters for each of the curves shown in Figure 6.1b can be found in Table E1 of the Appendix E. For the 50-µm cathode, $n_e^{lim}$ is found to be 1.08E4 and 2.54E4, with $F_0$ values of 33.8 nJ and 45.2 nJ, for the *off* and *on* biasing states, respectively. Counter-intuitively, the 100-µm cathode exhibits significantly lower $n_e^{lim}$ and $F_0$ values of 4.90E3 and 16.7 nJ, and 3.97E3 and 12.6 nJ, for the *off* and *on* states, respectively.

Owing to the factor of four larger emission area, one would expect the 100-µm cathode to generate larger threshold values, all else being equal. Note, however, that a variety of factors affect the photoemission process and could contribute to the observed behavior, thus rendering direct comparison of different cathode sizes challenging. Such factors include cathode surface contamination, cathode surface topology, and the position and orientation of the cathode relative to the Wehnelt aperture.[44] Nevertheless, the $n_e^{lim}$ values (nearly $10^5$ electrons per pulse) found for the UEM instrument used here enable experiments to be conducted at relatively low repetition rates and moderate image magnifications, though a tradeoff in temporal resolution must be made with increasing $n_{e-}$ (discussed below).

6.1.2 | Effect of Biasing and Packet Population on Space Charge

Insight into the relative extent of transverse space-charge spreading can be ascertained from the blurring that occurs in UEM cathode images. This effect is evident in the select frames presented in Figure 6.2a, where resolvable cathode features become blurred with increasing UV pulse energy. This blurring can be quantified by generating two-dimensional Fourier transforms of the cathode images; non-vanishing intensity at

increasing spatial frequencies ($\mu m^{-1}$) corresponds to sharper features in the real-space images. Further, the width of radially-averaged, background-subtracted Fourier space peak (here, defined as the width at which 95% of the intensity is contained in the peak, $\Delta_{s95}$) is inversely proportional to the extent of real-space blurring (Figure 6.2b).
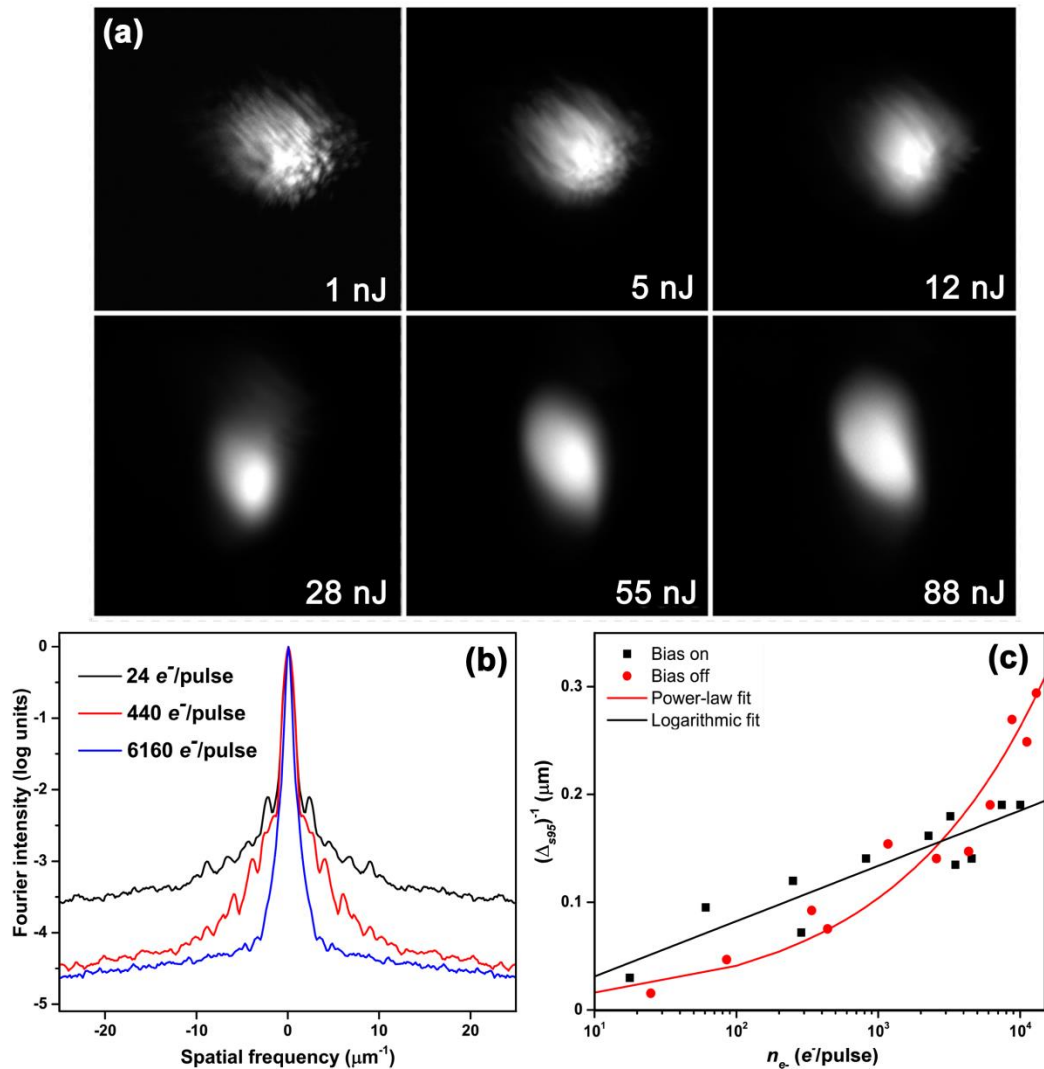


**Figure 6.2** Quantification of space-charge effects via UEM image analysis. (a) Select images of the 100-μm cathode generated with a range of UV pulse energies. The pulse

energies (nJ) used to generate the select frames are shown in the lower-right corner of each panel. (b) Two-dimensional discrete Fourier transforms of select images generated with measured $n_{e^-}$ values of 24 (black), 440 (red), and 6160 electrons per pulse (blue). (c) Effective spatial coherence [$(\Delta_{s95})^{-1}$, where $\Delta_{s95}$ corresponds to the width at which 95% of the intensity is contained in the peak] as a function of $n_{e^-}$ with the bias in the *off* (red circles) and *on* (black squares) states. The solid red and black curves are power-law and logarithmic fits to the data, respectively, which are included to highlight the respective trends.

In order to determine the effect of an applied Wehnelt bias (again, in the *off* and *on* states, as defined above) on space charge, the inverse of $\Delta_{s95}$ was plotted against $n_{e^-}$ (Figure 6.2c). Interestingly, dissimilar trends were observed for the *off* and *on* states; a power-law trend was observed for the *off* state, while logarithmic growth was seen for the *on* state, indicating application of a bias suppresses space-charge blurring at relatively large $n_{e^-}$ for the cathode positions used here. Note that the optimal cathode position may shift from what is predicted for the *off* state upon application of the biasing level used here (*i.e.*, just below the thermionic-emission threshold) and cause a corresponding shift in crossover position in the cathode-anode gap, which could explain the observed effect. Importantly, it has been suggested that application of a bias could also be used to reverse increases in energy spread that occur during the initial propagation period, with a commensurate temporal lengthening of the photoelectron-packet distribution.[38, 41] An evaluation of longitudinal broadening will be required to determine if such a tradeoff is at work in the UEM used here.

## 6.2 | Intstrument Response Characterization

### 6.2.1 | Significance of the Techniques

For physical phenomena occurring on timescales approaching the temporal resolution, determination of the UEM instrument response function (IRF) is necessary for deconvolution of intrinsic excitation dynamics, and evaluation of methods for generating femtosecond electron packets requires quantification of the pulse properties, ideally at the specimen location. In addition, a robust and precise method is needed for determining time zero (i.e., temporal overlap of the photon pulse and electron packet at the specimen).[31, 106, 110, 116] Thus, the techniques discussed in this chapter are an important tool in the interpretation of any experiment executed in the UEM.

### 6.2.2 | Instrument Response in the High Bunch-charge Regime

Determination of the dependence of UEM instrument-response time on $n_{e^-}$ for particular experimental conditions is required for isolation and quantification of initial ultrafast structural dynamics. As described in Chapter 2, this was accomplished here by using a plasma lensing effect in UEM imaging mode. Note that this can also be performed using electron energy-loss spectroscopy for suitably equipped UEM instruments (i.e. as described in Chapter 5).[38, 39, 41] Evaluation of the instrument temporal response for photoelectron packets with varying populations is presented in Figure 6.3 (Wehnelt bias in the *off* state). Note that application of a Wehnelt bias showed no discernible difference from the *off* state for the cathode positions used here (see Appendix E). In Figure 6.3a, a set of normalized kinetic image-intensity traces for measured values of $n_{e^-}$ ranging from 30 to over $10^4$ electrons per pulse are shown. The total instrument-

response time ($\sigma_t$, standard deviation of the resulting Gaussian peak function) was found to increase with increasing $n_{e^-}$, from 1 ps at 30 electrons per pulse to 4 ps at $10^4$ electrons per pulse. Further, it was found that the response exhibits a power-law trend (Figure 4a inset).
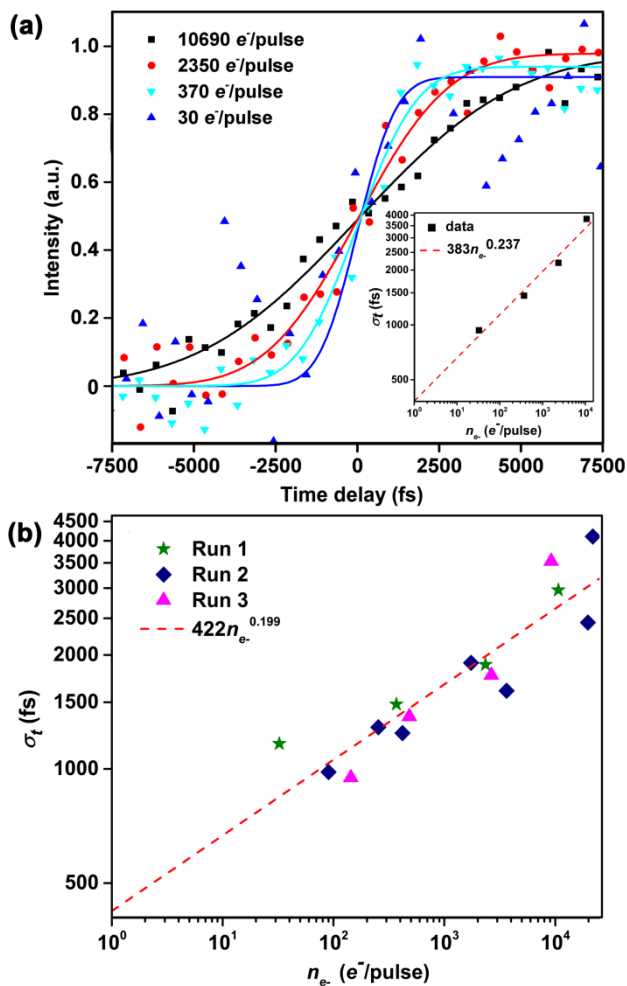


**Figure 6.3** Instrument-response time ($\sigma_t$) as a function of $n_{e^-}$. (a) Normalized kinetic image-intensity traces generated from photoelectron-packet populations of 30 (blue triangles), 370 (light-blue inverted triangles), 2350 (red circles), and 10690 (black

squares) electrons per pulse. The corresponding solid colored sigmoidal curves are fits of Equation 1 to the data. The intensity-change behavior is inverted compared to what is shown in Figure 1b for ease of fitting. In addition, the traces have been temporally aligned (for clarity) such that time zero occurs for each at the $t_{0.5}$ intensity-change point. The inset shows $\sigma_t$ as a function of $n_{e^-}$ for the four measured values (black squares) and a power-law fit to the data (dashed red line). (b) Compilation of three individual UEM time scans conducted on separate days (Run 1, 2, and 3) illustrating the behavior of $\sigma_t$ with varying $n_{e^-}$ and a power-law fit to the data (dashed red line).

In order to verify that the observed power-law trend results from effects of increasing bunch charge, the experiment was repeated three additional times, with each conducted on a different day (Figure 6.3b). The compiled triplicate data indeed follow a similar trend as shown in Figure 6.3a: a power-law exponent of 0.2 with an extrapolated single-electron-per-pulse temporal response of 400 fs ($\sigma_t$). Note that similar trends (in both functionality and magnitude) have been observed for comparable photoelectron-packet populations in ultrafast electron-diffraction instrumentation,[29] as verified with a two-dimensional mean-field model depicting packet propagation in the cathode-anode gap. While this gap is significantly larger in TEMs modified for stroboscopic operation, the electric potential is similar (~10 MV/m). Thus, the similar temporal trend for different instruments suggests comparable overall longitudinal broadening behavior via the Boersch effect. Interestingly, the extrapolated single-electron instrument-response time of 422 fs (994 fs FWHM, Figure 6.3b) returns a duration of 705 fs FWHM for the photoelectron-packet distribution after deconvolution of the measured 700-fs FWHM IR

pump pulse. This result indicates that the total instrument-response time is limited only by the laser-pulse durations when operated in the single-electron regime, at least for the pulse widths used here.

In addition to determining the instrument-response time, UEM imaging of the plasma lensing effect was used to find the position of time zero (here, the time at which the image-intensity change reaches 50%). Assuming sufficient plasma density is formed to cause onset of a detectable lensing effect on a timescale that is short relative to the total IR pump-pulse duration, the measured time zero can be approximated to represent true time zero (*i.e.*, the precise moment of Gaussian-peak overlap of the pump pulse and probe packet distribution at the specimen). As noted in the caption, the kinetic image-intensity traces shown in Figure 4a have been arbitrarily aligned at their half-maximum for clarity. In actuality, however, the $t_{0.5}$ time was found to vary (seemingly stochastically) over a range of approximately 6 ps for the three independent experiments shown in Figure 4b (see Appendix E, Fig. E3). Such behavior could arise from a variety of sources, such as variations in initial photoelectron-packet generation and propagation during acceleration (*i.e.*, the cathode to anode gap) and minor instrument voltage fluctuations over the period of data acquisition (which could further limit temporal resolution). Relatedly, the measured time-zero position was observed to shift by 80 ps upon switching from the 50- to the 100-μm cathode; recall the 100-μm cathode was positioned 100 μm further behind the Wehnelt aperture than the 50-μm cathode. As with the total instrument response, precise knowledge of the position and behavior of time

106

zero is critical for accurately isolating and quantifying initial ultrafast structural dynamics.

6.2.3 | Instrument Response Approaching the Single-electron Limit

While operating at large yet viable $n_{e^-}$ values offers increased UEM experimental flexibility, the temporal resolution decreases; here, the increase is from a laser-limited boundary of 1 ps FWHM (extrapolated to one electron per pulse) to 10 ps FWHM for $10^4$ electrons per pulse for 700-fs FWHM laser pulses (pump and probe; convoluted FWHM = 1 ps). Practically, image acquisition at relatively low instrument repetition rates is challenging in the single-electron regime. A simple approach to overcoming this is to increase the laser repetition rate at a fixed UV pulse energy – but only to the lowest value at which experiments can be reasonably conducted in order to minimize specimen heat accumulation. If this is accomplished via pulse picking, the laser-pulse durations will not change, and it may be expected that the instrument-response time will also remain unchanged, despite the increased average power being trained on the photocathode. Nevertheless, experimental rigor necessitates measurement of the response time when changing instrument conditions.

Accordingly, in order to determine the effects of increased repetition rate for conditions more closely approaching the single-electron regime (compared to the studies described above), the instrument-response time was measured at 600 kHz and with a UV pulse energy such that $n_{e^-}$ was measured to be 5.5 ± 1 electrons per pulse. These settings allowed for reasonable acquisition times (25 s) of images with sufficient signal-to-noise ratios for quantification. Figure 6.4a displays kinetic intensity traces generated from

three separate UEM image scans conducted over a span of three hours in total; the instrument-response time ($\sigma_t$, standard deviation of the resulting Gaussian peak function) was found to be $540 \pm 35$ fs.
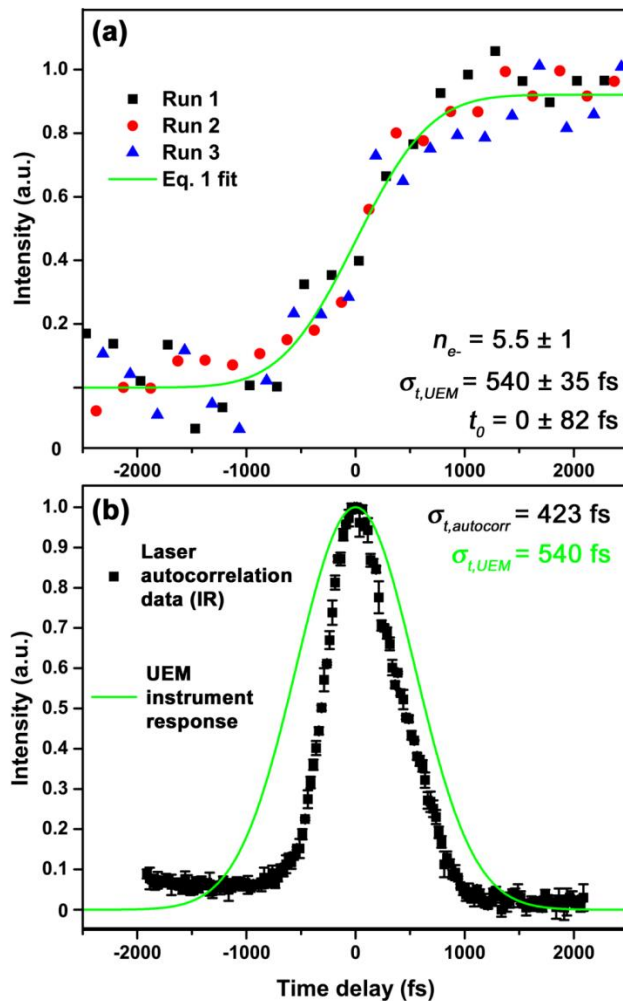


**Figure 6.4** Instrument-response time at an elevated repetition rate and near the single-electron regime. (a) Normalized kinetic intensity traces compiled from three separate image scans (Run 1, 2, and 3). The data is temporally shifted such that each run has approximately the same time-zero position ($t_0 = 0 \pm 82$ fs). The solid-green sigmoid

curve is the mean of the fits to each run. (b) Laser autocorrelation data (black squares; error bars represent one standard deviation) and UEM temporal instrument-response function (green peak function), which is the derivative of the Equation-1 (error function) fit to the kinetic traces. All $\sigma$ values are the standard deviation of a Gaussian peak function.

As discussed above, the minimum possible UEM instrument-response time (absent any electron-packet compression or other countermeasures) for a given laser-pulse duration ($\sigma_p$) is $\sigma_{t,UEM} = \sqrt{2}\sigma_p$, which is equivalent to $\sigma$ of the laser autocorrelation function ($\sigma_{t,autocorr}$). Thus, $\sigma_{t,UEM}$ will equal $\sigma_{t,autocorr}$ in the laser-limited case. Because dispersion is expected to be negligible for the 700-fs pulses used here, it is assumed that the UV and IR pulse widths are the same and that the IR autocorrelation function is a reasonable approximation of the actual UV-IR convoluted response. As shown in Figure 6.4b, $\sigma_{t,autocorr}$ for the IR pulses was measured to be 423 fs (996 fs FWHM). Recall that this value matches well with the extrapolated UEM single-electron instrument-response time in Figure 3b (422 fs, 994 fs FWHM). Compared to this, $\sigma_{t,UEM}$ for 5.5 electrons per pulse is broadened to 540 fs (1.3 ps FWHM). Thus, despite being near the single-electron regime (*i.e.*, well outside the space-charge and Coulombic explosion regimes), an apparent broadening of the photoelectron-packet distribution was still observed. This may be explained by noting that the UV photon energy is significantly higher than the LaB$_6$ work function (4.8 eV compared to 2.7 eV). This could result in an instantaneous momentum spread of the photoemitted electrons. It is important to again emphasize that the UEM instrument-response times measured here are specific to the employed optical-

excitation conditions; isolation of general physical phenomena from instrument-specific trends requires myriad additional systematic studies.

## 6.3 | Summary

In summary, we have systematically mapped the space-charge and temporal instrument-response parameter space as a function of photoelectron-packet population and applied bias for a UEM equipped with a conventional thermionic electron gun and absent any modifications beyond incorporation of optical periscopes. For IR pump and UV probe laser pulses of 700-fs FWHM durations, demonstration of instrument-response times ranging from 1 to 10 ps (FWHM), for laser-limited single-electron packets to those containing $\sim 10^5$ electrons, enables UEM experiments to be conducted at relatively low repetition rates, as demonstrated in the forthcoming chapter. Because the solid-state specimen is not refreshed in fs stroboscopic UEM, as is done for ultrafast molecular-beam experiments, operation at low repetition rates provides a means to allow for sufficient heat dissipation to occur between individual pump-probe events, thus minimizing deleterious effects. Further, precise determination of the UEM response time and time-zero position, for varied laser and TEM settings, is critical for isolating and quantifying the initial intrinsic ultrafast structural dynamics. Moving forward, it will be important to establish the limits of UEM instrument-response time for shorter laser-pulse durations in the single-electron regime, and to also determine the optimal conditions for combined Wehnelt biasing, photoelectron-packet population, and temporal resolution. It is expected that the results described here will provide a more quantifiable framework

upon which to base further developments and optimizations for achieving angstrom-fs real-space UEM imaging.

# 7 | Femtosecond Imaging and Diffraction of GHz-acoustic Waves in Thin-Films of Two-dimensional Atomic Crystals

Precise manipulation and control of coherent lattice oscillations via nanostructuring and phonon-wave interference has the potential to significantly impact a broad array of technologies and research areas. Resolving the dynamics of individual phonons in defect-laden materials presents an enormous challenge, however, owing to the interdependent nanoscale and ultrafast spatiotemporal scales. In this chapter, we report direct visualization of the nucleation, evolution, and decay of individual acoustic phonons in the vicinity of atomic-scale defects and nanoscale variations in lattice orientation via fs real-space imaging with an ultrafast electron microscope. Experimentally, we observe the launch of individual phonon wavefronts following coherent optical excitation of macroscopically-ordered but microscopically-disordered materials: here, few-layer tungsten diselenide ($WSe_2$). The transient low-energy elastic deformations associated with the propagating waves produce a slight re-orientation of the lattice and thus a localized, rapidly-varying Bragg condition. This manifests as coherent diffraction-

contrast wavetrains in the real-space images, the nucleation and dynamics of which are found to be strongly dictated by even minor lattice imperfections. Further, we observe that the appearance and directionality of the propagating wavefronts, as seen in the fs bright-field images, are strongly influenced by individual step-edges, interfaces, and crystal bending. By isolating and quantifying the transient contrast modulation, we extract the spatially-dependent vibrational-mode shapes and properties – namely, symmetries, frequencies, phase velocities, and decay times – over fields-of-view on the order of the phonon wavelengths. These observations open the way to detailed study of the effects of individual atomic-scale defects, spatially-varying lattice orientations, and associated strain fields on ultrafast energy propagation in less-than-pristine materials.

## 7.1 | Observation of Acoustic-phonon Wavefronts and Wavetrains in fs-Electron Imaging

Under stroboscopic bright-field imaging conditions, propagating periodic-contrast modulation arising from fs optical excitation was observed in the $WSe_2$ specimen (Fig. 7.1). From the sequence of fs electron images, phase velocities of 5.5 nm ps$^{-1}$, a commensurate periodicities of 40 ps, and ~25 to 40 GHz frequencies were determined for the traveling contrast modulations in $WSe_2$. This was accomplished by analyzing oscillations in the image intensity as a function of both space and time [Fig. 7.1(h); see Appendix G]. The close correspondence of the phase velocities to the bulk, in-plane speed of sound indicates the contrast dynamics arise from propagating acoustic phonons – major energy carriers emerging from electron-phonon coupling and reflecting the onset of coherent thermal transport. Note that GHz lattice-oscillation frequencies have also

been observed in crystalline Si with an ultrafast electron microscope via fs convergent-beam diffraction.[122, 123]
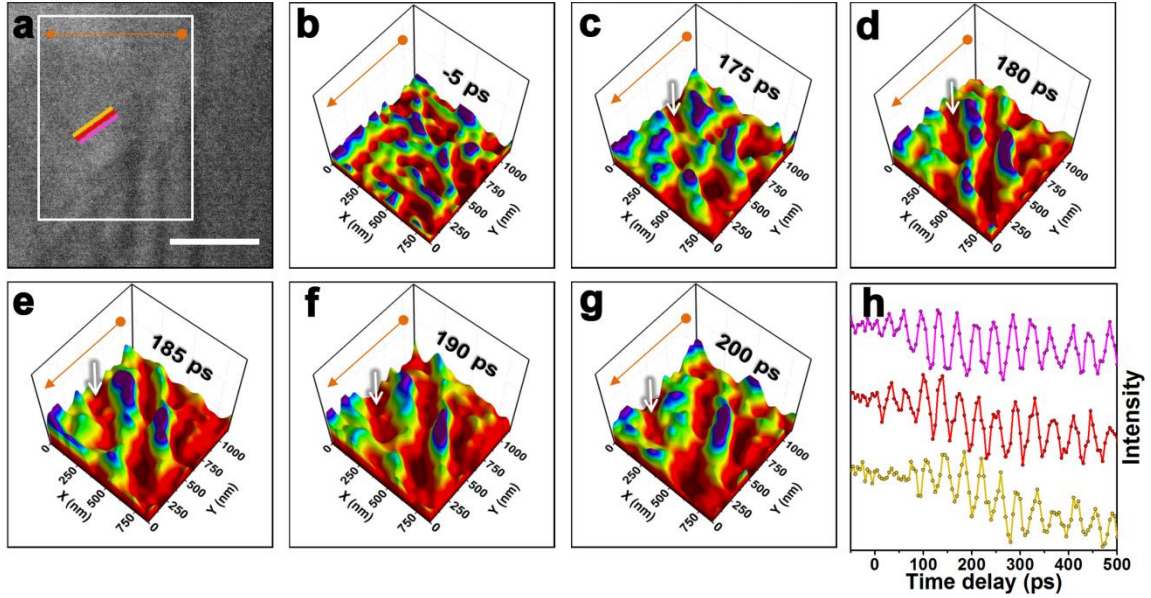


**Figure 7.1** Real-space fs electron imaging of single-phonon wavefronts in $WSe_2$. (a) Bright-field images of the $WSe_2$ flake obtained at -5 ps time delay. The images were acquired with a 25-kHz repetition rate with an 18-s integration time per frame. The three colored lines mark regions from which the mean intensity was quantified and used to generate the time traces in (h) (described below). The propagation direction is perpendicular to the colored lines. Scale bars = 500 nm. (b-g) Surface plots generated from an image series [region of interest = white rectangles in (a)] highlighting approximately one period of wavetrain propagation, with a pre-time-zero frame included for reference. Motion of individual wavefronts, which appear as a continuous, deep-red depression, is indicated by the white arrows. The orange arrow maps the orientation to the 2D images shown in (a). (h) Image-intensity measurements, obtained at the colored lines in (a), as a function of time delay (offset for clarity).

114

From the image series, it is immediately apparent that the phonon wavefronts do not emerge in a spatially uniform manner. Rather, within the few-layer WSe$_2$ flake, wavetrains are nucleated at a localized region along a distinct step-edge, and the subsequent propagation direction is perpendicular to the interface. The wavetrain emerges in one picosecond (ps; see below), is launched, and propagates at a velocity of 5.5 nm ps$^{-1}$ away from the step-edge.

### 7.1.1 | Emergence of a Phonon from a Terraced Interface

In order to precisely resolve the phonon dynamics at an individual step-edge, image series of WSe$_2$ were acquired with increased magnification and finer temporal sampling (500-fs steps). Within the region of interest highlighted in Figure 7.2, the intensity was observed to initially increase at a step-edge in the first few-hundred fs and continue to grow for approximately 10 ps before relaxation via emission of a traveling wave approximately perpendicular to the interface. The processed difference images [Fig. 7.2(b-f); see Appendix G] and corresponding time-dependent intensity traces [Fig. 7.2(g)] display the emergence mechanism of the in-plane acoustic phonons shown in Figure 7.1(a-h). Notably, the frequency of dynamic intensity at the step-edge is in accord with the interlayer echoing of back-and-forth acoustic phonons and resulting oscillating Moiré fringes[124, 125, 126] (see also Appendix G). It is therefore likely that the differential stress imparted on the interface by dephasing of the longitudinal *c*-axis waves across regions of differing height gives rise to the formation of the in-plane traveling phonons. Systematic studies to probe this and other aspects associated with the dynamic contrast mechanisms are currently in progress and will be described elsewhere.
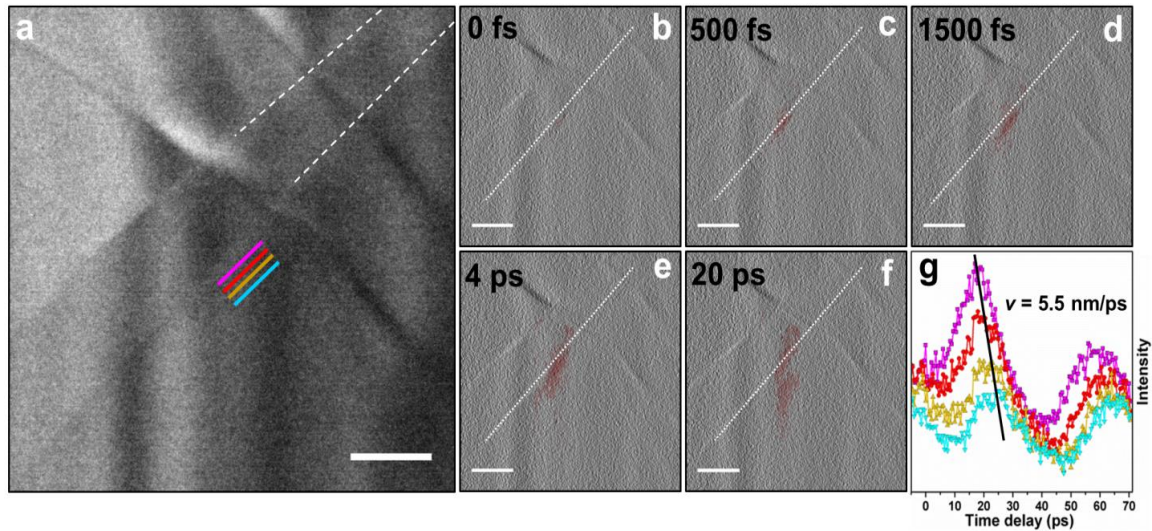
**Figure 7.2** Femtosecond-resolved phonon nucleation and launch at a crystal step-edge. (a) Bright-field image highlighting two step-edges (indicated by the partial dashed white lines) in few-layer $WSe_2$. The colored lines represent regions from which the mean intensity was quantified and used to generate the time traces in (g). The images were acquired with a 50-kHz repetition rate and a 20-s integration time per frame. (b-f) Select processed micrographs revealing the nucleation and emergence of a localized phonon wavefront (red). The dotted white lines indicate the position of the step-edge from which the wavefront emerges. (g) Intensity measurements obtained at the colored lines in (a) and plotted as a function of time delay. The slope of the line passing through the peaks of the first oscillation period reflects the wavefront velocity of 5.5 nm/ps. Scale bars = 200 nm.

### 7.1.2 | Spatially-dependent Frequencies, Symmetries, and Dispersion

The information contained in the image series can be further illustrated via a space-time surface plot (see Appendix G). In Figure 7.3(a), an analysis of contrast dynamics observed in the region between the $WSe_2$ crystal-vacuum interface and the

116

step-edge is summarized. Each streak corresponds to one period of an acoustic phonon, with the slope and width indicative of phase velocity and frequency, respectively. Such an analysis reveals the presence of multiple modes in this region, with a relatively high-frequency oscillation (phase velocity = 5.5 nm ps$^{-1}$) generated during the initial moments of excitation, and slower (0.9 nm ps$^{-1}$), lower-frequency dynamics dominating after a few-hundred ps. Similar spectral features identified with Brillouin light scattering from thin silicon membranes have been attributed to Lamb-wave modes.[127] Analogously here, the confinement of longitudinal acoustic phonons within the few-nanometer specimen thickness gives rise to in-plane propagating modes. These consist of traveling symmetric ($S_0^i$) and antisymmetric ($A_0$) interlayer displacements [Fig. 7.3(c)]. It has been predicted that such dilatational and flexural acoustic modes significantly influence thermal transport in layered materials.[128]
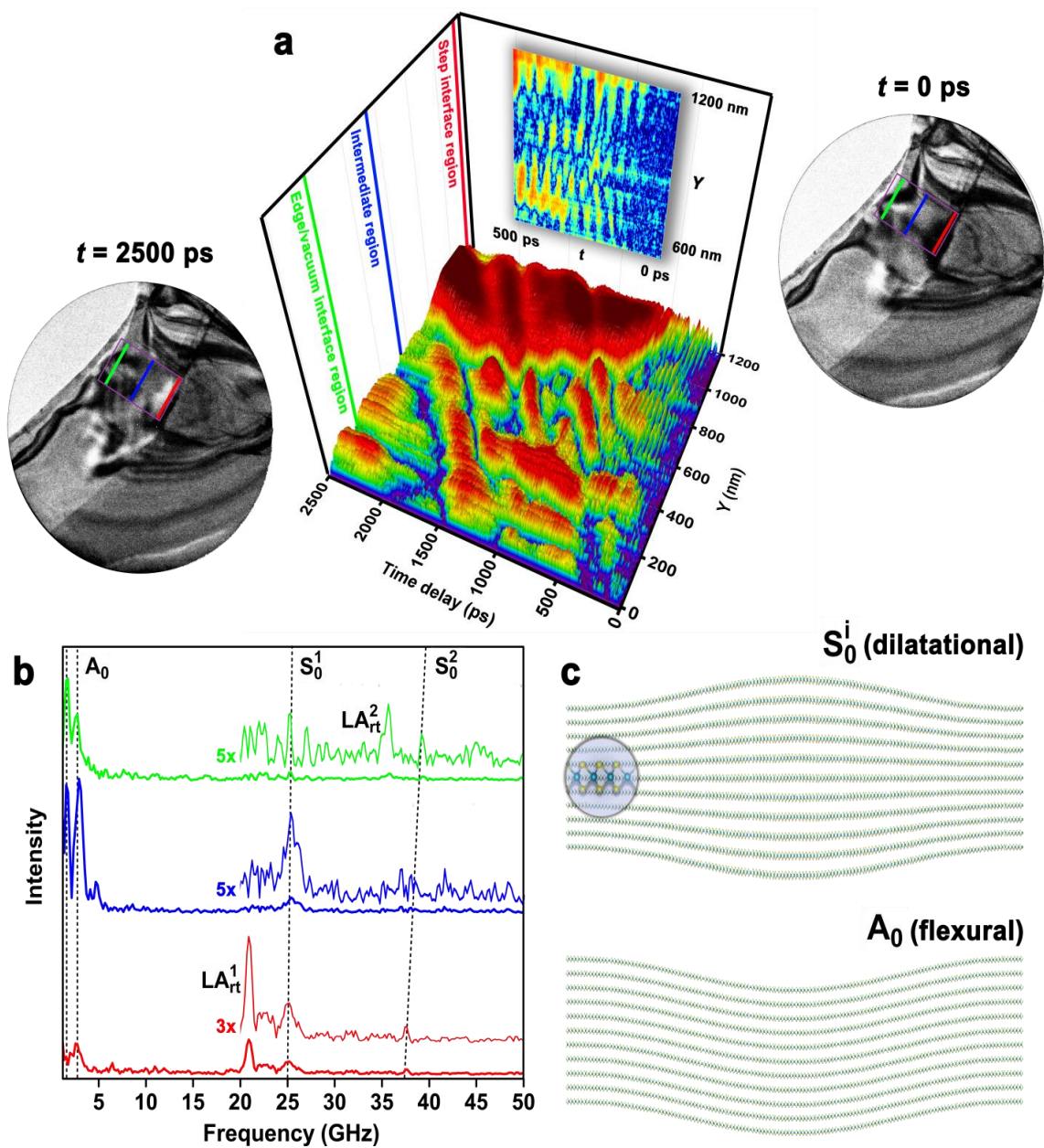
**Figure 7.3** Analysis of distinct, localized phonon modes in WSe$_2$. (a) Surface plot revealing the evolution of two primary modes, as observed in the region of interest highlighted in the accompanying images ($t$ = 0 and 2,500 ps; purple boxes). The images were acquired with a 25-kHz repetition rate and an 18-s integration time per frame. The colored lines demarcate the specific sub-regions analyzed. The thin, near-vertical streaks

118

predominantly in the sub-500-ps range and spanning the entire step interface region (600 to 1,200 nm; magnified in the inset) are produced by a relatively high-frequency mode, while the large amplitude, broad, diagonal features continuing out to the time-window limit are due to a more slowly-propagating low-frequency mode. (b) Time-domain Fourier transform of traces obtained from the sub-regions marked by the colored lines on the surface plot in (a). Peaks arising from echoing of longitudinal acoustic phonons ($LA_{rt}^i$) are labeled, while the traveling-wave modes ($A_0$, $S_0^i$) are indicated by the dashed lines, highlighting propagation dispersion. The superscript $i$ indicates waves emanating from the thicker step-edge region ($i = 1$) and from that bounded by the crystal-vacuum interface ($i = 2$). The spectra are offset for clarity. (c) Schematic of the symmetry of the propagating phonon modes with magnified view of a single layer. The dilatational modes ($S_0^i$, top) occur near 25 and 40 GHz, while the flexural modes ($A_0$, bottom) range from 2 to 5 GHz.

Inspection of the spatial dependence of the two phonon modes illustrated in Figure 7.3 via application of a discrete time-domain Fourier transform in three different spatial regions reveals that both are split into multiple branches, with the degree of excitation dependent on local morphology. A frequency trace near the crystal-vacuum interface returns dominant modes at 36 and 39 GHz [Fig. 7.3(b), green], whereas 21 and 25 GHz are found at the step-edge [Fig. 7.3(b), red]. In each case, the two dominant peaks correspond to the frequency of the back-and-forth $c$-axis acoustic phonons ($LA_{rt}^i$) and that of the resulting dilatational Lamb-wave mode ($S_0^i$). Consequently, the morphologically-dependent dispersion likely results from the difference in thickness

between the regions from which phonons originate. Additionally, the low-frequency flexural mode ($A_0$) is also split into multiple branches despite emanating from a region of uniform thickness. While this may occur from phonon interactions with bends and ripples in the flake, analysis of frequency traces obtained from the intermediate section [Fig. 7.3(b), blue] show that the $A_0$ mode is strongly damped upon reaching the step-edge. Such dynamics are the basis of the large disparities in thermal conductivity of layered materials.[48, 129]

### 7.1.3 | Discussion and Outlook

For all studies reported here, the laser-excitation wavelength used was 515 nm (2.41 eV). This photon energy is significantly larger than the band gap $WSe_2$ (1.6 eV). [130, 131] Accordingly, the roles played by charge-carrier excitation and recombination on localized acoustic-phonon nucleation and launch may be non-negligible. Indeed, the question of why acoustic phonons first appear at specific locations in the material is non-trivial to answer considering the sequence of events that occurs following fs excitation – especially in a disordered material – and the mechanisms of contrast formation in the bright-field images (discussed below). While this topic is the subject of current systematic studies in our lab, it nevertheless is perhaps worthwhile to draw comparisons to multi-photon pump-probe photoemission electron microscopy (PEEM). In this variant of PEEM, resonant excitation is used to induce surface-plasmon oscillations and image their launch, propagation, and evolution with fs resolution.[132, 133] An analogous methodology dubbed photon-induced near-field electron microscopy,[106] which is not reliant on resonant excitation,[107] has recently been used to image wave-particle properties

of surface plasmon polaritons and induce Rabi oscillations in swift, unbound electron packets.[115] With the resonant-excitation approach in mind, one can envision fs electron imaging experiments on acoustic-phonon dynamics, where the pump-photon energy is varied with respect to the band gap of the material under study. In this way, one may be able to determine the roles played by the various dynamic and transport phenomena at work.

Beyond the acoustic-phonon excitation and nucleation mechanisms, it will be important to quantify the precise manner in which contrast is formed in the fs electron images. Deviations of a few milliradians in the local Bragg condition can produce significantly different contrast patterns observed in bright-field micrographs. Indeed, this sensitivity to local morphology is what enables observation of dynamic contrast from small angular perturbations caused by in-plane propagating waves. It is expected that the nature of the contrast resulting from the acoustic waves is highly dependent on both vicinity to a zone axis and the specific zone axis itself. It is important to note that each of the videos of the $WSe_2$ flake presented in this study are acquired at slightly different orientations (due to the variability of sample insertion from one experiment to the next) and in fact show noticeable differences in static diffraction. In each case, however, the waves appear to emanate from the same features, and the frequencies and phase velocities extracted are the same. Nevertheless, the exact dependence of specimen orientation with respect to specific dynamic modulations indeed is an open question.

## 7.2 | Mechanisms of Contrast and Generation of Propagating Acoustic Waves

Imaging of acoustic-wave dynamics using stroboscopic UEM is enabled by the sensitivity of electron-scattering vectors to slight, time-varying orientations of the crystal lattice, in much the same way as occurs in static, conventional TEM diffraction-contrast imaging of bend contours. As photogenerated lattice waves travel across the imaging field-of-view, the atomic planes respond via local deformation, which causes tilting and oscillation of the (reciprocal) lattice with respect to the fixed Ewald sphere. This produces a corresponding local modulation of the Bragg condition. By inserting an aperture into the back focal plane of the objective lens, strongly-scattered electrons emerging from specimen regions satisfying the Bragg condition are blocked from entering the imaging (projection) system (Fig. 7.4). Accordingly, the specimen region from which this scattering occurs appears dark in the resultant bright-field image, and the propagating lattice waves manifest as coherent, propagating contrast waves in the UEM videos.[43] Further, it is expected that the degree of lattice deformation will manifest as variations in contrast strength; that is, larger local elastic strains should produce stronger contrast, depending upon the initial crystal orientation with respect to strongly-scattering conditions.
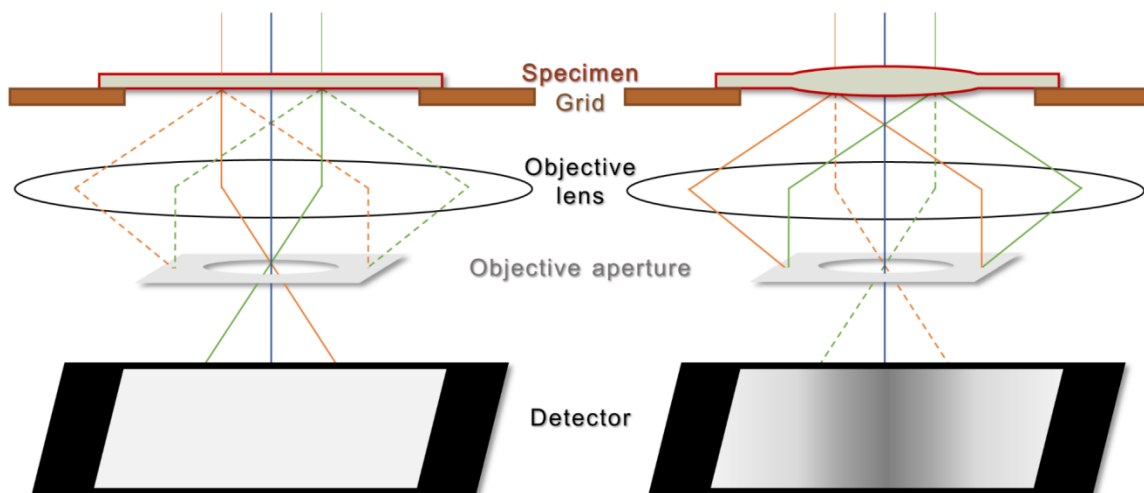
**Figure 7.4** Simplified schematic of the UEM imaging-contrast mechanism arising from transient local elastic strain. (Left) Freestanding specimen prior to laser-induced deformation. Under this condition, the diffracted beams (green and orange dashed lines) are only weakly excited, and the resulting image contrast is weak owing to most incident electrons being contained in the direct beam (green and orange solid lines; blue solid line is the optic axis); the direct beam is selected for image formation with the objective aperture. (Right) Upon photoexcitation, elastic deformation of a properly-oriented specimen produces a spatially-varying orientation, with some regions satisfying the Bragg condition, thus leading to strong excitation of the diffracted beams (green and orange solid lines). This produces a relative reduction in the number of incident electrons contained in the direct beam (green and orange dashed lines) and an increase in the image-contrast strength. The black regions at the edges of the detector represent the electron-opaque TEM grid bars.

7.2.1 Quantifying BF-image Series of Phonon Propagation in WSe$_2$

Discussed in the previous section, propagating contrast features were observed in few-layer flakes of $WSe_2$. $WSe_2$ has a layered atomic structure with strong covalent in-plane bonding and weak van der Waals bonding between layers. Upon thinning to a few layers, $WSe_2$ transitions from an indirect to direct band gap, making it an appealing candidate for next-generation optoelectronic applications.[64, 134, 135] Here, however, the flakes are expected to display behaviors more-closely matching those of the bulk regime, which exhibits an indirect band gap of approximately 1.3 eV.[136] Both UEM bright-field imaging and selected-area diffraction were conducted on a single flake of $WSe_2$, the results of which were correlated in order to develop a comprehensive atomic to mesoscale picture of the photoexcited structural dynamics. An overview of the $WSe_2$ specimen, and the observed real-space structural dynamics, is provided in Figure 7.5. Following fs excitation at 515 nm, two distinct acoustic-phonon behaviors are discernible with UEM bright-field imaging. In this case, the distinct behaviors are differentiated by the morphological defect features from which they emerge; one wave train is observed emanating from a vacuum/crystal interface, while the other emerges from a terraced (*i.e.*, crystal/crystal) interfacial region. Each wave train displays a distinct oscillation frequency; 40 and 25 GHz for the vacuum/crystal and terraced wave trains, respectively [Fig. 7.5(B) and (C), respectively]. Notably, the wave trains are most apparent in regions where contrast strength sharply varies spatially. Accordingly, small angular modulations in local lattice orientation, relative to the fixed Ewald sphere, due to relatively low-energy acoustic-phonon propagation give rise to discernible diffraction-contrast dynamics in the UEM images series.
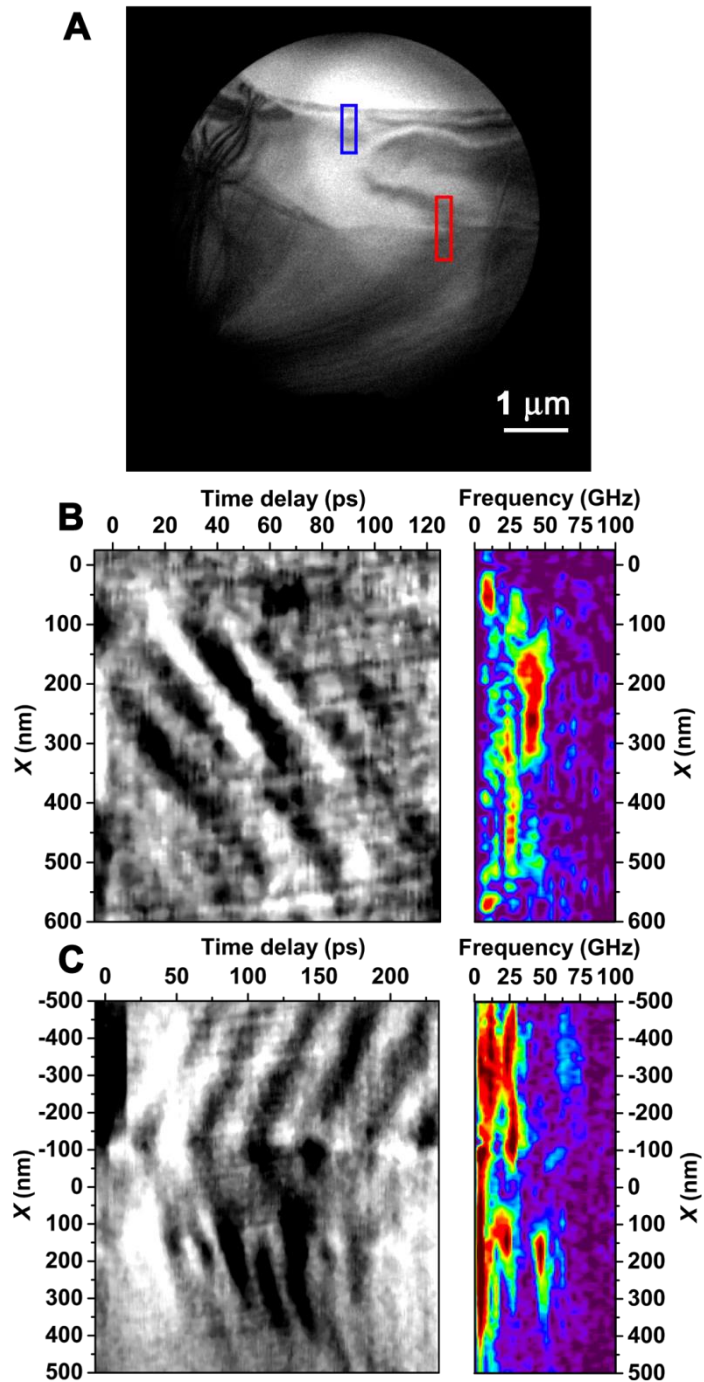
**Figure 7.5** Quantification of propagating acoustic waves in a freestanding WSe₂ flake from a UEM bright-field image series. (A) Representative bright-field UEM image of a

WSe$_2$ flake, with two distinct interfaces highlighted: the vacuum/crystal interface (blue rectangle) and a terraced interface (red rectangle). The black circle around the periphery of the image is due to an inserted selected-area aperture. (B, left) Space-time contour plot generated from the vacuum/crystal interfacial region highlighted with the blue rectangle in panel (A). Each time point was generated by first averaging image counts along the horizontal direction of the region of interest and then subtracting pre-time-zero values to isolate the relative change. For reference, the 0-nm spatial position corresponds to the vacuum/crystal interface. (B, right) Fourier transform of the temporal traces generated by analyzing the space-time contour plot. The frequency of the mode emanating from the vacuum/crystal interface is approximately 40 GHz, with velocities ranging from 5.5 to 7 nm/ps. (C, left) Space-time contour plot generated from the terraced interfacial region highlighted with the red rectangle in panel (A). For reference, the 0-nm spatial position corresponds to the approximate position of the terrace in the region of interest. (C, right) Fourier transform of the temporal traces revealing the presence of an acoustic wave of approximately 25 GHz emanating and propagating away from the terrace at 8 nm/ps, with an apparent double resonance of this mode (50 GHz) appearing in the thicker region of the crystal (*i.e.*, lower region of the image).

The behavior of the WSe$_2$ contrast dynamics at each defect can be quantified by defining a region of interest and generating line scans parallel to the propagation direction from a select region of interest (by averaging image intensity orthogonal to the propagation direction) and plotting the resultant profiles as a function of time. This approach is used to produce space-time contour plots displaying coherent contrast

126

oscillations arising from the phonon wave trains [Fig. 7.5(B) and (C)]. From such plots, one can identify both the propagation velocity of each wave front (slope of the contrast features) and the spatial frequency of the wave train across the region of interest. For the $WSe_2$ flake studied here, the terraced interface defines a spatial thickness transition region, with the thinner region spanning from the terrace to the vacuum/crystal interface. Here, the thinner region supports the 40 GHz wave train, which propagates at approximate velocities ranging from 5.5 to 7 nm/ps (depending upon which wave front is measured). In addition, the wave train is observed to propagate away from and along a vector approximately normal to the interface and oriented toward the terrace. Conversely, the wave train emanating from the terrace displays more complex behavior; two distinct wave trains can be seen emerging from the terrace and propagating away from and along vectors approximately normal to the interface. This behavior is manifested as contrast features in the contour plots having comparable slopes but different signs, thus illustrating the opposite propagation directions but comparable velocities (ranging from 7 to 11 nm/ps). Beyond 100 nm from, and on either side of, the terrace, oscillation frequencies of approximately 25 GHz are observed. Interestingly, a peak at 50 GHz is clearly present in the specimen region below the terrace (relative to the image plane); it is unclear whether this is a physical splitting of the wave via propagation through a specimen feature or an artifact of the complex contrast mechanisms in that particular region.

The distinctly different wave-train frequencies in the relatively thick and thin specimen regions suggest that local properties and behaviors are dictated by distinct

specimen morphologies and structural features. An explanation for the origin of the in-plane modes in $WSe_2$ is that initial photoexcitation and rapid $c$-axis expansion leads to excitation of transverse phonons, the nucleation and propagation direction of which is dictated by spatial discontinuities in elastic properties along particular wave vectors. Indeed, GHz oscillations in graphite, as measured with UEM, have been attributed to propagation of longitudinal waves along the $c$-axis stacking direction and reflection at the outer layers.[124, 125, 126] Similarly here, it is hypothesized that the back-and-forth motion of $c$-axis longitudinal phonons ultimately couple to in-plane propagating modes via interfacial stresses. These in-plane modes then manifest as traveling contrast features having distinct wave fronts and vectors in the UEM bright-field image series due to local modulation of the Bragg condition by the propagating elastic strain. As shown below, this hypothesis is supported by results obtained from correlative UEM selected-area diffraction studies and linear elastic modeling.

7.2.2 | Correlating Real-space Observations with Ultrafast SAED

Summarized in Figure 7.6 are UEM selected-area diffraction studies conducted on relatively thin and thick $WSe_2$ specimen regions of interest [dashed blue and dashed red circles (corresponding to the aperture size and location), respectively, in Fig. 7.6(A)]. The composite representative diffraction pattern in Figure 7.6(B), where scattering from the thin and thick regions is mapped in blue and red RGB channels, respectively, confirms that specimen crystallinity is both continuous and oriented across the terrace interface, though the relative intensities of the diffracted beams vary between the regions

due to tilting effects. That is, the two regions are portions of an oriented crystal rather than individual and disparate crystal grains in a polycrystalline film.

Here, with UEM, monitoring Bragg-spot properties as a function of time reveals ultrafast variations in both the spacing and angular orientation of diffracted beams (relative to the direct beam). For example, Figure 7.6(C) summarizes the extracted dynamics of the (202) reflection, which is present in diffraction patterns from both specimen regions [white square in Fig. 7.6(B)]. Importantly, the onset of dynamics is observable as an initial 0.05% contraction in the inverse $d$-spacing ($\Delta d^{-1}$) in the trace from the thin region. The reciprocal-space contraction (*i.e.*, real-space expansion) occurs over approximately 3 ps and is the precursor to coherent oscillations. Note that the initial temporal change is likely instrument limited at the UEM settings used here, as mentioned above. The onset of resolvable angular resonances occurs approximately 15 ps after this initial real-space expansion, which may correspond to the first reflection of a $c$-axis longitudinal phonon from an outer crystal layer, after which oscillations in both angle and position begin and continue over the entire temporal window (here, beyond 230 ps). The observed transient modulations in diffracted-beam position indicate that the corresponding lattice planes exhibit both shear motion and lateral expansion and contraction, an effect which may stem from $a$- and $b$-axis displacements of in-plane phonons. Figure 7.6(D) displays Fourier transforms of both the angular and radial diffraction-spot dynamics from each selected area; frequencies of 21 and 38 GHz for the thick and thin regions, respectively, are apparent in both degrees of freedom. Using the relation $T = 0.5\tau v_s$ – where $T$ is the flake thickness, $\tau$ is the corresponding oscillation

period (*i.e.*, $1/f$, where $f$ is the oscillation frequency), and $v_s$ is the speed of sound along the propagation direction (1.9 nm/ps for the WSe$_2$ *c*-axis) – thicknesses of 45 and 25 nm for the thick and thin regions, respectively, are extracted.
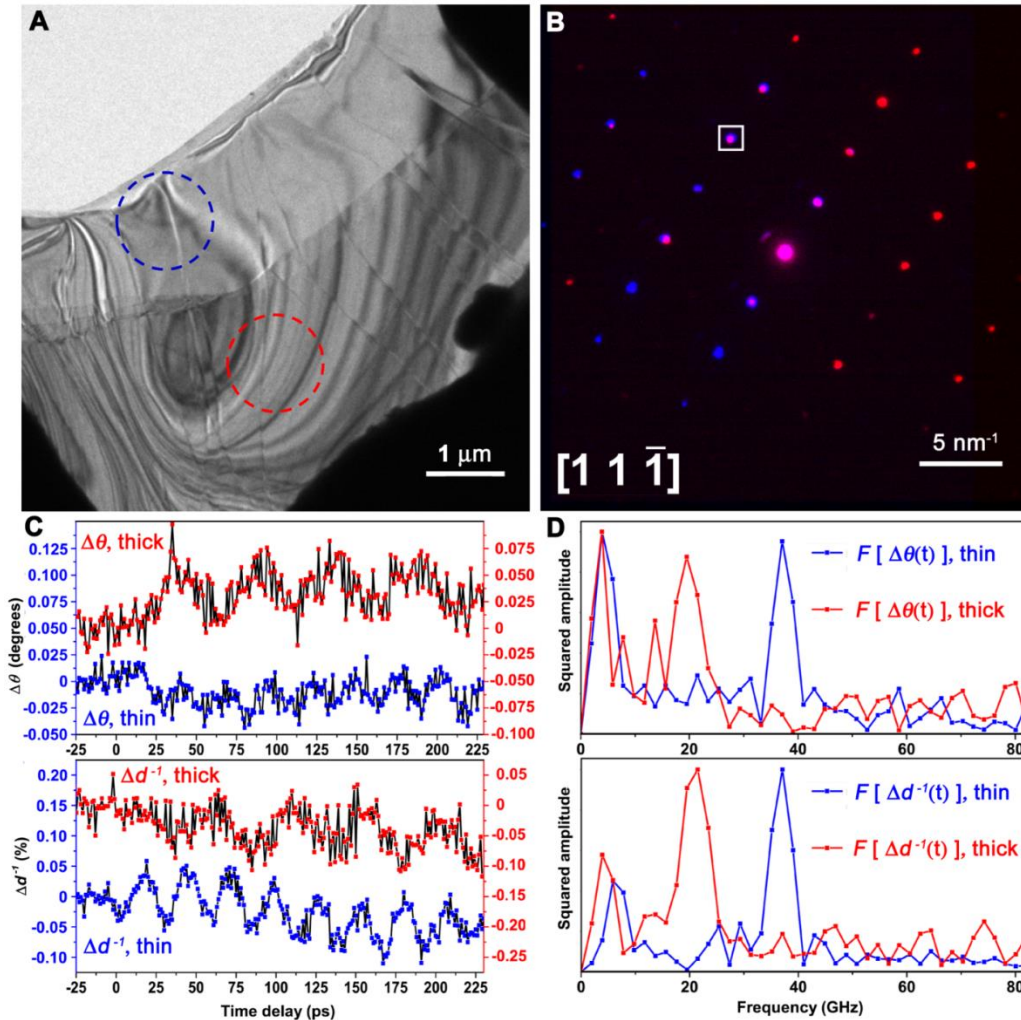


**Figure 7.6** Selected-area diffraction dynamics in relatively thin and thick regions of a freestanding WSe$_2$ flake. (A) Representative UEM bright-field image illustrating the relatively thin (blue dashed circle) and thick (red dashed circle) regions from which selected-area time-resolved diffraction data was obtained. (B) Composite frame

consisting of UEM parallel-beam diffraction patterns acquired approximately along the [11$\bar{1}$] zone-axis for the thin (blue) and thick (red) regions of interest; overlapping intensity between the two regions appears pink. The white square highlights the analyzed (202) reflection, which has significant diffracted-beam intensity contributed from both regions of interest. (C) Transient behavior of the angular orientation ($\Delta\theta$, top) and diffraction-spot spacing ($\Delta d^{-1}$, bottom) of the (202) reflection acquired from both the thin (blue data points) and thick (red data points) specimen regions. The left (blue) and right (red) axes correspond to data from the thin and thick regions, respectively. Note that an initial contraction of the (202) diffraction-spot spacing (indicative of an initial interlayer expansion) is evident in the time trace from the thin specimen region; this initial expansion induces the oscillatory elastic response observed in both the real- and reciprocal-space UEM studies. (D) Fourier transforms of the oscillatory behavior shown in panel (C) from both the thin and thick specimen regions. Frequencies of 38 GHz in the thin region and 21 GHz in the thick region, respectively, are evident in the spectra for both $\Delta\theta$ (top) and $\Delta d^{-1}$ (bottom). The observed behavior is ascribed to beating of $c$-axis longitudinal waves between the flake surfaces within regions of differing thickness.

The atomic-level picture of structural dynamics revealed with ultrafast diffraction supports the hypothesis pertaining to the origins of GHz propagating, in-plane acoustic-phonon modes observed with UEM bright-field imaging. In short, an initial interlayer expansion induces an elastic response that launches compression waves that propagate along the $c$-axis layer-stacking direction. Confinement and interaction of these waves with the specimen surfaces (*i.e.*, the outer-most specimen layers) couples to in-plane

modes through differential stresses at discrete interfaces (*e.g.*, vacuum/crystal and crystal/crystal). The physical picture of this process is explained in more detail in the next section. Note, however, that the exact and detailed nature of initial fs optical coupling to the observed thermoelastic behavior (especially with respect to distinct nanoscale defects and interfaces) is not directly addressed with the experiments reported here. Accordingly, future experiments will focus on examining timescales and amplitudes of the initial onset of dynamics as a function of photoexcited charge-carrier density and excitation wavelength in effort to elucidate the nature of electron-phonon coupling leading to local and (eventually) global elastic deformation.

7.2.3 | Simulating Acoustic-phonon Dynamics in WSe$_2$ with a Time-dependent Linear-elastic Model

In order to gain further insight into the nature of the observed coherent contrast waves, a finite-element simulation was performed using a transient linear-elastic model with the COMSOL Multiphysics Structural Mechanics software module. Here, free boundary conditions were assumed, and the initial and initiating condition for phonon launch was an instantaneous, depth-dependent displacement along the $z$-axis (*i.e.*, layer-stacking axis) in the crystal. This initial $z$-displacement represents the ultrafast, optically-induced interlayer expansion observed in the diffraction experiments. That is, the initial condition was set to be $\Delta z(z, t = 0) = Ae^{-\frac{z}{\alpha}}$, where $z$ is the coordinate along the WSe$_2$ $c$-axis, $A$ is the magnitude of the initial displacement, and $\alpha$ is the inverse of the attenuation coefficient (with units of length). For illustrative purposes, (exaggerated) values of $A$ and $\alpha$ have been chosen to be 7.5E-2 nm and 3.2 nm, respectively. This model was applied to

132

an idealized mesh structure of the two regions of interest – the vacuum/crystal and terraced (crystal/crystal) interfaces – embodying a two-dimensional representation of the experimental geometry of the WSe$_2$ flake. For the hexagonal symmetry of the WSe$_2$ flake, five independent elastic constants make up the anisotropic elastic stiffness tensor, represented by the elasticity matrix:[137]

$$C_{ij} = \begin{bmatrix} C_{11} & C_{12} & C_{13} & & & \\ C_{12} & C_{11} & C_{13} & & 0 & \\ C_{13} & C_{13} & C_{33} & & & \\ & & & C_{44} & 0 & 0 \\ & 0 & & 0 & C_{44} & 0 \\ & & & 0 & 0 & \dfrac{C_{11} - C_{12}}{2} \end{bmatrix}$$

Here, the $C_{11}$ and $C_{33}$ values are 300 and 34 GPa, respectively, to match compressional speeds-of-sound along the corresponding axes [i.e., $C_{33} = \rho v_{s,c}^2 = 9320$ kg/m$^3 \cdot (1.9$ nm/ps)$^2 = 34$ GPa], the $C_{44}$ value is 19 GPa,[138] and the $C_{12}$ and $C_{13}$ values are each set to 15 GPa.

Select frames from the simulation, representing discrete time points, are shown in Figure 7.7 (A) and (B). As can be seen in the simulations, the initial depth-dependent expansion results in a coherent compressional wave that propagates back and forth along the c-axis between the outer layers. At the free edge of the specimen [Fig. 7.7(A)], stress imparted by propagation of the longitudinal wave results in rapid coupling to in-plane displacements that emanate from the vacuum/crystal interface (i.e., the left edge of the flake in the simulation) owing to abrupt spatial variation in elastic (acoustic) properties. After 100 ps, a coherent wave train of in-plane compressional displacements can be

133

discerned ($t = 100$ ps for $x$-displacement), the emergence of which becomes clear after 50 ps. Similarly, in-plane displacements arise at the terraced interface when the $c$-axis longitudinal waves on either side of the interface become out of phase owing to variations in total transit time. For this type of defect, the in-plane displacements are observed to subsequently propagate away from the interface in both directions and take on a tilted, non-uniform spatial frequency as time progresses.
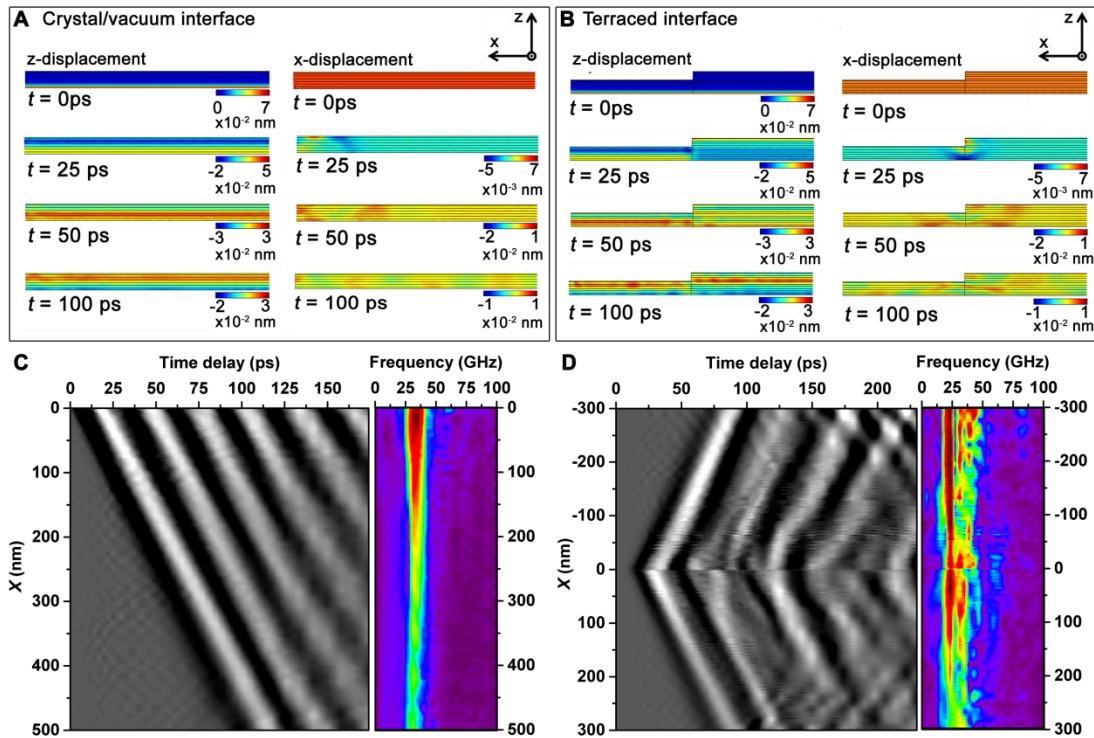


Figure 7.7 Time-dependent linear-elastic simulation of GHz propagating acoustic waves at interfaces in WSe$_2$. (A) Select transients from the simulation mapping both the $z$- and $x$-displacements (*i.e.*, the $c$-axis and in-plane directions, respectively) in regions near the vacuum/crystal interface. (B) Select transients from the simulation mapping both the $z$- and $x$-displacements in regions near the terraced interface. In both (A) and (B), the initial

134

depth-dependent photoinduced expansion launches a compressional wave that oscillates along the $z$-axis. This motion couples to in-plane (*i.e.*, $x$-axis) modes at the edge of the specimen (A) and at the terrace (B) owing to the discontinuous elastic properties at each interface. (C and D, left) Space-time contour plots of the $x$-displacement generated by averaging in-plane line-scans at 3-nm intervals within the specimen. (C and D, right) Space-frequency contour plots of the $x$-displacement illustrating near-quantitative agreement with experiment; behaviors that are quantitatively similar to experimental observations are captured in the simulations, including the presence of specimen-thickness-dependent frequencies and speed-of-sound wave trains emanating from the interfacial regions.

In order to further quantify the initiation and launch processes and to compare to experimentally-observed contrast dynamics, the $x$-displacement simulation data was converted into spatially-averaged line scans of intensity (sampled from varying crystal depths) and plotted as a function of time. Shown in Figure 7.7 (C) and (D) are simulated space-time contour plots and corresponding Fourier transforms displaying spatial frequency distributions. As with the experimental data shown in Figure 7.5 (B) and (C), the simulated space-time contrast oscillations depict the propagation direction and velocities of the $x$-displacements, with the slopes of the contrast bands dictated by the in-plane compressional speed of sound and, thus, the commensurate $C_{11}$ elastic constant. Further, the oscillation frequency of the in-plane waves stems from the specimen resonant frequency dictated by the crystal thickness and the out-of-plane compressional speed of sound (*i.e.*, the commensurate $C_{33}$ elastic constant). Indeed, the spatial and

interfacial dependence of the experimentally-observed phonon frequencies are nearly quantitatively reproduced in the finite-element simulations.

While the simulations support the hypothesized formation mechanism and coupling behavior of the experimentally-observed GHz acoustic phonons, some disagreement remains. First, the absence of low-frequency features in the simulation likely results from a simplification of the actual specimen geometry and exclusion of bends and ripples that give rise to these features in the experimental data [see, for example, the spatial frequency region below 25 GHz in Figure 7.5(C)]. Second, the model employs a projection along one in-plane axis of the structure, and thus does not provide an indication of the wave-front shape in two spatial dimensions. For the UEM experiments, the wave-front shapes and propagation directions can evolve and become more complex depending upon the orientation of the two in-plane axes with relation to discrete and discontinuous morphological features. Additionally, the values of the elastic constants can dictate the behavior of the phenomena in the simulation, and these values are often not known for advanced materials or defect-laden specimens. Indeed, future efforts could focus on determining if quantification of the observed acoustic-phonon dynamics can be used to extract the anisotropic elastic properties of nanostructures. Finally, the continuum model applied here is relevant to bulk materials and geometries; while a majority of the presently-observed phenomena is well represented in the simulation, future work will determine if a transition to more complex behavior occurs upon reduction of flake thickness (*i.e.*, within a transition region from atomistic to continuum regimes).[42, 139, 140]

## 7.3 | Summary

In conclusion, we have reported the direct, real-space imaging of acoustic-phonon dynamics in macroscopically-ordered but microscopically-disordered few-layer $WSe_2$. Via fs electron imaging, we have discovered that phonon nucleation and launch occurs at discrete spatial locations along individual step-edges, and that the appearance of coherent, propagating wavefronts are extremely sensitive to the shapes of local strain fields and vacuum-crystal interfaces. Further, analysis of ps contrast modulation reveals the phase velocities, frequencies, and symmetries of the modes, with the spatial and layer-thickness dependence of the oscillations being resolved. The acoustic waves, discernable in real space via local elastic strain of the lattice leading to modulations of the Bragg condition and the resulting commensurate diffraction-contrast dynamics, arise from interfacial stress caused by initial excitation and confinement of compressional waves along the $c$-axis stacking direction within the specimen-layer boundaries. The transient diffraction-beam scattering-vector magnitudes and angular orientations, as measured with UEM selected-area diffraction, support both the proposed dynamic image-contrast mechanisms and the physical origins of the acoustic wave trains. Guided by these experimental insights, a time-dependent linear-elastic finite-element simulation of the mechanical deformations was developed and applied, the results of which further supported the proposed depiction of the ultrafast photoinduced elastic strain-wave dynamics. Moving forward, application of combined UEM imaging and diffraction modalities on select, nanoscale specimen regions are expected to be useful in uncovering

the physical origins of other phenomena, including (spatial) energy nucleation, propagation, conversion, and decay in myriad materials and composite systems. In particular, one could envision using these approaches to uncover the spatially- and temporally-varying anisotropic elastic tensors, especially as affected by discrete (and dilute) structural discontinuities. With the spatiotemporal resolutions accessible with UEM, it is also expected that much insight could be generated regarding atomistic-to-continuum structural dynamics, which will aid in informing the continued development of multiscale modeling approaches.

# 8 | Conclusions

Throughout this work, we have outlined the development of UEM as a tool for the investigation of nanoscale energy transport. Uniquely, UEM has the ability to probe phonon transport processes on the relevant condensed time- and length-scales – that is, femtoseconds and nanometers, respectively. We have studied a variety of phenomena in two-dimensional atomic crystals  and discussed progress in methodologies in operation of a thermionic UEM.

With *in situ* electron diffraction, we found a large population of out-of-plane vibrations in both single-crystal and polycrystalline monolayer graphene membranes. While these were static representations of the laser-heated structures, the technique described could be extended to the ps- and ns-time-scales to depict phonon population and relaxation within individual grains and offer insight into interfacial confinement and scattering at the boundaries.

Additional *in situ* studies on the 1T- and 4H$_B$-polytypes of TaS$_2$ provided insight into the nearly-commensurate to incommensurate charge-order transitions and revealed a single-laser-pulse switching effect which we believe to arise from the intense shear-motion in the moments after excitation. The TaS$_2$ case study exemplified some practical

challenges associated with stroboscopic operation in UEM; notably, heat dissipation from the specimen must be considered such that pseudo-steady-state operating temperatures resulting from the laser-pulse-trains are within ranges suitable for a particular experiment. Additionally, dynamics occurring on time-scales comparable to instrument response (such as the ultrafast charge-order melting observed in $TaS_2$) require precise deconvolution for proper interpretation of instrinsic material response. Nonetheless, dark-field imaging on the ultrafast time-scale demonstrated the potential for extraction of non-equilibrium kinetics locally in real-space.

In preliminary efforts to realize a solution for systematic characterization of electron packet properties, we described a method for *in situ* ultrafast electron packet and photon pulse characterization based on interactions between the probing electrons and intense, fleeting evanescent fields at the specimen. Though these strong interactions have deleterious effects on image resolution in the initial moments of excitation (as we have shown), their kinetics are indicative of the instrument response for the given conditions. While this technique has been widely used, our instrument is not equipped with an EELS spectrometer, and as such, an alternative solution was required. Exploiting a plasma-lensing effect described in chapter 2, we systematically mapped the space-charge and temporal instrument-response parameter space as a function of photoelectron-packet population and applied bias. Instrument-response times ranging from 1 to 10 ps (FWHM), for laser-limited single-electron packets to those containing $\sim 10^5$ electrons, were observed; this large range of achievable packet population increases experimental

flexibility and indeed allows UEM experiments to be conducted at relatively low repetition rates (i.e. ~5 kHz).

Imaging discrete propagation of discrete phonon wavefronts was facilitated by contrast arising from small angular perturbations (and as result, local modulation of the Bragg condition) in the lattice associated with elastic deformation. We have discovered that phonon nucleation and launch occurs at discrete spatial locations along individual step-edges, and that the appearance of coherent, propagating wavefronts are extremely sensitive to the shapes of local strain fields and vacuum-crystal interfaces. Drawing additional information from ultrafast selected area diffraction and time-dependent elastic simulations, we have concluded the observed modes arise from interfacial stress caused by initial excitation and confinement of compressional waves along the $WSe_2$ c-axis stacking direction within the specimen-layer bound.

We expect the methodology and insight presented in this work will aid in future quantitative studies of energy transport in crystalline materials with nanostructured interfaces and atomic defects. Ultimately, we envision the direct insight available in UEM will facilitate design of materials and structures for precise control of energy transport and improvement of the numerous applications in which understanding heat transport is critical.

# 9 | References

1.      'Plenty of room' revisited. *Nature nanotechnology* **2009,** *4* (12), 781.

2.      Thompson, S. E.; Parthasarathy, S., Moore's law: the future of Si microelectronics. *Materials Today* **2006,** *9* (6), 20-25.

3.      Curtarolo, S.; Hart, G. L.; Nardelli, M. B.; Mingo, N.; Sanvito, S.; Levy, O., The high-throughput highway to computational materials design. *Nature materials* **2013,** *12* (3), 191-201.

4.      Lu, Z.; Yin, Y., Colloidal nanoparticle clusters: functional materials by design. *Chemical Society reviews* **2012,** *41* (21), 6874-87.

5.      Kroto, H. W.; Heath, J. R.; O'brien, S. C.; Curl, R. R.; Smalley, R. E., C60: Buckminsterfullerence. *Nature* **1985,** *318*, 162-163.

6.      Binnig, G.; Rohrer, H., Scanning Tunneling Microscopy. *Surface Science* **1983,** *126*, 236-244.

7.      Binnig, G.; Quate, C. F.; Gerber, C., Atomic force microscope. *Physical review letters* **1986,** *56* (9), 930-933.

8.      Ludwig, R.; Helmut, K., *Transmission Electron Microscopy: Physics of Image Formation*. 5th ed.; Springer Science + Business Media: New York, 2008; p 590.

9.      Zewail, A. H., 4D ultrafast electron diffraction, crystallography, and microscopy. *Annual review of physical chemistry* **2006,** *57*, 65-103.

10.     Flannigan, D. J.; Zewail, A. H., 4D electron microscopy: principles and applications. *Accounts of chemical research* **2012,** *45* (10), 1828-39.

11.     Plemmons, D. A.; Suri, P. K.; Flannigan, D. J., Probing structural and electronic dynamics with ultrafast electron microscopy. *Chem Mater* **2015,** *27* (9), 3178-3192.

12.     Cahill, D. G.; Ford, W. K.; Goodson, K. E.; Mahan, G. D.; Majumdar, A.; Maris, H. J.; Merlin, R.; Phillpot, S. R., Nanoscale thermal transport. *J. Appl. Phys.* **2003,** *93* (2), 793.

13.     Cahill, D. G.; Braun, P. V.; Chen, G.; Clarke, D. R.; Fan, S.; Goodson, K. E.; Keblinski, P.; King, W. P.; Mahan, G. D.; Majumdar, A.; Maris, H. J.; Phillpot, S. R.; Pop, E.; Shi, L., Nanoscale thermal transport. II. 2003-2012. *Appl. Phys. Rev.* **2014,** *1*, 45.

14.     Pop, E., Energy dissipation and transport in nanoscale devices. *Nano Research* **2010,** *3* (3), 147-169.

15.     Maldovan, M., Sound and heat revolutions in phononics. *Nature* **2013,** *503* (7475), 209-17.

16.     Kippenberg, T. J.; Vahala, K. J., Cavity optomechanics: back-action at the mesoscale. *Science* **2008,** *321* (5893), 1172-6.

17.     Brooks, D. W.; Botter, T.; Schreppler, S.; Purdy, T. P.; Brahms, N.; Stamper-Kurn, D. M., Non-classical light generated by quantum-noise-driven cavity optomechanics. *Nature* **2012,** *488* (7412), 476-80.

18.     Schittny, R.; Kadic, M.; Guenneau, S.; Wegener, M., Experiments on transformation thermodynamics: molding the flow of heat. *Physical review letters* **2013,** *110* (19), 195901.

19.     Zen, N.; Puurtinen, T. A.; Isotalo, T. J.; Chaudhuri, S.; Maasilta, I. J., Engineering thermal conductance using a two-dimensional phononic crystal. *Nature communications* **2014,** *5*, 3435.

20.     Minnich, A. J.; Dresselhaus, M. S.; Ren, Z. F.; Chen, G., Bulk nanostructured thermoelectric materials: current research and future prospects. *Energy & Environmental Science* **2009,** *2* (5), 466.

21.     Barty, A.; Boutet, S.; Bogan, M. J.; Hau-Riege, S.; Marchesini, S.; Sokolowski-Tinten, K.; Stojanovic, N.; Tobey, R. a.; Ehrke, H.; Cavalleri, A.; Düsterer, S.; Frank, M.; Bajt, S.; Woods, B. W.; Seibert, M. M.; Hajdu, J.; Treusch, R.; Chapman, H. N., Ultrafast

Single-Shot Diffraction Imaging of Nanoscale Dynamics. *Nature Photon.* **2008,** *2* (7), 415-419.

22.     Miller, R. J. D., Mapping Atomic Motions with Ultrabright Electrons: The Chemists' Gedanken Experiment Enters the Lab Frame. *Annual Review of Physical Chemistry* **2014,** *65*, 583-604.

23.     Baum, P.; Yang, D.-S.; Zewail, A. H., 4D Visualization of Transitional Structures in Phase Transformations by Electron Diffraction. *Science* **2007,** *318* (5851), 788.

24.     Gao, M.; Lu, C.; Jean-Ruel, H.; Liu, L. C.; Marx, A.; Onda, K.; Koshihara, S. Y.; Nakano, Y.; Shao, X.; Hiramatsu, T.; Saito, G.; Yamochi, H.; Cooney, R. R.; Moriena, G.; Sciaini, G.; Miller, R. J., Mapping molecular motions leading to charge delocalization with ultrabright electrons. *Nature* **2013,** *496* (7445), 343-6.

25.     Fritz, D. M.; Reis, D. A.; Adams, B.; Akre, R. A.; Arthur, J.; Blome, C.; Bucksbaum, P. H.; Cavalieri, A. L.; Engemann, S.; Fahy, S.; Falcone, R. W.; Fuoss, P. H.; Gaffney, K. J.; Georger, M. J.; Hajdu, J.; Hertlein, M. P.; Hillyard, P. B.; Horn-von Hoegen, M.; Kammler, M.; Kaspar, J.; R. Kienberger, R.; Krejcik, P.; Lee, S. H.; Lindenberg, A. M.; McFarland, B.; Meyer, D.; Montagne, T.; Murray, E. D.; Nelson, A. J.; Nicoul, M.; Pahl, R.; Rudati, J.; Schlarb, H.; Siddons, D. P.; Sokolowski-Tinten, K.; Tschentscher, T.; von der Linde, D.; Hastings, J. B., Ultrafast Bond Softening in Bismuth: Mapping a Solid's Interatomic Potential with X-rays. *Science* **2007,** *315*, 3.

26.     Ernstorfer, R.; Harb, M.; Hebeisen, C. T.; Sciaini, G.; Dartigalongue, T.; Miller, R. J. D., The Formation of Warm Dense Matter: Experimental Evidence for Electronic Bond Hardening in Gold. *Science* **2009,** *323*, 4.

27.     Sokolowski-Tinten, K.; Blome, C.; Blums, J.; Cavalleri, A.; Dietrich, C.; Tarasevitch, A.; Uschmann, I.; Forster, E.; Kammler, M.; Horn-von Hoegen, M.; Von der Linde, D., Femtosecond X-ray measurement of coherent lattice vibrations near the Lindemann stability limit. *Nature* **2003,** *422*, 3.

28.     Bargheer, M.; Zhavoronkov, N.; Gritsai, Y.; Woo, J. C.; Kim, D. S.; Woerner, M.; Elsaesser, Coherent Atomic Motions in a Nanostructure Studied by Femtosecond X-ray Diffraction. *Science* **2004,** *306*, 3.

29.     Gahlmann, A.; Park, S. T.; Zewail, A. H., Ultrashort electron pulses for diffraction, crystallography and microscopy: theoretical and experimental resolutions. *Physical chemistry chemical physics : PCCP* **2008,** *10* (20), 2894-909.

30.     Siwick, B. J.; Dwyer, J. R.; Jordan, R. E.; Miller, R. J. D., Ultrafast electron optics: Propagation dynamics of femtosecond electron packets. *Journal of Applied Physics* **2002,** *92* (3), 1643-1648.

31.     Reed, B. W., Femtosecond electron pulse propagation for ultrafast electron diffraction. *Journal of Applied Physics* **2006,** *100* (3), 034916.

32.     Chatelain, R. P.; Morrison, V. R.; Klarenaar, B. L. M.; Siwick, B. J., Coherent and Incoherent Electron-Phonon Coupling in Graphite Observed with Radio-Frequency Compressed Ultrafast Electron Diffraction. *Physical review letters* **2014,** *113* (23), 235502.

33.     Chatelain, R. P.; Morrison, V. R.; Godbout, C.; Siwick, B. J., Ultrafast electron diffraction with radio-frequency compressed electron pulses. *Applied Physics Letters* **2012,** *101* (8), 081901.

34.     Weathersby, S. P.; Brown, G.; Centurion, M.; Chase, T. F.; Coffee, R.; Corbett, J.; Eichner, J. P.; Frisch, J. C.; Fry, A. R.; Guhr, M.; Hartmann, N.; Hast, C.; Hettel, R.; Jobe, R. K.; Jongewaard, E. N.; Lewandowski, J. R.; Li, R. K.; Lindenberg, A. M.; Makasyuk, I.; May, J. E.; McCormick, D.; Nguyen, M. N.; Reid, A. H.; Shen, X.; Sokolowski-Tinten, K.; Vecchione, T.; Vetter, S. L.; Wu, J.; Yang, J.; Dürr, H. A.; Wang, X. J., Mega-electron-volt ultrafast electron diffraction at SLAC National Accelerator Laboratory. *Review of Scientific Instruments* **2015,** *86* (7), 073702.

35.     Zhu, P.; Zhu, Y.; Hidaka, Y.; Wu, L.; Cao, J.; Berger, H.; Geck, J.; Kraus, R.; Pjerov, S.; Shen, Y.; Tobey, R. I.; Hill, J. P.; Wang, X. J., Femtosecond time-resolved MeV electron diffraction. *New Journal of Physics* **2015,** *17* (6), 063004.

36.     Lobastov, V. A.; Srinivasan, R.; Zewail, A. H., Four-dimensional ultrafast electron microscopy. *Proceedings of the National Academy of Sciences of the United States of America* **2005,** *102* (20), 7069-7073.

145

37.     Aidelsburger, M.; Kirchner, F. O.; Krausz, F.; Baum, P., Single-electron pulses for ultrafast diffraction. *Proceedings of the National Academy of Sciences of the United States of America* **2010,** *107* (46), 19714-19719.

38.     Piazza, L.; Masiel, D. J.; LaGrange, T.; Reed, B. W.; Barwick, B.; Carbone, F., Design and implementation of a fs-resolved transmission electron microscope based on thermionic gun technology. *Chemical Physics* **2013,** *423*, 79-84.

39.     Plemmons, D. A.; Park, S. T.; Zewail, A. H.; Flannigan, D. J., Characterization of fast photoelectron packets in weak and strong laser fields in ultrafast electron microscopy. *Ultramicroscopy* **2014,** *146*, 97-102.

40.     Barwick, B.; Park, H. S.; Kwon, O.-H.; Baskin, J. S.; Zewail, A. H., 4D Imaging of Transient Structures and Morphologies in Ultrafast Electron Microscopy. *Science* **2008,** *322*, 1227-1231.

41.     Bücker, K.; Picher, M.; Crégut, O.; LaGrange, T.; Reed, B. W.; Park, S. T.; Masiel, D. J.; Banhart, F., Electron beam dynamics in an ultrafast transmission electron microscope with Wehnelt electrode. *Ultramicroscopy* **2016,** *171*, 8-18.

42.     Valley, D. T.; Ferry, V. E.; Flannigan, D. J., Imaging Intra- and Interparticle Acousto-plasmonic Vibrational Dynamics with Ultrafast Electron Microscopy. *Nano letters* **2016,** *16* (11), 7302-7308.

43.     Cremons, D. R.; Plemmons, D. A.; Flannigan, D. J., Femtosecond electron imaging of defect-modulated phonon dynamics. *Nature communications* **2016,** *7*, 11230.

44.     Kieft, E.; Schliep, K. B.; Suri, P. K.; Flannigan, D. J., Communication: Effects of thermionic-gun parameters on operating modes in ultrafast electron microscopy. *Structural dynamics* **2015,** *2* (5), 051101.

45.     Butler, S. Z.; Hollen, S. M.; Cao, L.; Cui, Y.; Gupta, J. A.; Gutiérrez, H. R.; Heinz, T. F.; Hong, S. S.; Huang, J.; Ismach, A. F.; Johnston-Halperin, E.; Kuno, M.; Plashnitza, V. V.; Robinson, R. D.; Ruoff, R. S.; Salahuddin, S.; Shan, J.; Shi, L.; Spencer, M. G.; Terrones, M.; Windl, W.; Goldberger, J. E., Progress, Challenges, and Opportunities in Two-Dimensional Materials Beyond Graphene. *ACS nano* **2013,** *7* (4), 2898-2926.

46.      Novoselov, K. S.; Jiang, D.; Schedin, F.; Booth, T. J.; Khotkevich, V. V.; Morozov, S. V.; Geim, A. K., Two-dimensional atomic crystals. *Proceedings of the National Academy of Sciences of the United States of America* **2005,** *102* (30), 10451-3.

47.      Nika, D. L.; Askerov, A. S.; Balandin, A. A., Anomalous size dependence of the thermal conductivity of graphene ribbons. *Nano Lett* **2012,** *12* (6), 3238-44.

48.      Chiritescu, C.; Cahill, D. J.; Nguyen, N.; Johnson, D.; Bodapati, A.; Keblinski, P.; Zschack, P., Ultralow Thermal Conductivity in Disordered, Layered WSe$_2$ Crystals. *Science* **2007,** *315*, 3.

49.      Pop, E.; Varshney, V.; Roy, A. K., Thermal properties of graphene: Fundamentals and applications. *MRS Bulletin* **2012,** *37* (12), 1273-1281.

50.      Banhart, F.; Kotakoski, J.; Krasheninnikov, A. V., Structural Defects in Graphene. *ACS nano* **2011,** *5* (1), 26-41.

51.      Hashimoto, A.; Suenaga, K.; Gloter, A.; Uirta, K.; Iijima, S., Direct evidence for atomic defects in graphene layers. *Nature* **2004,** *430*, 870-873.

52.      Huang, P. Y.; Ruiz-Vargas, C. S.; van der Zande, A. M.; Whitney, W. S.; Levendorf, M. P.; Kevek, J. W.; Garg, S.; Alden, J. S.; Hustedt, C. J.; Zhu, Y.; Park, J.; McEuen, P. L.; Muller, D. A., Grains and grain boundaries in single-layer graphene atomic patchwork quilts. *Nature* **2011,** *469* (7330), 389-92.

53.      Kim, K.; Lee, Z.; Regan, W.; Kisielowski, C.; Crommie, M. F.; Zettl, A., Grain Boundary Mapping in Polycrystalline Graphene. *ACS nano* **2011,** *5* (3), 2142-2146.

54.      Ghosh, S.; Calizo, I.; Teweldebrhan, D.; Pokatilov, E. P.; Nika, D. L.; Balandin, A. A.; Bao, W.; Miao, F.; Lau, C. N., Extremely high thermal conductivity of graphene: Prospects for thermal management applications in nanoelectronic circuits. *Applied Physics Letters* **2008,** *92* (15), 151911.

55.      Xin, G.; Sun, H.; Hu, T.; Fard, H. R.; Sun, X.; Koratkar, N.; Borca-Tasciuc, T.; Lian, J., Large-area freestanding graphene paper for superior thermal management. *Advanced materials* **2014,** *26* (26), 4521-6.

56.      Ma, T.; Liu, Z.; Wen, J.; Gao, Y.; Ren, X.; Chen, H.; Jin, C.; Ma, X. L.; Xu, N.; Cheng, H. M.; Ren, W., Tailoring the thermal and electrical transport properties of graphene films by grain size engineering. *Nature communications* **2017,** *8*, 14486.

57.     Lee, W.; Kihm, K. D.; Kim, H. G.; Shin, S.; Lee, C.; Park, J. S.; Cheon, S.; Kwon, O. M.; Lim, G.; Lee, W., In-Plane Thermal Conductivity of Polycrystalline Chemical Vapor Deposition Graphene with Controlled Grain Sizes. *Nano letters* **2017,** *17* (4), 2361-2366.

58.     Mermin, N. D., Crystalline Order in Two Dimensions. *Physical Review* **1968,** *176* (1), 250-254.

59.     Fasolino, A.; Los, J. H.; Katsnelson, M. I., Intrinsic ripples in graphene. *Nature materials* **2007,** *6* (11), 858-61.

60.     Meyer, J. C.; Geim, A. K.; Katsnelson, M. I.; Novoselov, K. S.; Booth, T. J.; Roth, S., The structure of suspended graphene sheets. *Nature* **2007,** *446* (7131), 60-3.

61.     Lindsay, L.; Broido, D. A.; Mingo, N., Flexural phonons and thermal transport in graphene. *Physical Review B* **2010,** *82* (11).

62.     Mariani, E.; von Oppen, F., Flexural phonons in free-standing graphene. *Physical review letters* **2008,** *100* (7), 076801.

63.     Poellmann, C.; Steinleitner, P.; Leierseder, U.; Nagler, P.; Plechinger, G.; Porer, M.; Bratschitsch, R.; Schüller, C.; Korn, T.; Huber, R., Resonant internal quantum transitions and femtosecond radiative decay of excitons in monolayer $WSe_2$. *Nature Materials* **2015,** *14* (9), 889-893.

64.     Zhao, W.; Ghorannevis, Z.; Chu, L.; Toh, M.; Kloc, C.; Tan, P.-H.; Eda, G., Evolution of electronic structure in atomically thin sheets of $WS_2$ and $WSe_2$. *ACS Nano* **2013,** *7* (1), 791-797.

65.     Hao, K.; Moody, G.; Wu, F.; Dass, C. K.; Xu, L.; Chen, C.-H.; Sun, L.; Li, M.-Y.; Li, L.-J.; MacDonald, A. H.; Li, X., Direct measurement of exciton valley coherence in monolayer $WSe_2$. *Nature Physics* **2016,** *12*, 677-682.

66.     Slobodeniuk, A. O.; Basko, D. M., Exciton-phonon relaxation bottleneck and radiative decay of thermal exciton reservoir in two-dimensional materials. *Physical Review B* **2016,** *94* (20), 205423.

67.     Ruppert, C.; Chernikov, A.; Hill, H. M.; Rigosi, A. F.; Heinz, T. F., The role of electronic and phononic excitation in the optical response of monolayer $WS_2$ after ultrafast excitation. *Nano Letters* **2017,** *17* (2), 644-651.

68.     Ludwig, R.; Helmut, K., *Transmission Electron Microscopy: Physics of Image Formation*. Springer: New York, 2008.

69.     Han, T.-R. T.; Zhou, F.; Malliakas, C. D.; Duxbury, P. M.; Mahanti, S. D.; Kanatzidis, M. G.; Ruan, C.-Y., Exploration of metastability and hidden phases in correlated electron crystals visualized by femtosecond optical doping and electron crystallography. *Science Advances* **2015,** *1* (5), e1400173.

70.     Eichberger, M.; Schafer, H.; Krumova, M.; Beyer, M.; Demsar, J.; Berger, H.; Moriena, G.; Sciaini, G.; Miller, R. J. D., Snapshots of cooperative atomic motions in the optical suppression of charge density waves. *Nature* **2010,** *468* (7325), 799-802.

71.     Haupt, K.; Eichberger, M.; Erasmus, N.; Rohwer, A.; Demsar, J.; Rossnagel, K.; Schwoerer, H., Ultrafast Metamorphosis of a Complex Charge-Density Wave. *Physical review letters* **2016,** *116* (1), 016402.

72.     Williams, D. B.; Carter, C. B., *Transmission Electron Microscopy*. Springer: New York, 2009.

73.     Thomas, J. M.; Midgley, P. A., The Modern Electron Microscope: A Cornucopia of Chemico-Physical Insights. *Chem. Phys.* **2011,** *385* (1-3), 1-10.

74.     Bals, S.; Kabius, B.; Haider, M.; Radmilovic, V.; Kisielowski, C., Annular dark field imaging in a TEM. *Solid State Commun.* **2004,** *130* (10), 675-680.

75.     Plemmons, D. A.; Flannigan, D. J., Ultrafast electron microscopy: Instrument response from the single-electron to high bunch-charge regimes. *Chemical Physics Letters* **2017,** *683*, 186-192.

76.     Dresselhaus, M. S.; Jorio, A.; Cancado, L. G.; Dresselhaus, G.; Saito, R., Raman Spectroscopy: Characterization of Edges, Defects, and the Fermi Energy of Graphene and sp2 Carbons. In *Graphene Nanoelectronics*, Raza, H., Ed. Springer-Verlag: Berlin, 2012; p 41.

77.     Ferrari, A. C.; Basko, D. M., Raman spectroscopy as a versatile tool for studying the properties of graphene. *Nature nanotechnology* **2013,** *8*, 12.

78.     Suk, J. W.; Kitt, A.; Magnuson, C. W.; Hao, Y.; Ahmed, S.; An, J.; Swan, A. K.; Goldberg, B. B.; Ruoff, R. S., Transfer of CVD-Grown Monolayer Graphene onto Arbitrary Substrates. *ACS Nano* **2011,** *5* (9), 9.

79.     Lin, Y. C.; Lu, C. C.; Yeh, C. H.; Jin, C.; Suenaga, K.; Chiu, P. W., Graphene annealing: how clean can it be? *Nano Lett* **2012,** *12* (1), 414-9.

80.     Regan, W.; Alem, N.; Alemán, B.; Geng, B.; Girit, Ç.; Maserati, L.; Wang, F.; Crommie, M.; Zettl, A., A direct transfer of layer-area graphene. *Applied Physics Letters* **2010,** *96* (11), 113102.

81.     Meyer, S. F.; Howard, R. E.; Stewart, G. R.; Acrivos, J. V.; Geballe, T. H., Properties of intercalated 2H-NbSe2, 4Hb-TaS2, and 1T-TaS2 *The Journal of Chemical Physics* **1975,** *62* (11), 4411-4419.

82.     Wilson, J. A.; Di Salvo, F. J.; Mahajan, S., Charge-density waves and superlattices in the metallic layered transition metal dichalcogenides. *Advances in Physics* **2010,** *50* (8), 1171-1248.

83.     Park, H.; Hao, Z.; Wang, X.; Nie, S.; Clinite, R.; Cao, J., Synchronization of femtosecond laser and electron pulses with subpicosecond precision. *Review of Scientific Instruments* **2005,** *76* (8), 083905.

84.     Dwyer, J. R.; Hebeisen, C. T.; Ernstorfer, R.; Harb, M.; Deyirmenjian, V. B.; Jordan, R. E.; Miller, R. J. D., Femtosecond electron diffraction: 'making the molecular movie'. *Philosophical transactions. Series A, Mathematical, physical, and engineering sciences* **2006,** *364* (1840), 741-78.

85.     Scoby, C. M.; Li, R. K.; Musumeci, P., Effect of an ultrafast laser induced plasma on a relativistic electron beam to determine temporal overlap in pump-probe experiments. *Ultramicroscopy* **2013,** *127*, 14-18.

86.     Balandin, A. A.; Ghosh, S.; Bao, W.; Calizo, I.; Teweldebrhan, D.; Miao, F.; Lau, C. N., Superior Thermal Conductivity of Single-Layer Graphene. *Nano letters* **2008,** *8* (3), 902-907.

87.     Lee, J.-U.; Yoon, D.; Kim, H.; Lee, S. W.; Cheong, H., Thermal conductivity of suspended pristine graphene measured by Raman spectroscopy. *Physical Review B* **2011,** *83* (8).

88.     Sahoo, S.; Gaur, A. P. S.; Ahmadi, M.; Guinel, M. J. F.; Katiyar, R. S., Temperature-Dependent Raman Studies and Thermal Conductivity of Few-Layer MoS2. *The Journal of Physical Chemistry C* **2013,** *117* (17), 9042-9047.

89.     Luo, Z.; Maassen, J.; Deng, Y.; Du, Y.; Garrelts, R. P.; Lundstrom, M. S.; Ye, P. D.; Xu, X., Anisotropic in-plane thermal conductivity observed in few-layer black phosphorus. *Nature communications* **2015,** *6*, 8572.

90.     Chávez-Ángel, E.; Reparaz, J. S.; Gomis-Bresco, J.; Wagner, M. R.; Cuffe, J.; Graczykowski, B.; Shchepetov, A.; Jiang, H.; Prunnila, M.; Ahopelto, J.; Alzina, F.; Sotomayor Torres, C. M., Reduction of the thermal conductivity in free-standing silicon nano-membranes investigated by non-invasive Raman thermometry. *APL Materials* **2014,** *2* (1), 012113.

91.     Beechem, T.; Yates, L.; Graham, S., Invited Review Article: Error and uncertainty in Raman thermal conductivity measurements. *The Review of scientific instruments* **2015,** *86* (4), 041101.

92.     Bagri, A.; Kim, S. P.; Ruoff, R. S.; Shenoy, V. B., Thermal transport across twin grain boundaries in polycrystalline graphene from nonequilibrium molecular dynamics simulations. *Nano letters* **2011,** *11* (9), 3917-21.

93.     Yasaei, P.; Fathizadeh, A.; Hantehzadeh, R.; Majee, A. K.; El-Ghandour, A.; Estrada, D.; Foster, C.; Aksamija, Z.; Khalili-Araghi, F.; Salehi-Khojin, A., Bimodal Phonon Scattering in Graphene Grain Boundaries. *Nano letters* **2015,** *15* (7), 4532-40.

94.     Shevitski, B.; Mecklenburg, M.; Hubbard, W. A.; White, E. R.; Dawson, B.; Lodge, M. S.; Ishigami, M.; Regan, B. C., Dark-field transmission electron microscopy and the Debye-Waller factor of graphene. *Physical review. B, Condensed matter and materials physics* **2013,** *87*, 045417.

95.     Allen, C. S.; Liberti, E.; Kim, J. S.; Xu, Q.; Fan, Y.; He, K.; Robertson, A. W.; Zandbergen, H. W.; Warner, J. H.; Kirkland, A. I., Temperature dependence of atomic vibrations in mono-layer graphene. *Journal of Applied Physics* **2015,** *118* (7), 074302.

96.     Hu, J.; Vanacore, G. M.; Cepellotti, A.; Marzari, N.; Zewail, A. H., Rippling ultrafast dynamics of suspended 2D monolayers, graphene. *Proceedings of the National Academy of Sciences of the United States of America* **2016,** *113* (43), E6555-E6561.

97.     Sipos, B.; Kusmartseva, A. F.; Akrap, A.; Berger, H.; Forro, L.; Tutis, E., From Mott state to superconductivity in-1T-TaS2. *Nature materials* **2008,** *7*, 906-909.

98.     Benedek, G.; Brusdeylins, G.; Hofmann, F.; Ruggerone, P.; Toennies, J. P.; Vollmer, R.; Skofronick, J. G., Strong coupling of Rayleigh phonons to charge density waves in 1T-TaS$_2$. *Surf Sci* **1994,** *304* (1-2), 185-190.

99.     Haupt, K.; Eichberger, M.; Erasmus, N.; Rohwer, A.; Demsar, J.; Rossnagel, K.; Schwoerer, H., Ultrafast Metamorphosis of a Complex Charge-Density Wave. *Physical review letters* **2016,** *116* (1), 016402.

100.    Morrison, V. R.; Chatelain, R. P.; Godbout, C.; Siwick, B. J., Direct Optical Measurements of the Evolving Spatio-Temporal Charge Density in Ultrashort Electron Pulses. *Opt. Express* **2013,** *21*, 21-29.

101.    Han, T.-R. T.; Tao, Z.; Mahanti, S. D.; Chang, K.; Ruan, C.-Y.; Malliakas, C. D.; Kanatzidis, M. G., Structural dynamics of two-dimensional charge-density waves in CeTe3investigated by ultrafast electron crystallography. *Physical Review B* **2012,** *86* (7).

102.    Van Landuyt, J.; Van Tendeloo, G.; Amelinckx, S., Electron Diffraction Study of Inter- and Intrapolytypic Phase Transitions in Transition Metal Dichalcogenids. *phys. stat. sol. (a)* **1974,** *26*, 585-592.

103.    Yurtsever, A.; Baskin, J. S.; Zewail, A. H., Entangled Nanoparticles: Discovery by Visualization in 4D Electron Microscopy. *Nano Lett.* **2012,** *12* (9), 5027-5032.

104.    Haes, A. J.; Haynes, C. L.; McFarland, A. D.; Schatz, G. C.; Van Duyne, R. R.; Zou, S. L., Plasmonic Materials for Surface-Enhanced Sensing and Spectroscopy. *MRS Bull.* **2005,** *30* (5), 368-375.

105.    Park, S. T.; Yurtsever, A.; Baskin, J. S.; Zewail, A. H., Graphene-Layered Steps and Their Fields Visualized by 4D Electron Microscopy. *Proc. Natl. Acad. Sci. U. S. A.* **2013,** *110* (23), 9277-9282.

106.    Barwick, B.; Flannigan, D. J.; Zewail, A. H., Photon-induced near-field electron microscopy. *Nature* **2009,** *462* (7275), 902-906.

107.    Park, S. T.; Lin, M.; Zewail, A. H., Photon-Induced Near-Field Electron Microscopy (PINEM): Theoretical and Experimental. *New Journal of Physics* **2010,** *12* (12), 123028.

108.    García de Abajo, F. J.; Asenjo-Garcia, A.; Kociak, M., Multiphoton Absorption and Emission by Interaction of Swift Electrons with Evanescent Light Fields. *Nano letters* **2010,** *10* (5), 1859-1863.

109.    Park, S. T.; Zewail, A. H., Relativistic Effects in Photon-Induced Near Field Electron Microscopy. *J. Phys. Chem. A* **2012,** *116* (46), 11128-11133.

110.    Yurtsever, A.; van der Veen, R. M.; Zewail, A. H., Subparticle Ultrafast Spectrum Imaging in 4D Electron Microscopy. *Science* **2012,** *335* (6064), 59-64.

111.    Flannigan, D. J.; Barwick, B.; Zewail, A. H., Biological imaging with 4D ultrafast electron microscopy. *Proc Natl Acad Sci U S A* **2010,** *107* (22), 9933-7.

112.    Park, S. T.; Kwon, O.-H.; Zewail, A. H., Chirped Imaging Pulses in Four-Dimensional Electron Microscopy: Femtosecond Pulsed Hole Burning. *New J. Phys.* **2012,** *14* (5), 053046.

113.    Kirchner, F. O.; Gliserin, A.; Krausz, F.; Baum, P., Laser Streaking of Free Electrons at 25 keV. *Nature Photon.* **2013,** *8*, 52-57.

114.    Barwick, B.; Zewail, A. H., Photonics and Plasmonics in 4D Ultrafast Electron Microscopy. *ACS Photonics* **2015,** *2*, 1391-1402.

115.    Feist, A.; Echternkamp, K. E.; Schauss, J.; Yalunin, S. V.; Schäfer, S.; Ropers, C., Quantum coherent optical phase modulation in an ultrafast transmission electron microscope. *Nature* **2015,** *521* (7551), 200-203.

116.    Piazza, L.; Lummen, T. T.; Quinonez, E.; Murooka, Y.; Reed, B. W.; Barwick, B.; Carbone, F., Simultaneous observation of the quantization and the interference pattern of a plasmonic near-field. *Nature communications* **2015,** *6*, 6407.

117.    Gao, M.; Jean-Ruel, H.; Coooney, R. R.; Stampe, J.; de Jong, M.; Harb, M.; Sciaini, G.; Moriena, G.; Miller, R. J. D., Full characterization of RF compressed femtosecond electron pulses using ponderomotive scattering. *Optics Express* **2012,** *20* (11), 10.

118.    Li, R. K.; Musumeci, P., Single-Shot MeV Transmission Electron Microscopy with Picosecond Temporal Resolution. *Phys. Rev. Appl.* **2014,** *2* (2), 024003.

119.    Gliserin, A.; Walbran, M.; Krausz, F.; Baum, P., Sub-phonon-period compression of electron pulses for atomic diffraction. *Nat Commun* **2015,** *6*, 8723.

120.    Chatelain, R. P.; Morrison, V.; Godbout, C.; van der Geer, B.; de Loos, M.; Siwick, B. J., Space-Charge Effects in Ultrafast Electron Diffraction Patterns from Single Crystals. *Ultramicroscopy* **2012,** *116*, 86-94.

121.    Pasmans, P. L. E. M.; van Vugt, D. C.; van Lieshout, J. P.; Brussaard, G. J. H.; Luiten, O. J., Extreme regimes of femtosecond photoemission from a copper cathode in a dc electron gun. *Physical Review Accelerators and Beams* **2016,** *19* (10), 103403.

122.    Yurtsever, A.; Zewail, A. H., Kikuchi ultrafast nanodiffraction in four-dimensional electron microscopy. *Proceedings of the National Academy of Sciences* **2011,** *108* (8), 3152-3156.

123.    Yurtsever, A.; Schaefer, S.; Zewail, A. H., Ultrafast Kikuchi diffraction: nanoscale stress-strain dynamics of wave-guiding structures. *Nano letters* **2012,** *12* (7), 3772-7.

124.    Barwick, B.; Park, H. S.; Kwon, O.-H.; Baskin, J. S.; Zewail, A. H., 4D Imaging of Transient Structures and Morphologies in Ultrafast Electron Microscopy. *Science* **2008,** *322*, 5.

125.    Kwon, O.-H.; Barwick, B.; Park, H. S.; Baskin, J. S.; Zewail, A. H., Nanoscale Mechanical Drumming Visualized by 4D Electron Microscopy. *Nano letters* **2008,** *8* (11), 3557-3562.

126.    Park, H. S.; Baskin, J. S.; Barwick, B.; Kwon, O. H.; Zewail, A. H., 4D ultrafast electron microscopy: Imaging of atomic motions, acoustic resonances, and moiré fringe dynamics. *Ultramicroscopy* **2009,** *110* (1), 7-19.

127.    Cuffe, J.; Chavez, E.; Shchepetov, A.; Chapuis, P. O.; El Boudouti el, H.; Alzina, F.; Kehoe, T.; Gomis-Bresco, J.; Dudek, D.; Pennec, Y.; Djafari-Rouhani, B.; Prunnila, M.; Ahopelto, J.; Sotomayor Torres, C. M., Phonons in slow motion: dispersion relations in ultrathin Si membranes. *Nano letters* **2012,** *12* (7), 3569-73.

128.    Seol, J. H.; Jo, I.; Moore, A. L.; Lindsay, L.; Aitken, Z. H.; Pettes, M. T.; Li, X.; Yao, Z.; Huang, R.; Broido, D.; Mingo, N.; Ruoff, R. S.; Shi, L., Two-dimensional phonon transport in supported graphene. *Science* **2010,** *328* (5975), 213-6.

129.    Seol, J. H.; Jo, I.; Moore, A. L.; Lindsay, L.; Aitken, Z. H.; Pettes, M. T.; Li, X.; Yao, Z.; Huang, R.; Broido, D.; Mingo, N.; Ruoff, R. S.; Shi, L., Two-Dimensional Phonon Transport in Supported Graphene. *Science* **2010,** *328*, 4.

130.    Frindt, R. F., The optical properties of single crystals of $WSe_2$ and $MoTe_2$. *Journal of Physics and Chemistry of Solids* **1963,** *24* (9), 1107-1108.

131.    Upadhyayula, L. C.; Loferski, J. J.; Wold, A.; Giriat, W.; Kershaw, R., Semiconducting properties of single crystals of *n*- and *p*-type tungsten diselenide ($WSe_2$). *Journal of Applied Physics* **1968,** *39* (10), 4736-4740.

132.    Kubo, A.; Onda, K.; Petek, H.; Sun, Z. J.; Jung, Y. S.; Kim, H. K., Femtosecond imaging of surface plasmon dynamics in a nanostructured silver film. *Nano Lett.* **2005,** *5* (6), 1123-1127.

133.    Meyer zu Heringdorf, F.-J.; Chelaru, L. I.; Möllenbeck, S.; Thien, D.; Horn-von Hoegen, M., Femtosecond photoemission microscopy. *Surf. Sci.* **2007,** *601* (20), 4700-4705.

134.    Baugher, B. W. H.; Churchill, H. O. H.; Yang, Y.; Jarillo-Herrero, P., Optoelectronic devices based on electrically tunable p-n diodes in a monolayer dichalcogenide. *Nature Nanotechnology* **2014,** *9* (4), 262-267.

135.    Ross, J. S.; Klement, P.; Jones, A. M.; Ghimire, N. J.; Yan, J.; Mandrus, D. G.; Taniguchi, T.; Watanabe, K.; Kitamura, K.; Yao, W.; Cobden, D. H.; Xu, X., Electrically tunable excitonic light-emitting diodes based on monolayer $WSe_2$ p-n junctions. *Nature Nanotechnology* **2014,** *9* (4), 268-272.

136.    Fang, H.; Chuang, S.; Chang, T. C.; Takei, K.; Takahashi, T.; Javey, A., High-performance single layered $WSe_2$ p-FETs with chemically doped contacts. *Nano Letters* **2012,** *12* (7), 3788-3792.

137.    Hjelmstad, K. D., *Fundamentals of Structural Mechanics*. 2 ed.; Springer: New York, 2005.

138.    Zhao, Y.; Luo, X.; Li, H.; Zhang, J.; Araujo, P. T.; Gan, C. K.; Wu, J.; Zhang, H.; Quek, S. Y.; Dresselhaus, M. S.; Xiong, Q., Interlayer breathing and shear modes in few-trilayer MoS2 and WSe2. *Nano letters* **2013,** *13* (3), 1007-15.

139.    Yip, S.; Short, M. P., Multiscale materials modelling at the mesoscale. *Nature Materials* **2013,** *12* (9), 774-777.

140.    Miller, R. E.; Tadmor, E. B., A unified framework and performance benchmark of fourteen multiscale atomistic/continuum coupling methods. *Model. Simul. Mater. Sci. Eng.* **2009,** *17* (5), 053001.

# Appendix A | List of Publications and Presentations

## *Publications*

9.      Cremons, D. R.; Plemmons, D. A.; Flannigan, D. J. Defect-Mediated Phonon Dynamics in TaS2 and WSe2. *Struct. Dyn.* 2017, **4**, 044019. (Special issue: Ultrafast Structural Dynamics – A Tribute to Ahmed. H. Zewail, Invited)

8.      Plemmons, D. A.; Flannigan, D. J. Ultrafast Electron Microscopy: Instrument Response from the Single-Electron to High Bunch-Charge Regimes. *Chem. Phys. Lett.* 2017, **683**, 186-192. (Special issue: Ahmed Zewail (1946-2016) Commemoration Issue of Chemical Physics Letters, Invited)

7.      Plemmons, D. A.; Flannigan, D. J. Discrete Chromatic Aberrations Arising from Photoinduced Electron-Photon Interactions in Ultrafast Electron Microscopy. J. Phys. Chem. A 2016, 120, 3539-3546.

6.      Cremons, D. R.; Plemmons, D. A.; Flannigan, D. J. Morphological Modulation of Acoustic Phonons Imaged with Ultrafast Electron Microscopy. *Microsc. Microanal.* 2016, **22** (Suppl. 3), 1632-1633.

5.      Cremons, D. R.; Plemmons, D. A.; Flannigan, D. J. Femtosecond Electron Imaging of Defect-Modulated Phonon Dynamics. *Nature Commun.* 2016, **7**, 11230.

4.      Plemmons, D. A.; McKenna, A. J.; Flannigan, D. J. Effects of Quantized, Transient Chromatic Aberrations in Ultrafast Electron Microscopy. *Microsc. Microanal.* 2015, **21** (Suppl. 3), 805-806.

3.      Plemmons, D. A.; Suri, P. K.; Flannigan, D. J. Probing Structural and Electronic Dynamics with Ultrafast Electron Microscopy. *Chem. Mater.* 2015, **27**, 3178-3192. (Invited Up-and-Coming Series Perspective)

2.      Plemmons, D. A.; Park, S. T.; Zewail, A. H.; Flannigan, D. J. Characterization of Fast Photoelectron Packets in Weak and Strong Laser Fields in Ultrafast Electron Microscopy. *Ultramicroscopy* 2014, **146**, 97-102.

1.      Plemmons, D. A.; Flannigan, D. J. Practical Considerations for Ultrashort Electron Pulse Characterization in Ultrafast Transmission Electron Microscopy. *Microsc. Microanal.* 2014, **20**, (Suppl. 3), 1588-1589.

## *Presentations*

### 2017

13. Flannigan, D. J.; Cremons, D. R.; McKenna, A. J.; <u>Plemmons, D. A.</u>; Valley, D. T. "Coherent Photoexcited Structural Dynamics in Nanostructured and Nanoscale Materials" Electron Microscopy at High Temporal Resolution, Strasbourg, FR, May 29-June 1, 2017. (*Invited*)

### 2016

12. <u>Plemmons, D. A.</u>; Flannigan, D. J. "Femtosecond Electron Imaging and Diffraction of Few-GHz Phonon Dynamics in Layered Nanostructures" Advances in Spatial, Energy and Time Resolution in Electron Microscopy, MRS Fall Meeting, Boston, MA, November 27-December 2, 2016. (*poster*) (*Best Poster Award*)

11. <u>Cremons, D. R.</u>; Plemmons, D. A.; Flannigan, D. J. "Morphological Modulation of Acoustic Phonons Imaged with Ultrafast Electron Microscopy" Microscopy and Microanalysis Meeting, Columbus, OH, July 24-28, 2016. (*poster*)

10. <u>Plemmons, D. A.</u>; Flannigan, D. J. "Observing Energy Transport on the Nanoscale with Ultrafast Transmission Electron Microscopy" University of Minnesota Doctoral Research Showcase, Minneapolis, MN, April 5, 2016. (*poster*) (*Invited*)

9. <u>Plemmons, D. A.</u>; Flannigan, D. J. "Imaging Acoustic Phonon Dynamics on the Nanometer-Femtosecond Spatiotemporal Length-Scale with Ultrafast Electron Microscopy" 2016 APS March Meeting, Baltimore, MD, March 14-18, 2016.

### 2015

8. <u>Flannigan, D. J.</u>; Plemmons, D. A.; Cremons, D. R.; Valley, D. T. "Quantized Chromatic Aberrations and Temporal Resolutions in Ultrafast Electron Microscopy" Chemical Imaging: Frontiers of Spatio-Temporal Resolution, International Chemical Congress of Pacific Basin Societies (Pacifichem), Honolulu, HI, December 15-20, 2015.

7. <u>Plemmons, D. A.</u>; Flannigan, D. J. "Thermal Transport and Atomic Vibrations in Suspended Polycrystalline Graphene Membranes" 2015 MRS Fall Meeting, Boston, MA, November 29-December 4, 2015.

6. <u>Plemmons, D. A.</u>; McKenna, A. J.; Flannigan, D. J. "Effects of Quantized Chromatic Aberrations in Ultrafast Electron Microscopy" Microscopy and Microanalysis Meeting, Portland, OR, August 2-6, 2015. (*poster*)

### 2014

5. <u>Plemmons, D. A.</u>; Flannigan, D. J. "Semi-Direct Transfer of CVD Graphene for *In Situ* Transmission Electron Microscopy Thermal Transport Experiments" 4th International Symposium on Graphene Devices, Bellevue, WA, September 21-25, 2014.

4. Flannigan, D. J.; Plemmons, D. A. "Electron Pulse Properties and PINEM Aberrations in Ultrafast Transmission Electron Microscopy" 18th International Microscopy Congress, Prague, Czech Republic, September 7-12, 2014. (*Invited*)

3. Plemmons, D. A.; Flannigan, D. J. "Practical Considerations for Ultrashort Electron Pulse Characterization in Ultrafast Transmission Electron Microscopy" Microscopy and Microanalysis, Hartford, CT, August 3-7, 2014.

2. Plemmons, D. A.; Flannigan, D. J. "Prospects for Investigation of 2D Energy Transport via Ultrafast Transmission Electron Microscopy" Microscopy Across the Disciplines, University of St. Thomas, St. Paul, MN, January 16, 2014. (*poster*)

**2013**

1. Plemmons, D. A.; Holzman, N.; Flannigan, D. J. "Characterization of Transfer Artifacts of CVD-Grown Graphene Using Correlative Optical, Confocal Raman, and Transmission Electron Microscopy" MNAVS Annual Symposium, St. Paul, MN, September 19, 2013. (*poster*)

# Appendix B | Detailed Methods for *In Situ* and Correlative Graphene Studies

*Preparation of suspended graphene membranes*

Monolayer graphene grown by CVD on copper (Graphene Supermarket) was transferred by a previously described polymer scaffold technique to silicon TEM frames with a 0.5 mm by 0.5 mm window covered by a 200 nm holey silicon nitride film with holes 2.5 um in diameter (Ted Pella). An optical microscope with a 20x dark-field objective lens was used to both determine coverage of the film and find features on the support film to correlate with low magnification TEM images such that the SAED grain structure characterization is performed on the associated membranes examined by confocal Raman microscopy.

*Opto-thermal Raman measurements of thermal conductivity*

A Witec alpha300R confocal Raman microscope with a 514.5 nm excitation source (Omnichrome Argon ion laser) was used in characterization of graphene films and measurement of their thermal conductivity. Areas of pristine monolayer graphene free of wrinkles, polymer and copper contaminates, and bi-/tri-layer islands were identified by performing coarse, wide-area scans to find large regions with appropriate $I_{2D}/I_G$ ratios and free of surface contamination peaks. Thermal conductivity measurements of membranes is performed by acquiring spectra for 0.4 seconds in a 30 pixel by 30 pixel grid with the specimen rastered across a 12 μm by 12 μm region for six different laser powers. Spectra taken from the center of each membrane are then fit to a pseudo-Voigt function to determine the center of each G-peak, $\omega_G$, and its intensity. The intensity of each peak is

correlated with calibration measurements to determine the laser power incident on the specimen, and the slope of the $\omega_G$ versus laser power is used to estimate thermal conductivity via Eq. 1. The error bars represent error propagated from the standard error of the slopes in linear fitting of $\omega_G$ vs $P$.

*Grain size determination*

Membranes examined in the Raman technique were carefully identified in a 120kV transmission electron microscope (FEI Tecnai T12) by comparing features observed in the TEM with reference features from optical micrographs. SAED patterns were acquired at 350mm camera-length with the beam illuminating precisely the suspended membrane. Azimuthal integration was performed over a 10 pixel annulus centered at the radius of the (110) reflection and orientation angle plots were generated by averaging four of the six equivalent 60 degree sections. Orientation angle peaks (and shoulders for peaks closely bordering each other) with intensity over twice the noise-limit were fit to a 2D pseudo-Voigt function, and the geometric mean of the normalized intensities (that is, the intensity of a single-peak normalized to the summation of the intensities of all peaks) was used to determine an average grain area via multiplication by the total membrane area. The characteristic grain size is the square root of this area.

*In-situ SAED of laser-heated membranes*

*In-situ* laser heating of graphene membranes was performed in a 200kV TEM (FEI Tecnai Femto) equipped with an optical periscope directing external laser light to the specimen region. Pulse trains of 515 nm laser light, the second harmonic of a

Yb:KGW 1030 nm (1.2 eV) fundamental laser (Light Conversion), are used to excite the specimen, and the power is attenuated to 24 mW, 18 mW, and 14 mW by pulse-picking from 600kHz to 200 kHz, 150 kHz, and 120 kHz, respectively. The laser beam-width at the specimen is ~120 μm FWHM as measured ex-situ with a beam profiler. Automated acquisition of SAED patterns takes place at 120 mm camera length with 10 second acquisitions occuring every 22 seconds on a 2048 pixel by 2048 pixel CCD with 16-bit digitization (Gatan Orius Sc200B). A shutter is systematically opened and closed at specified intervals to allow laser light to reach the specimen. During the first shutter-open interval, the laser power is set at ~14 mW via pulse-picking, and the power is increased to 18 mW and then 24 mW in the subsequent shutter-open intervals. For each interval, a pseudo-steady-state is reached within the first two acquisitions.

*Extraction of the Debye-Waller Factor for single-crystal membranes*

For the single-crystal membranes approximately 50 peaks are extracted out to tenth-order [i.e. the (410) reflection], and each peak is fit individually to a 2D pseudo-Voigt function with 7 free-parameters: a Lorentizian and Gaussian amplitude, two center coordinates, two orthoganal widths, and an angle describing the rotation of width axes with respect to the diffraction axes. We take the intensities as the sum of the Lorentzian and Gaussian amplitudes, and these values are used in fitting to Eq. 2 to obtain the non-excited DWF and in calculations of elastic scattering suppression. In determining the non-excited DWF, we average the intensities of each peak over 5 DPs acquired with the laser off, apply appropriate normalization of "strong" peaks according to the structure factor (that is, divide the intensity of the $2^{nd}$, $5^{th}$, $6^{th}$, and $10^{th}$ order peaks by 4), and fit to

Eq. 2 with log-scale weighting. The reported uncertainty is the standard deviation of measurements on three different membranes. To measure intensity suppression upon laser excitation, equivalent peaks in every diffraction pattern are averaged and normalized to the median laser-off intensity for the given reflection. The suppression ratio, $I/I_0$, used in Debye-Waller calculations is taken as the median of the laser-on values for a given excitation power. Unless otherwise noted, error-bars for $\Delta<U^2>$ represent the standard error in the slope in linear fitting of $-LN(I/I_0)$ vs. $G^2$.

*Extraction of the Debye-Waller Factor for polycrystalline membranes and within individual grains*

Intensities at radii corresponding to the first six reflections in polycrystalline membranes were evaluated by azimuthal integration over 300 degrees (such that the region affected by the beam block is excluded). The background of each azimuthal trace is estimated by a $4^{th}$-order polynomial minimizing an asymmetric truncated quadratic cost function, and the sum of the background-subtracted azimuthal traces are normalized to the median of laser-off values. Again, the appropriate suppression ratio, $I/I_0$, used in Debye-Waller calculations is taken as the median of the laser-on values for a given excitation power.

For single-grain calculations, specific angles in the background-subtracted azimuthal traces corresponding to individual grains are analyzed separately. The intensity of the $1^{st}$, $2^{nd}$, $5^{th}$ and $6^{th}$ order reflections are extracted by summing 8 pixels surrounding a peak maximum, and the intensities traces of the $5^{th}$ and $6^{th}$ order peaks normalized to

the $1^{st}$ and $2^{nd}$ order peaks are used to extract $\Delta<U^2>$ by Eq. 5. In this case, the error bars represent the standard deviation of 4 calculations of $\Delta<U^2>$ with $j = 5$, 6 and $i = 1$, 2.

# Appendix C | Derivations and Additional PINEM Calculations

***Derivation of the Weak-Interaction Limit*** – In ultrafast electron microscopy (UEM), a probing electron passing through a scattered near-field generated by a femtosecond laser pulse can gain and lose *n* quanta of the incident photon energy in a process known as the photon-induced near-field (PINEM) effect [C1]. A detailed derivation of the transition probability for a PINEM event was given in Ref. [C2]. The temporal filter aspect of PINEM was given in Ref. [C3] and utilized in Ref. [C4] to characterize the temporal spread and energy-time correlation of the electron pulse. Note, however, that only first-order transitions were considered therein. Below, we describe how higher-order transitions may be used to determine both optical and electron pulse durations *in situ.*

The probability (spatial) density of an electron propagating in the z-direction, $P_e(z')$, on a moving frame, $z' = z - v_e t$, was chosen to be the normalized Gaussian function (Eq. S1).

$$P_e(z') = \left( \frac{1}{\sqrt{2\pi}\Delta_e v_e} exp \left[ \frac{-\left(\frac{z'}{v_e}\right)^2}{2\sigma_e^2} \right] \right) \qquad (C1)$$

Equation S1 represents a pulsed electron packet with temporal width $\sigma_e$ traveling at $v_e$, the electron velocity. The (temporal) intensity of incident light at the particle position is given by Equation C2.

$$I_p(t) = I_0 exp \left[ \frac{-(-t-\tau)^2}{2\sigma_p^2} \right] \qquad (C2)$$

165

Here, $\sigma_p$ is the photon duration, and $\tau$ is the delay between the electron and photon pulses. After interaction with the scattered light, the resulting electron density of the $n^{th}$ virtual-state is given by Equation C3.

$$P_n(z') = P_e(z')Q_n(z';\tau) \quad \text{(C3)}$$

Here, $Q_n(z';\tau)$ is the transition probability described in Ref. 2 and given by Equation S4.

$$\boldsymbol{Q_n(t)} = \left| \boldsymbol{J_n} \left\{ \frac{-e|\tilde{F}_0|}{\hbar\omega_p} \boldsymbol{I_p(t)^{\frac{1}{2}}} \right\} \right|^2 \quad \text{(C4)}$$

Here, $-e$ is the electron charge, $\hbar\omega_p$ the photon energy, and $J_n$ a Bessel function of the first kind. The exponential term describes overlap of the electron packet with the incident light at the specimen position in a slowly-varying envelope approximation. The $|\tilde{F}_0|$ term is the amplitude of scattered light with spatial frequency $k = \dfrac{\omega_p}{v_e}$. As the electric field of a scattered wave is proportional to the magnitude of the electric field of the incident light, $\tilde{E}_0$, we can separate the intensity dependence of the $|\tilde{F}_0|$ term (Eq. C5).

$$|\tilde{F}_0| = |\tilde{E}_0\tilde{L}| = \sqrt{\frac{2I_0}{c\varepsilon_0}}|\tilde{L}| \quad \text{(C5)}$$

Here, $\tilde{L}$ is determined by the geometry of the particle and the dielectric constant of the material, as well as the polarization, wavelength, and phase of the incident light.

While for large arguments the Bessel function in the transition probability must be explicitly evaluated, for small arguments (i.e., the weak-interaction limit) it may be

approximated as the first term in the series expansion, $J_n\left(\Omega^{\frac{1}{2}}\right)^2 \approx \frac{1}{n!}\left(\frac{\Omega}{2}\right)^n$ **for** $\Omega^{\frac{1}{2}} \ll$

$\sqrt{n+1}$, and Equation S4 reduces to

$$Q_n(z';\tau) = \frac{1}{n!^2}\left\{\left(\frac{-e|\tilde{F}_0|}{\hbar\omega_p}\right)^2 exp\left[\frac{-\left(\frac{z'}{v_e}-\tau\right)^2}{2\sigma_p^2}\right]\right\}^n \quad \text{for} \quad \frac{-e|\tilde{F}_0|}{\hbar\omega_p} \ll \sqrt{n+1} \quad (C6)$$

Upon insertion of Equation S5 and grouping of constants, Equation C6 can be further reduced to Equation S7.

$$Q_n(z';\tau) = \frac{1}{n!^2}\left\{W_0 I_0 exp\left[\frac{-\left(\frac{z'}{v_e}-\tau\right)^2}{2\sigma_p^2}\right]\right\}^n = \frac{W_0^n}{n!^2}\left\{I_p\left(-\frac{z'}{v_e}\right)\right\}^n \quad (C7)$$

Here, $W_o = \frac{2}{c\epsilon_o}\left(\frac{e|\tilde{L}|}{2\hbar\omega_p}\right)^2$. From Equation C7 it can be seen that the temporal profile of the incident light is explicitly present in the transition probability and that an $n^{th}$-order transition will experience an effective optical pulse length of $\frac{\sigma_p}{\sqrt{n}}$; namely, the higher the order of the transition, the shorter pulse length.

The $n^{th}$-order virtual state populations, or the electron energy-gain spectrum (EEGS), at time delay $\tau$ can then be obtained by integration of Equation S3 over the entire electron packet (Eq. C8).

$$P(n;\tau) = \int_{-\infty}^{+\infty} dz' P_e(z') Q_n(z';\tau) = \frac{W_0^n}{n!^2}\left[P_e(z')\otimes\left\{I_p\left(-\frac{z'}{v_e}\right)\right\}^n\right](-\tau) \quad (C8)$$

It can be seen in Equation (C8) that the temporal dependence of each virtual state is proportional to the cross-correlation of the two Gaussian functions representing the

electron packet and the effective optical pulse experienced by the electron for transitions of order $n$. The width of this cross-correlation is then given by Equation C9.

$$\sigma_n = \sqrt{\sigma_e^2 + \frac{\sigma_p^2}{n}} \quad \text{(C9)}$$

From Equation S9, the electron packet duration can be determined for a known photon pulse width, or both the electron packet and photon pulse durations can be determined independently by analyzing all orders via linear regression of $\sigma_n^2$ vs. $\frac{1}{n}$.

*Peak Broadening Magnitude* −The origin of peak broadening lies in the non-linear photon-pulse intensity dependence of PINEM transitions. The peaks deviate from Gaussian shape at higher fluence as they are depleted non-uniformly (within the next effective optical pulse range) in favor of the adjacent peaks. Broadening of the ZLP temporal cross-section occurs when it is repopulated due to electrons that have absorbed and emitted an equal number of photons; for $n$ PINEM events, where $n$ is an even integer, the ZLP cross-section is repopulated only within the effective optical pulse range $\frac{\sigma_p}{\sqrt{n}}$. The relative magnitude of broadening of the observed temporal width of the ZLP cross-section $\sigma_0^{observed}$ with respect to the cross-correlation width $\left(\sigma_0 = \sqrt{\sigma_e + \sigma_p}\right)$ depends only on the ratio between pulse durations $\frac{\sigma_e}{\sigma_p}$ and the interaction parameter, $\Omega$. Figure S1 illustrates the dependence of the broadening percentage $\left(\frac{\sigma_0^{observed}}{\sigma_0} \times 100\right)$ on the pulse duration ratio and interaction strength. It can be seen that broadening is largest for pulse durations of equal magnitude. Although this case is seldom observed − electron packet

durations are typically significantly larger than photon durations due to energy-time uncertainty during emission and broadening during propagation – new pulse compression techniques are being developed to reach this regime.
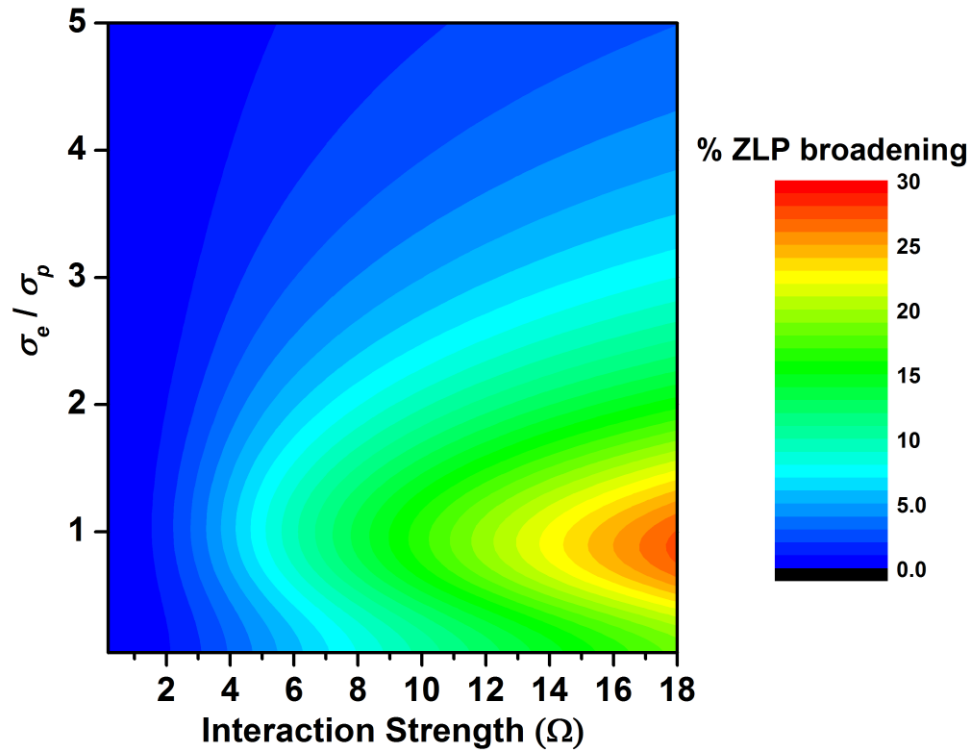


**Fig. C1.** ZLP temporal cross-section broadening. Maximum broadening occurs for photon pulse durations that are comparable to the electron packet duration. This is attributed to the greater number of PINEM events that occur for longer-duration and higher-intensity photon pulses.

***Simulation of EELS/EEGS Plots*** – Population of $n^{th}$-order PINEM peaks were calculated from the quantum-mechanical treatment of swift electrons in an evanescent

near-field [C2]. For a focused electron beam (fixed impact parameter), population of an $n^{\text{th}}$-order peak is given by Equation C10.

$$P(n) = \sum_{j=0}^{\infty} \sum_{k=0}^{\infty} C_j^n C_k^{n*} \left(1 + S_{njk} R_\sigma^2\right)^{-1/2} exp\left[-\frac{S_{njk} R_\tau^2}{2\left(1 + S_{njk} R_\sigma^2\right)}\right]$$

$$where \quad C_j^n = \frac{1}{(|n|+j)!j!} \left(\frac{\Omega}{2}\right)^{n+j} \left(\frac{-\Omega}{2}\right)^{j} \qquad (C10)$$

Here, $S_{njk} = n + j + k$, $R_\sigma = \sigma_e/\sigma_p$, and $R_\tau = \tau/\sigma_p$. Because the interaction strength, $\Omega$, varies in space, the resulting PINEM populations for parallel beam illumination must be determined from spatial integration over the entire electron beam spot. For the simulations presented here, a spherical nanostructure has been considered such that the interaction strength decays exponentially away from the sphere (Eq. C11).

$$\Omega(r, \phi) = \Omega(a, 0) exp\left[\frac{-(r-a)}{\delta}\right] \cos\phi \qquad (C11)$$

Here, $a$ is the radius of the sphere, $\delta$ is an empirical decay length, $r$ is the radial position, and $\phi$ is the azimuthal angle. Integrating over the beam waist ($w$) yields the relation used for $n^{\text{th}}$-order PINEM populations (Eq. C12).

$$P(n) = \sum_{j=0}^{\infty} \sum_{k=0}^{\infty} D_{jk}^n C_j^n C_k^{n*} \left(1 + S_{njk} R_\sigma^2\right)^{-1/2} exp\left[-\frac{S_{njk} R_\tau^2}{2\left(1 + S_{njk} R_\sigma^2\right)}\right]$$

$$where \quad D_{jk}^n = \frac{\delta\left\{(2S_{njk}a+\delta) - exp\left[\frac{-2S_{njk}(w-a)}{\delta}\right](2S_{njk}w+\delta)\right\}}{2\sqrt{\pi} S_{njk}^2 (w^2 - a^2)} \frac{\Gamma\left(\frac{1}{2}+S_{njk}\right)}{\Gamma\left(1+S_{njk}\right)} \qquad (C12)$$

For illustrative purposes, parameters for a spherical protein vesicle ($a$ = 250 nm, $\delta$ = 68 nm ) and an electron beam waist of $w$ = 367 nm have been used here [C5]. Additionally, Gaussian temporal profiles have been used for photon pulses and electron packets, with $\sigma_p$ = 150 fs and $\sigma_e$ = 300 fs, respectively. The EELS/EEGS plots are generated from the PINEM populations by convolution with the energy-profile of the incident electrons. For a Gaussian energy distribution of standard deviation $\sigma_E$, the EELS/EEGS distribution is described by Equation C13.

$$P_{EEGS}(E) \sum_n P(n) exp \left[ \frac{-(E-n\hbar\omega)^2}{2\sigma_E} \right] \qquad (C13)$$

Here, a FWHM of 1 eV ($\sigma_E$ = 0.425 eV) has been used for the incident electron energy distribution, and 519 nm ($\hbar\omega$ = 2.39 eV) has been used for the pump laser energy.

*Gaussian Fitting for Determining Temporal Durations* – To determine the temporal duration of peaks from EELS plots we employ Gaussian fitting of the temporal cross-sections at $n\hbar\omega$ (Eq. C14).

$$P_n(\tau) = Aexp \left[ \frac{-\tau^2}{2\sigma_n^2} \right] \quad (C14)$$

Provided the peaks take the form shown in Equation C14, the Gaussian temporal widths $\sigma_n$ can be determined from the least-squares fitting of $\ln(P_n)$ vs. $\tau^2$ such that $\sigma_n = \sqrt{\frac{1}{2(-\beta)}}$, where $\beta$ is the slope determined from least-squares analysis. Error values given are based on propagation of uncertainty using the standard error of the slope, $SE_\beta$.

171

As discussed in the text, least-squares fitting of $\sigma_n{}^2$ vs. $\frac{1}{n}$ can be performed to determine the temporal durations of the electron packet and photon pulse. The electron packet duration is given by $\sigma_e = \sqrt{\alpha}$, where $\alpha$ is the y-intercept of the regression analysis, and the estimated value of the photon pulse duration is given by $\sigma_p = \sqrt{\beta}$. Reported error values in Table 1 of the main text are calculated from propagation of uncertainty using standard errors of $\alpha$ and $\beta$.

## References

[C1]    B. Barwick, D.J. Flannigan, A.H. Zewail, Photon-Induced Near-Field Electron Microscopy, Nature 462 (2009) 902-906.

[C2]    S.T. Park, M. Lin, A.H. Zewail, Photon-Induced Near-Field Electron Microscopy (PINEM): Theoretical and Experimental, New J. Phys. 12 (2010) 123028.

[C3]    S.T. Park, A.H. Zewail, Enhancing Image Contrast and Slicing Electron Pulses in 4D Near Field Electron Microscopy, Chem. Phys. Lett. 521 (2012) 1-6.

[C4]    S.T. Park, O.-H. Kwon, A.H. Zewail, Chirped Imaging Pulses in Four-Dimensional Electron Microscopy: Femtosecond Pulsed Hole Burning, New J. Phys. 14 (2012) 053046.

[C5]    D.J. Flannigan, B. Barwick, A.H. Zewail, Biological Imaging with 4D Ultrafast Electron Microscopy, Proc. Natl. Acad. Sci. U.S.A. 107 (2010) 9933-9937.

# Appendix D | Detailed Methods for Discrete Chromatic Aberrations Study and Supplementary Information

*Methods*

**Calculation of point spread functions and transfer functions.** Projections of the electron-energy distribution in the Gaussian image plane are evaluated with the following TEM operating parameters: a collection angle ($\beta$) of 4.5 mrad, a coefficient of chromatic aberration ($C_c$) of 1.2 mm, and an accelerating voltage ($V$) of 200 kV. We approximate the Fourier transforms of the point spread functions (*PSF*) with the discrete Cooley-Tukey numerical approximation. One-dimensional (1D) cross-sections of the *PSF*s are sampled out to $r = \pm \frac{C_c \beta \; (240 \text{ eV})}{V}$ with frequency $F_s = \frac{V}{C_c \beta \; (0.24 \text{ eV})}$ in order to avoid low-frequency sampling artifacts. The radial symmetry of the *PSF*s allows rotational sweeping of 1D cross-sections of the FFT to produce two-dimensional transfer functions with increased numerical stability and accuracy.

**Image simulations.** The bright-field images of nanostructures shown in Figure 5 were acquired with a Tecnai Femto UEM (FEI Company) operated in thermionic mode at 200 kV. Images of Au nanocrystals were generated from a gold/graphitized carbon calibration specimen (Ted Pella), while those of the carbon nanotube were obtained from a specimen prepared by drop casting from a dilute solution (Sigma-Aldrich; outer diameter = 6 to 13 nm, length = 2.5 to 20 μm) in ethanol. To simulate the effect of quantized energy dispersion, the experimental images were convoluted with the chromatic *PSF* using the *imfilter* command with circular boundary options in Matlab. For accurate portrayal of blurring, the spatial sampling frequency of the experimental

images, 93.6 pixels nm$^{-1}$ for the Au nanocrystals and 76.4 pixels nm$^{-1}$ for the carbon nanotube, is replicated in the calculation of the chromatic *PSF*. Fast Fourier transforms of the images are displayed on a logarithmic color scale mapped from counts in the 85th (black) to the 98th percentile (white).

*Electron-photon coupling and the interaction parameter, Ω* – The extent of coupling that occurs between the probing electrons and pump photons is dependent upon both the properties of the near-field and the degree of overlap with the photoelectron packet in space and time.[D1,D2] From quantum mechanical treatment, transition probabilities for absorption or emission of n-quanta of the photon energy by a swift electron at position *t* within a temporal envelope can be represented by equation D1:

$$Q_n(t;\tau) = \left| J_n \left\{ \frac{-e|F_o|}{\hbar\omega_p} I_p(t-\tau)^{1/2} \right\} \right|^2 \quad \text{(D1)}$$

with –e being the electron charge, $\hbar\omega_p$ the photon energy, $I_p(t)$ is the pump laser-pulse intensity profile, and $J_n$ is an $n$[th]-order Bessel function of the second kind, and $\tau$ is the delay between the electron packet and photon pulse. Importantly, the $|\widetilde{F}_o|$ term is the Fourier component of the electric field at the critical spatial frequency necessary for electron-photon coupling such that the *z*-component of the phase velocity of light equals that of the electron velocity – that is, $k = \dfrac{\omega_p}{v_e}$. This term (obtainable through numerical solutions to Maxwell's equations) is dependent on the geometry of the specimen, the dielectric constant of the material, as well as the polarization, wavelength, and phase of the incident light. To evaluate the general dependencies of the electron-energy profile for

an arbitrary specimen, the near-field effects are collected into a single, non-dimensional

term called the interaction parameter ($\Omega$) which we define as $\Omega = \dfrac{e|F_0|}{\hbar\omega_p}$. [D2,D3]  The

peak energy densities associated with the optical excitation pulses employed in UEM

typically yield values of $\Omega$ ranging from five to 25 for typical pump-laser fluences.[D2]

      After integrating transition probabilities over the entire electron packet, the

energy envelope describing the population of discrete energy states, $P(E;\ \tau)$, is given by

Equation D2.

$$P(E;\tau) = \int P_e(t+\tau) J_{\frac{E}{\hbar\omega}} [\Omega I_p(t)^{1/2}]^2 dt \quad \text{(D2)}$$

Here, $E$ is the electron energy relative to those comprising the zero-loss peak (arising

from substituting $n = \dfrac{E}{\hbar\omega_p}$) and $P_e(t)$ is the electron-packet probability density.

Following this treatment, at $\tau = 0$ fs and $\Omega = 10$, a substantial number of the zero-loss

electrons are partitioned into discrete states at integer multiples of the photon energy,

with populations given by $P(E;\ \tau)$ and an energy distribution ($\Delta E$) governed by the initial

photo-generation process [Fig. 1b, main text].  Experimentally, electron energy loss/gain

spectroscopy (*i.e.*, EELS/EEGS) has been used to resolve peaks at up to $\pm 40\ \hbar\omega$, [D2]

corresponding to a total energy envelope spanning nearly 200 eV.  Within this strong-

interaction regime, the impact of the chromatic dispersion of the electrons, typically

about one part per million in conventional TEM, must be carefully considered in the

UEM image-formation process, especially at increased magnifications.

*Weak interaction versus strong interaction* – As the transition probabilities are governed by a Bessel function the second kind, implying a physical multi-state Rabii oscillation, a high degree of non-linearity occurs for strong interaction. However, we have shown previously [D4] that electrons sampling weak fields results in population of $n^{th}$-order side bands with temporal dependence that goes as the quadrature of the widths of the electron temporal envelope and the effective temporal optical pulse width (e.g.

$$\Delta_n = \sqrt{\Delta_e^{\,2} + \frac{\Delta_p^{\,2}}{n}}$$

). Similarly, the duration of the imaging aberration, $\Delta_t$, resulting from quantized chromatic dispersion exhibits a temporal dependence that goes as

$$\Delta_t = \sqrt{\Delta_e^{\,2} + \Delta_p^{\,2}}$$

for electrons sampling weak fields. This regime occurs for weak coupling-fields or, alternatively, when the electron packet is much longer than optical pulse and thus fewer electrons sample the intense fields associated with a greater probability for multiple transition events. Conversely, as discussed in the main text, strong coupling-fields or condensed electron packets result in departure from the non-linear coupling regime and the aberration durations are no longer described as above. Summarized in Supplementary Figure 1, contours of the predicted aberration duration [Fig. S1, a] roughly follow the linear-coupling contours [Fig. S1, b] when $\Delta_e > \sim 2\Delta_p$ and the optical pulse duration is short enough to sufficiently excite coupling events (i.e. $\Delta_p < \sim 600 fs$). In the non-linear regime, only marginal gains are achieved upon condensing the temporal envelope of the electron packet.
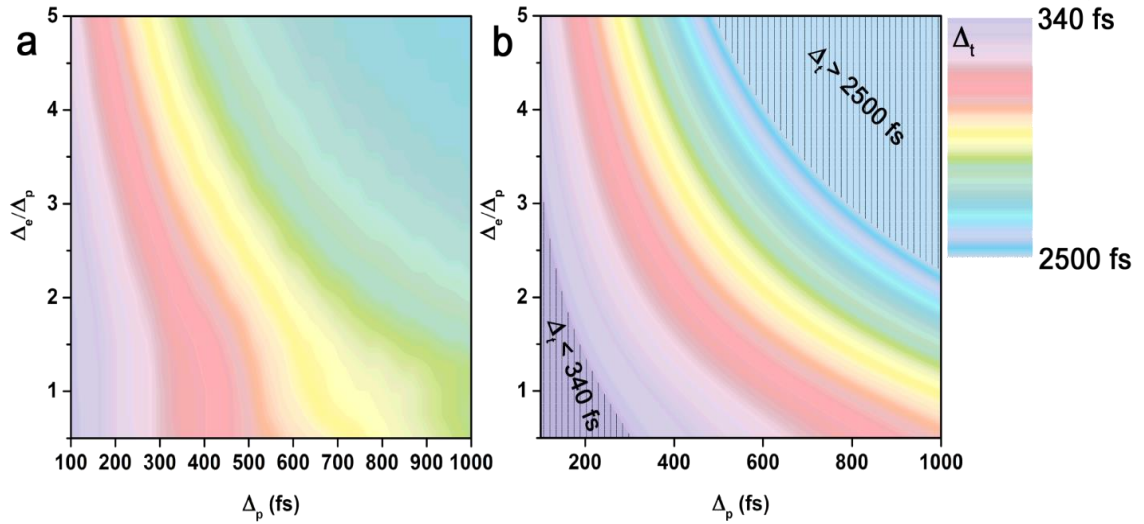
**Figure D1.** Comparison of aberration durations to linear-coupling regime. (a) Simulated contours of the aberration durations ($\Delta_t$) as a function of the temporal FWHMs of the optical pulse profile ($\Delta_p$) and electron packet envelope ($\Delta_e$). (b) Contours of $\Delta_t = \sqrt{\Delta_e^2 + \Delta_p^2}$ representing the linear-coupling behavior. (Note: Linear color-scale)

**REFERENCES**

D1.     García de Abajo, F. J.; Asenjo-Garcia, A.; Kociak, M., Multiphoton Absorption and Emission by Interaction of Swift Electrons with Evanescent Light Fields. Nano letters 2010, 10 (5), 1859-1863.

D2.     Park, S. T.; Lin, M.; Zewail, A. H., Photon-Induced Near-Field Electron Microscopy (PINEM): Theoretical and Experimental. New Journal of Physics 2010, 12 (12), 123028.

D3.     Feist, A.; Echternkamp, K. E.; Schauss, J.; Yalunin, S. V.; Schäfer, S.; Ropers, C., Quantum Coherent Optical Phase Modulation in an Ultrafast Transmission Electron Microscope. Nature 2015, 521 (7551), 200-203.

D4.     Plemmons, D. A.; Tae Park, S.; Zewail, A. H.; Flannigan, D. J., Characterization of fast photoelectron packets in weak and strong laser fields in ultrafast electron microscopy. Ultramicroscopy 2014, 146, 97-102.

# Appendix E | Additional Details for Instrument Response Characterization

## I.      Effect of Bias on Bunch Charge and Instrument Response

A series of cathode images were acquired with varying Wehnelt bias for a range of UV laser-pulse energies in order to determine the effects of electrostatic bias on the generation and the collection of photoelectrons.  As shown in Figure E2, there appears to be a threshold bias (here, reported as a 'heat-to' value) at which photoelectron counts begin to increase, particularly for relatively large UV pulse energies.  Despite this, the bias appears to have only a marginal effect on photoelectron collection for the cathode sizes and positions used here, as counts vary within only a factor of two for pulse energies and over the entire heat-to range (0 to 31).  It is important to emphasize that, for the UEM instrument used here, increasing the Wehnelt bias also increases the temperature of the $LaB_6$ cathode.  This produces a shift in the electron Fermi-Dirac distribution of the $LaB_6$, which will cause a variation in the photoemission process. Fitting the data with the model described by Equation 6.1 in the chapter 6 suggests that the relative magnitude of two-photon photoemission increases when the bias is in the *on* state.  This effect likely arises from an increase in population of the tail of the Fermi-Dirac distribution during resistive heating.  Table E1 is a compilation of the parameters used in the image-charge-limited model described by Equation 6.1 in the chapter 6. Parameters for both cathodes used here (50- and 100-μm flat, graphite encircled $LaB_6$; see chapter 2).
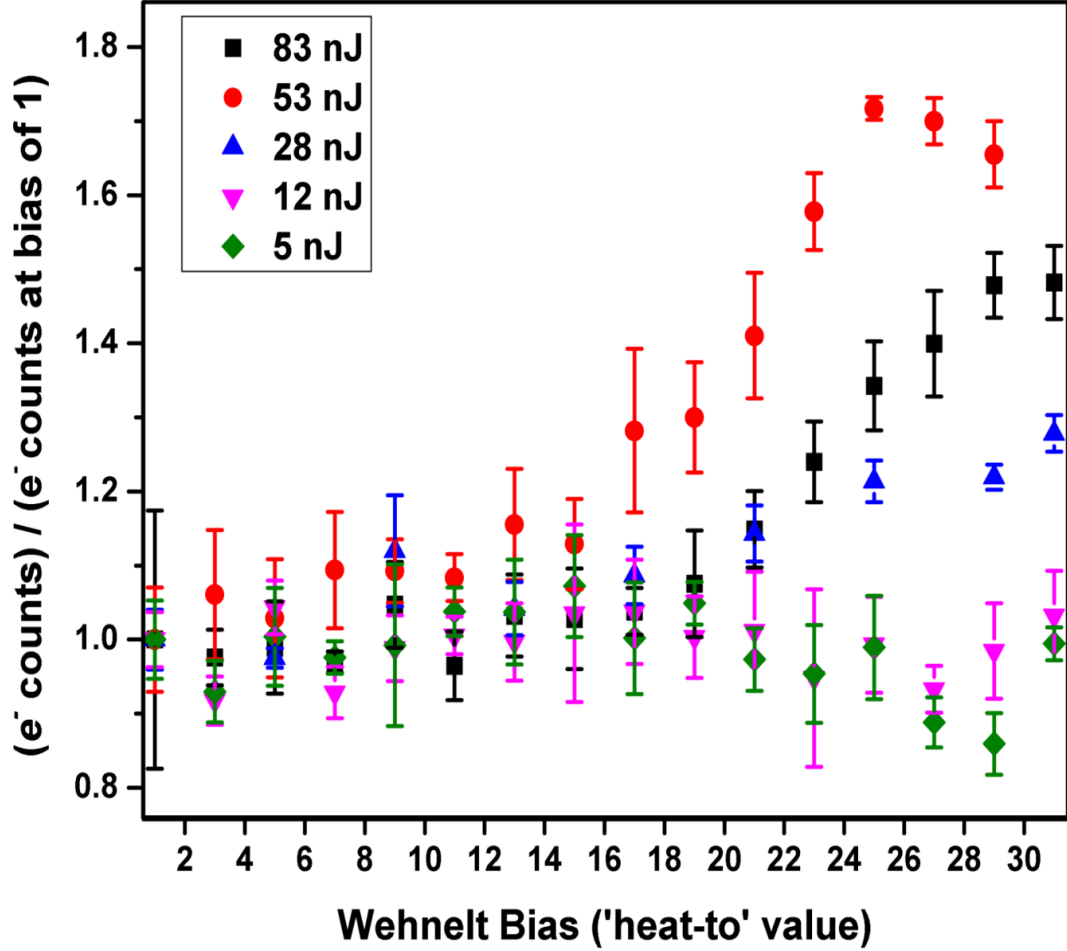
**Figure E1** Normalized photoelectron counts as a function of applied Wehnelt bias for a range of 700-fs UV laser pulse energies. The error bars represent one standard deviation.

**Table E1: Fit Parameters to Equation 6.1**

|  | Bias on, 100 μm | Bias off, 100 μm | Bias on, 50 μm | Bias off, 50 μm |
|---|---|---|---|---|
| $b_1$ ($e^-$/nJ) | 10.46 | 38.48 | 356.90 | 228.28 |
| $b_2$ ($e^-$/nJ$^2$) | 16.46 | 15.45 | 40.62 | 24.32 |
| $F_0$ (nJ) | 12.59 | 16.65 | 45.20 | 33.76 |

| $n_e^{lim}(e^-)$ | 3,971.00 | 4,946.63 | 25,436.41 | 10,834.19 |
|---|---|---|---|---|
| $b_0\ (e^-)$ | 8.59 | 0.11 | 0.00 | 0.00 |

To test for any effect of applied Wehnelt bias on measured instrument-response time, $\sigma_t$ was determined at the extreme and mid-range heat-to values (1, 16, and 31) for a range of photoelectron-packet populations (Figure E2). As throughout the main text, $\sigma_t$ is the standard deviation of the Gaussian peak function that results from the derivative of the kinetic image-intensity error function (see Figures 6.3 and 6.4 in chapter 6). As can be seen in Figure E2, application of a bias at the three values used here has no discernible effect on the instrument-response time or the power-law trend observed for $\sigma_t$ versus photoelectron-packet population (*i.e.*, UV laser-pulse energy).
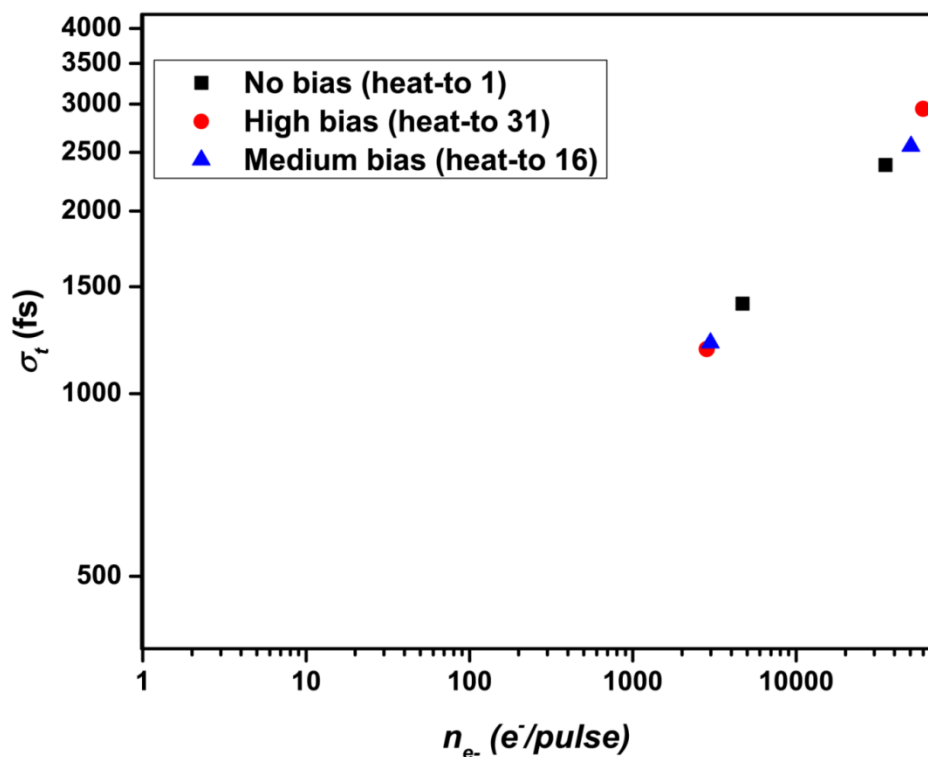
**Figure E2** Instrument-response time (fs; standard deviation of Gaussian function) at 1 (black squares), 16 (blue triangles), and 31 (red circles) heat-to values (*i.e.*, Wehnelt bias) as a function of photoelectron-packet population (electrons per pulse).

## II.  Time Zero

Figure E3 shows the observed apparent stochastic fluctuation in measured time zero as a function of photoelectron-packet population for three individual UEM image scans.  The effect appears to become more pronounced for larger packet populations, suggesting a modest acceleration occurs during generation and propagation (*i.e.*, the packets with populations above ~$10^4$ arrive at earlier times relative to packets below this value).
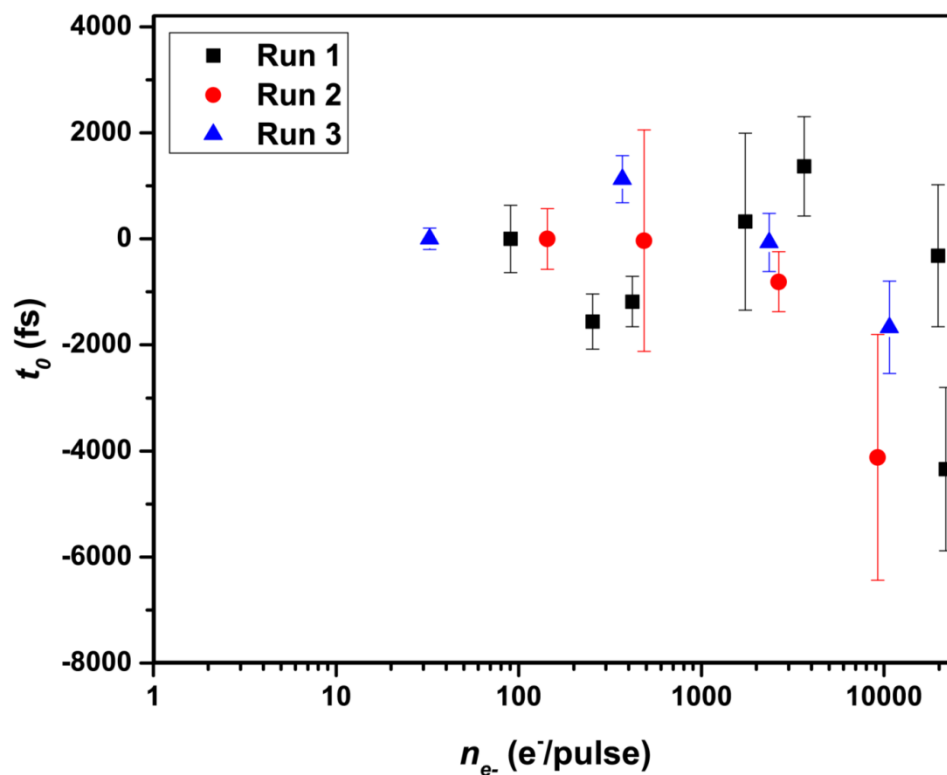
**Figure E3** Relative arrival time of photoelectron packets as a function of population (*i.e.*, UV pulse energy). Three individual UEM image scans are shown (Run 1, 2, and 3). The error bars represent one standard deviation.

## Appendix G | Image Processing Steps and Additional BF-image Series Information

In generating panels (b-g) and (j-o) in Fig. 7.1 of the main text, several steps were taken in converting the photoelectron images to 3D surface plots. First, difference images were created by taking an average of 10 pre-time-zero images (dubbed the reference image) and subtracting it from each frame in the series. Second, the difference image was modified for contrast and brightness in order to enhance the features of interest, including passing the images through a 10-pixel Gaussian smoothing filter. Third, each image was leveled by adjusting any pixels with values above 90% or below 10% of the maximum and minimum intensity, respectively, to the 90% and 10% values, respectively. In addition, a one-pixel swath along the edges of each image was set to the 10% intensity value.

The line scans shown in Fig. 7.1(h) of the main text were generated by first drift correcting the series of images and rotating each frame such that the direction of propagation was horizontal across the field of view. Following this, three adjacent regions measuring 12 by 100 pixels were identified in each image series such that the contrast waves traversed these in succession; the regions were offset in the horizontal direction such that each would sample the contrast wave one after the other. At every time delay, each region was summed in the vertical direction, and the average was determined in the horizontal. Plotting the mean intensities as a function of time delay makes apparent the transitory nature of the waves, as illustrated in Fig. 7.1 of the main text. Phase velocities were extracted by taking the slope of a line connecting the peaks of

184

the mean intensities and converting the pixel values of each region to a real-space position.

Panels (b-f) of Fig. 7.2 in the main text were generated in a similar manner as Fig. 7.1. A 6 pixel by 6 pixel average filter was applied to difference images created by subtracting an average of 10 pre-time-zero images (*i.e.*, the average reference image). The resulting frame was then thresholded at the $80^{th}$ percentile and placed in the saturation channel of an HSV (*i.e.*, h̲ue, s̲aturation, and v̲alue) image such that the bright, dynamic contrast appears red. In order to highlight the appearance of contrast at the interface, a 3 pixel by 3 pixel vertical Prewitt-filtered version of the original image was placed in the value channel. The line scans were obtained in the same fashion as for Fig. 2.

The space-time surface plot in Fig. 7.3(a) of the main text was generated by first rotating each image such that the axis of propagation is oriented directly vertical. A 651 pixel ($Y$) by 100 pixel ($X$) box was selected for the region of interest and median filtered (4 pixel by 4 pixel). Next, the profile for each time delay was created by determining the mean of the 100-horizontal pixels for each of the vertical single-pixel-wide sections and then subtracting the vertical 651-pixel time-zero reference. Thus, the motion appears as diagonal streaks in the surface plot, with the velocity captured in the slope. The frequency traces were created by taking a discrete Fourier transform of a de-trended time trace for various pixels (one at a time). The displayed results represent the average of the Fourier transforms determined over the 20-pixel vertical range.
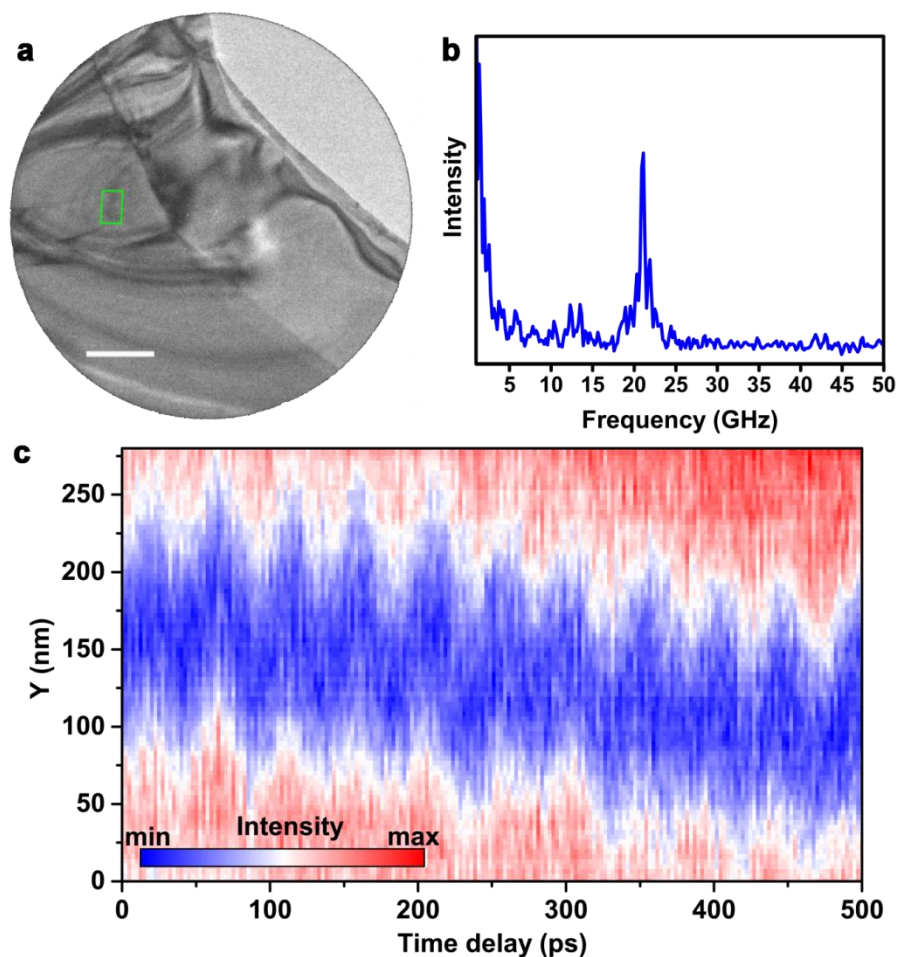
**Figure G3. Moiré-fringe dynamics.** (a) Bright-field image of a WSe$_2$ region showing Moiré fringes. The green box indicates the region of interest analyzed to generate panels (b) and (c). Note that this is the same specimen region shown in Fig. 4 of the main text. The *xy*-orientation is different because the specimen was removed from the holder following the experiments done to generate Fig. 4 of the main text and then replaced for the experiments done to generate this figure. The change in orientation also produced a slight difference in specimen angle with respect to the incoming photoelectron wavevector. This results in bright-field images (and thus, fs electron images and videos) showing different contrast patterns due to changes in the Bragg condition across the field

186

of view. Detailed studies to quantify this behavior with respect to acoustic-phonon dynamics and fs electron-imaging experiments are currently underway in our lab and will be reported elsewhere. Scale bar = 1 μm. **(b)** Average frequency spectrum generated from 150 pixels perpendicular to the direction of motion within the region of interest. **(c)** Space-time contour plot of the region of interest in (a). Oscillations of the particular Moiré fringe (blue) about a fixed spatial position are indicative of the echoing of the $c$-axis phonons against the boundaries of the layered crystal, with the period given by $\tau =$ $2d/v$, where $d$ is the crystal thickness and $v$ is the $c$-axis speed of sound[1]. Taking the $c$-axis speed of sound to be $v = 1.65$ nm/ps (as measured with picosecond acoustic and interferometry methods)[2] and the thickness to be $d = 36$ nm (27 to 28 layers) yields a period of $\tau = 44$ ps ($f = 22.7$ GHz).